MAGNETIC, SUPERCONDUCTING ORDERS AND IMPURITY EFFECT IN 122 IRON-PNICTIDES

A Dissertation

Presented to

the Faculty of the Department of Physics

University of Houston

In Partial Fulfillment

of the Requirements for the Degree

Doctor of Philosophy

By

Bo Li

May 2015

MAGNETIC, SUPERCONDUCTING ORDERS AND IMPURITY EFFECT IN 122 IRON-PNICTIDES

Bo Li

APPROVED:

Dr. Kevin E. Bassler, Chairman

Dr. Chin-Sen Ting

Dr. Wu-Pei Su

Dr. Arnold M. Guloy

Dean, College of Natural Sciences and Mathematics

Acknowledgements

First of all I would like to thank my Ph.D. advisor Prof. Kevin E. Bassler. His continuous support, constructive suggestions, and encouragements greatly helped me to overcome many difficulties. He taught me how to think like a physicist in both classes and daily research.

I have special thanks to Prof. C. S. Ting, who opened a door for me towards the amazing world of superconductivity. His wisdom and acquaintance in this field benefited me a lot in my research. I'm thankful to my graduate committee members Prof. Arnold Guloy, Prof. Haibing Peng, and Prof. Wu-Pei Su for their great help and support. They gave me many helpful suggestions and advice on my research.

I would like to thank Dr. Charo I. Del Genio; his patient instructions helped me a lot to improve my computational skills. I am grateful to Dr. Yi Gao and Dr. Huaixiang Huang who helped me a lot when I started to learn BdG equations. I also thank Dr. Yuan-Yen Tai for providing his GPU codes to me and sharing many great physics ideas with me. I want to thank Dr. Jian Li, Dr. Hong-Yi Chen, and Dr. Lihua Pan for their great cooperation and helpful guidance in my research. I am also grateful to Dr. Yuanyuan Zhao and Dr. Yaohua Chen for a lot of useful discussions.

I have many thanks to my wife, Dr. Yang Zhao. She is the most beautiful thing I have ever met in this world. I am feeling lucky and grateful to all of my friends who helped me a lot during these years. I am especially grateful to my parents Lianmei Zhao and Yanxian Li; they gave me a wonderful childhood. I could not finish this without their understanding and selfless support.

MAGNETIC, SUPERCONDUCTING ORDERS AND IMPURITY EFFECT IN 122 IRON-PNICTIDES

An Abstract of a Dissertation

Presented to

the Faculty of the Department of Physics

University of Houston

In Partial Fulfillment

of the Requirements for the Degree

Doctor of Philosophy

By

Bo Li

May 2015

Abstract

Iron-based high temperature superconductors (HTS) were discovered in 2008; many experimental and theoretical studies have been initiated since then. Driven by several interesting experiments and based on a phenomenological two-orbital tight-binding model, the Fe-based HTS systems under different types of effects were investigated theoretically. First, the system was studied under the effect of different types of twin-boundaries. The magnetic, SC, and electron density properties of magnetic domain walls induced by twin boundaries were studied in the electron-under-doped region of $BaFe_2As_2$. The SC order can be either enhanced or suppressed near different types of twin boundaries. Second, the system was studied under the effect of highly electron-doped charge carriers. The nearest-neighbor pairing additional to the next-nearest-neighbor one was added in the Hamiltonian of highly electron-doped $A_xFe_2Se_2$ system. The d-wave pairing orders were obtained in such system. Third, the system was studied under the effect of magnetic field and single Zn impurity. A single strong non-magnetic Zn impurity was placed in the center of vortex core when the system was under the effect of magnetic field. The system showed a combination of both vortex and impurity properties. Lastly, the system was studied under the effect of single and multiple Zn impurities. The impurity effect based on a single orbital Zn model was studied. The calculated suppression of SC order with different concentrations of Zn impurities agrees quantitatively with the experimental data.

Contents

Chapter 1

Introduction

In 2008, Kamihara and co-authors reported an Fe-based high temperature superconductor (HTS), $LaO_{1-x}F_xFeAs$, with $T_c = 26K$ [1]. Very soon in that year another Fe-based HTS with $T_c = 55K$, $SmO_{1-x}F_xFeAs$, was found by Z.-X. Zhao's group [2]. These two discoveries, along with many others [3–5] of Fe-based superconductors, offer an alternative avenue to explore the physics of a new family of HTS, and many experimental studies have been initiated since then. For example, the superconducting (SC) and magnetic phase diagrams were obtained in both electron-doped [6–13] and hole-doped [14] regions of FeAs-122 family; the magnetic domain wall structure was observed along the twin boundaries on several Fe-based HTS [15, 16]; a robust SC phase was reported in a highly electron-doped sample $K_xFe_2Se_2$ [17–20], etc. Although the experimental research on Fe-based HTS has been making significant progress, correlated theoretical study is still trying to follow up. A lot of phenomena observed in the experiments cannot be well explained under current theoretical

models. The objective of my research is to narrow the gap between experimental frontier and the following theoretical study on Fe-based HTS.

The Fe-based HTS system is highly complicated, and no theory has given a satisfying explanation to it so far. Usually the birth of a successful theory is based on the analysis of existing experimental measurements and the verification of predicted phenomena. My research was intended to add bricks in the construction of such a theory. My work was driven by several interesting experiments, especially in Fe-pnictides (compounds containing iron and pnictogen elements), which could not be theoretically understood by existing models. Specific adjustments were added to the previous model based on the particular physical properties in those experiments. According to the modified model, some of the system's physical quantities can be calculated and compared with the experimental measurements, and some other quantities which had not been measured can be regarded as predictions to be verified in future experiments. I have successfully done this on the subject of twin-boundary structures, robust SC phase in $K_xFe_2Se_2$, impurity pinned at the center of vortex core structure, and Zn impurity effects. These works will be further discussed in the following chapters.

This chapter is organized as follows. In Sec. 1.1 some important experimental results and first principle calculations on Fe-based HTS are introduced. In Sec. 1.2 I will briefly exhibit several theoretical models. In Sec. 1.3 the development and major achievements of a phenomenological two-orbital model are introduced. This model would be a starting point for me to further investigate some specific experiments. In Sec. 1.4 a self-consistent field method, the so called BdG equations, is discussed

in detail. This method is essential to many superconducting studies. It is able to diagonalize the Hamiltonian matrix of HTS, and consequently obtain the system physical quantities. In Sec. 1.5 the supercell technique is introduced. This technique can help to improve the resolution of local density of states (LDOS), a quantity which can be directly measured in scanning tunneling microscope (STM) experiments. In Sec. 1.6 the numerical method in order to realize the BdG equations is discussed. In Sec. 1.7 an overview of the following chapters is exhibited.

1.1 Iron-based superconductors

Different Fe-based HTS families are characterized by their crystal structures. Typically they are constructed by two different types of atom layers: one layer with elements Fe and X (X=As, Se, Te, etc.), and the other layer with some other elements. So far, there are five major types of Fe-based HTS: 11-FeSe, 111-LiFeAs, 122-$SrFe_2As_2$, 1111-LaFeAsO, and 32522-$Sr_3Sc_2O_5Fe_2As_2$ [21]. All the FeX layers in these five types of Fe-based HTS share the same structure; all the Fe atoms are on the same plane, while the X atoms are tetrahedrally joined. However the X atoms are not on the same plane with Fe; they are either above or below the Fe plane, which is very different from the Cu-O-based HTS (cuprates) in which both Cu and O atoms are located on the same plane. Take the crystal structure of $BaFe_2As_2$ compound as an example, shown in Fig. 1.1. All the Fe atoms (red dots) are located on the same plane, but the As atoms (green dots) one either above or below the Fe plane. The Ba atoms are in between two neighboring FeAs layers. This upper/lower

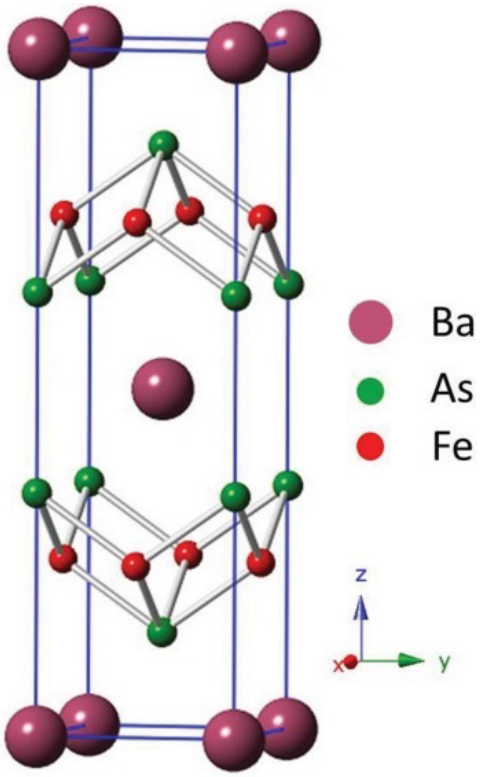

Figure 1.1: Crystal structure of the compound $BaFe_2As_2$, from Ref. [22]

X atom position property plays an important role in affecting the orbital orientation and pairing symmetries.

The FeAs-122 family has been studied a lot both experimentally and theoretically in order to get a better understand of the electronic structure, magnetic structure, and pairing symmetries of Fe-based HTS. By manipulating the chemical or structural properties, the phase diagram of the Fe-based HTS systems can be produced. As shown in Fig. 1.2, chemical doping (or substitution) of Co or K atom is applied to drive an antiferromagnetic (AFM), non-superconducting parent compound $BaFe_2As_2$ to a superconducting (SC), non-AFM state. Substitution of different types of atoms

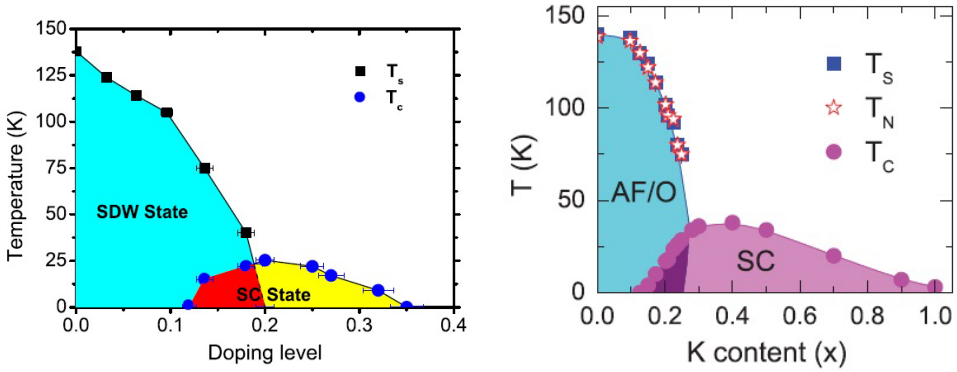

Figure 1.2: The SC and magnetic phase diagram of different doping level in (left panel) electron-doped $BaFe_{2-x}Co_xAs_2$ from Ref. [33] and (right panel) hole-doped $Ba_{1-x}K_xFe_2As_2$ from Ref. [22].

will lead to a difference in charge carrier properties in the system. The doped Co atoms add electrons as charge carriers while substitution from Ba to K atoms increases holes in the system. This phase diagram of 122-$BaFe_2As_2$ family as shown in Fig. 1.2 is very similar to several other unconventional superconductors, for example cuprates [23, 24]. In the under-doped regime, both the spin density wave (SDW) and SC order coexist. When the material is further doped, the SDW is continuously suppressed until it fully disappears, and there is only SC order left in the optimal- and over-doped regimes. This phase diagram property has been confirmed in many experimental works [25–31]. However it differs from some of the other types of Fe-based HTS families such as 11-FeSe systems [32], which reveals some intrinsic distinctions between different Fe-based HTS families.

Two non-equivalent As atoms (located above and below the Fe plane) result in the folding of the first Brillouin Zone (BZ) to include two Fe atoms per unit cell. Based on that, the electronic band structure has been calculated using the

local density approximation (LDA) method [34]. The calculation results show that the electronic properties are mainly dominated by five Fe d-orbital states near the Fermi energy, including two hole pockets around the BZ center (Γ point) $(0, 0)$, and two electron pockets around the BZ corner (M point) $(\pm\pi, \pm\pi)$. Though the mechanism of the SC in Fe-based HTS still remains an open subject, a great number of theoretical models [35–37] believe that the complex geometry of the Fermi surface (FS) including both hole and electron pockets in the BZ should be mainly responsible for the SC in weakly and moderately doped systems. For example, in the Co doped $BaFe_{2-x}Co_xAs_2$ compound, the SC disappears at almost the same doping level as where the hole pockets vanish in the FS in electron-doped samples [38–42]. This relationship between the evolution of FS and SC orders corresponding to different dopings could be a strong evidence to support the importance of the interaction between electron and hole pockets. Further theoretical studies based on this will be discussed in the following section.

1.2 Theoretical approaches

The most accurate way to study a solid system is to do calculations based on the first principle theory. Technically the interactions between every possible combination of two particles in the system should be considered in the calculation. Considering the number of particles in a typical superconductor sample, to solve this many-body problem is far beyond current calculation ability. In order to study the HTS more practically, some approximations must be done. One widely used approximation is

the tight-binding model. The electrons in this model should be tightly bound to the atom to which they belong, and they should have limited interaction with states and potentials on surrounding atoms of the solid. This model considers all the limited interaction of the electrons as perturbations. This approximation will reduce the calculation work tremendously.

Based on the tight-binding approximation, a number of phenomenological models were proposed to study the Fe-based HTS. These models are mainly characterized by the number of electron orbitals considered. A comprehensive idea is to include all possible valence electron orbitals on the Fe-plane. For the FeAs-122 family, five Fe-3d orbitals and three As-4p orbitals are taken into consideration, which makes it an eight-orbital model [43]. If considering only the SC order contributed by Fe atoms (five 3d orbitals), a five-orbital model will come up naturally [44]; however these five Fe-3d orbitals are not equally contributing. Several three-orbital models which include only three orbitals (d_{xy}, d_{xz} and d_{yz}) were also proposed [45, 46]. Lastly if the number of orbitals in the model is reduced to two (d_{xz} and d_{yz}), then we reach the minimal two-orbital models [47–50]. These models were invented for different reasons and were used for different calculations. A general principle here is that the electronic properties, for example the band structure, can be more accurate with a large number of orbitals, however the cost of this accuracy is the increasing amount of numerical work. Limited by current calculation abilities, this means that these models can only do calculations on a small lattice size in real space. However a lot of experimental results cannot be modeled in a system with small lattice size, for

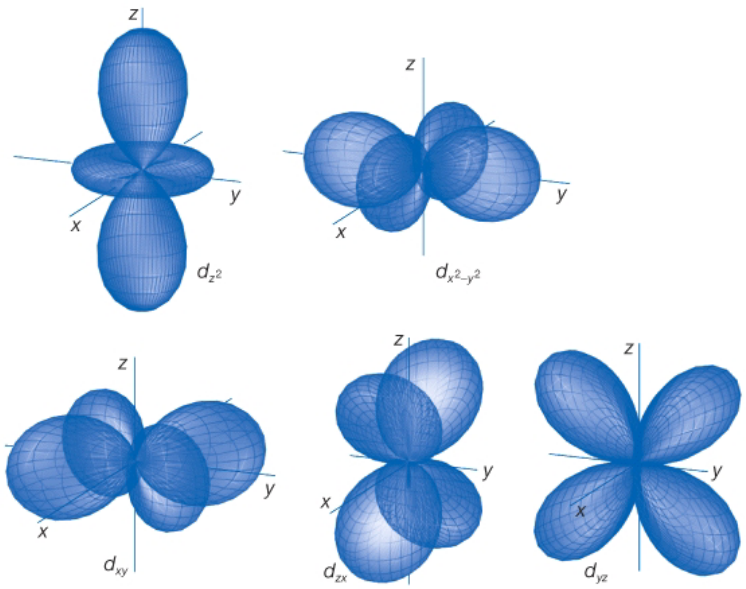

Figure 1.3: The probability patterns for the five 3d-orbitals in an iron atom. Only the d_{zx} and d_{yz} orbitals are considered in the two-orbital model.

example, the twin boundary structures, magnetic vortex core states, and multiple-impurity effects. This requires us to extract the most important physics part in the Fe-based HTS with a simplified calculation.

The probability patterns of the five Fe-3d orbitals are shown in Fig. 1.3. According to the partial density of state (PDOS) work from [51], the $d_{xz}$and d_{yz} orbitals are very close to the FS and are highly degenerated in energy among five Fe-d orbitals. Thus many important electronic and magnetic properties can be studied by only including these two orbitals. Another LDA calculation in $CaFe_2As_2$ system [52] also concluded that the most important orbitals to form SC phase in Fe-based HTS are d_{xz} and d_{yz} orbitals. The SDW order can be generated with Hubbard interaction U and Hund's coupling J_H. Therefore the two-orbital model which considers the Fe-3d

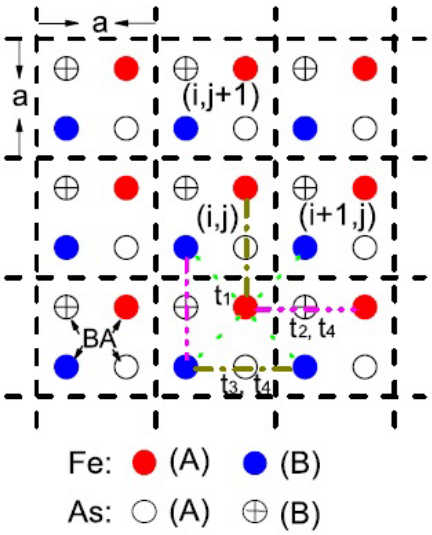

Figure 1.4: Schematic lattice of Fe-As layers with each unit cell containing two Fe (A and B) and two As (A and B) atoms, here the As atoms are located above and below the Fe plane, from Ref. [53]. The green, pink and brown lines represent the nearest-neighbor hopping, next-nearest-neighbor hopping across B-type As atoms and next-nearest-neighbor hopping across A-type As atoms correspondingly.

d_{xz} and d_{yz} orbitals was used in my research work. The details of this model will be discussed in the following section.

1.3 A two-orbital model

In 2009, D. Zhang proposed a two-orbital tight-binding model [53] in order to explain the new families of Fe-based HTS theoretically. In his model, the inequivalent As atoms above and below the Fe plane are taken into consideration. As shown in Fig. 1.4, the inequivalent As atoms create two sublattices A and B in the system. The next-neareast-neighbor (NNN) Fe-Fe hoppings have different values when across

different types of As atoms. Zhang's model gave nice FS evolution at least in the electron-doped side, and it was also successfully applied to calculate the phase diagram and LDOS by T. Zhou and co-authors [54]. In that work, the on-site Hubbard interaction U, the Hund's coupling J_H and the pairing interaction V were applied to Zhang's model, then the Hamiltonian of the model would be

$$H = H_0 + H_{SC} + H_{int}. \tag{1.1}$$

The first term H_0 is the hopping terms and chemical potential from Zhang's model, it can be explicitly expressed as

$$H_0 = -\sum_{i\mu j\nu\sigma} t_{i\mu j\nu} c^{\dagger}_{i\mu\sigma} c_{j\nu\sigma} - t_0 \sum_{i\mu\sigma} c^{\dagger}_{i\mu\sigma} c_{i\mu\sigma}, \tag{1.2}$$

where $t_{i\mu j\nu}$ is the hopping parameter between two electrons, one at position i with the orbital μ and the other at position j with orbital ν, and $c^{\dagger}_{i\mu\sigma}$ is the creation operator of an electron with spin σ at position i with orbital μ. t_0 is the chemical potential. As shown in Fig. 1.4, four types of hopping were included in the model: t_1 is the nearest-neighbor (NN) intraorbital hopping, t_2 is the NNN intraorbital hopping across As atoms belonging to B sublattice, t_3 is the NNN intraorbital hopping across As atoms belonging to A sublattice, and t_4 is the NNN interorbital hopping. The second term H_{SC} includes the pairing interaction energy,

$$H_{SC} = \sum_{i\mu j\nu\sigma} (\Delta_{i\mu j\nu} c^{\dagger}_{i\mu\sigma} c^{\dagger}_{j\nu\bar{\sigma}} + \text{H.c.}), \tag{1.3}$$

where $\Delta_{i\mu j\nu}$ is the pairing parameter between two electrons. Here $\bar{\sigma}$ denotes the opposite spin of σ. The third term includes both the Hubbard interaction U and the Hund's coupling J_H,

$$H_{int} = (U - 3J_H) \sum_{i,\mu\neq\nu,\sigma} \langle n_{i\mu\sigma}\rangle n_{i\nu\sigma} + (U - 2J_H) \sum_{i,\mu\neq\nu,\sigma\neq\bar{\sigma}} \langle n_{i\mu\bar{\sigma}}\rangle n_{i\nu\sigma}$$

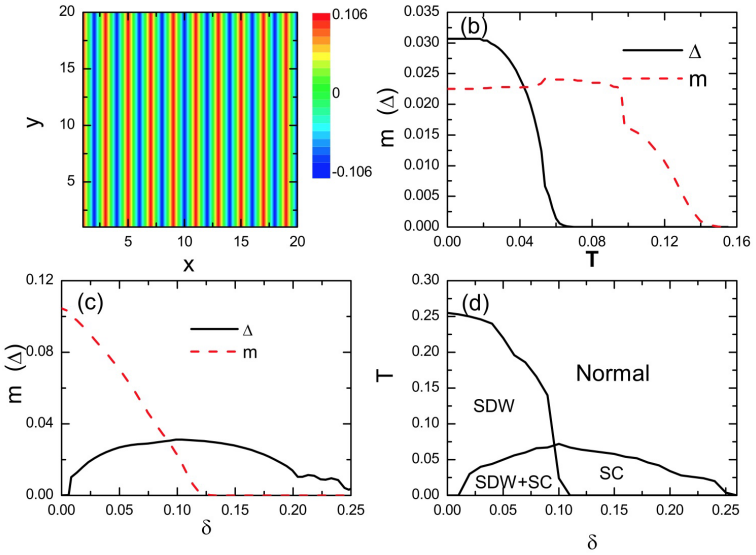

Figure 1.5: (a) Two-dimensional real space map of SDW order, red and blue represent the positive and negative orders, (b) temperature dependence of SC and SDW order with the doping density $\delta = 0.09$, (c) magnitude of SC and magnetic order as a function of the doping at zero temperature and (d) the calculated phase diagram of SDW and SC critical temperatures at different electron-doped levels, from Ref. [54].

$$+U \sum_{i,\mu,\sigma\neq\bar{\sigma}} \langle n_{i\mu\bar{\sigma}} \rangle n_{i\mu\sigma}, \tag{1.4}$$

where $n_{i\mu\sigma}$ is the electron number operator $c^{\dagger}_{i\mu\sigma} c_{i\mu\sigma}$, and $\langle n_{i\mu\sigma} \rangle$ is the expectation value of $n_{i\mu\sigma}$. This effective model can describe well the electron-doped phase diagram for $BaFe_2As_2$ family as shown in Fig. 1.5. However this model has limitations to be applied in the hole-doped region, therefore Y. Tai made some improvements to it which worked well in both electron-doped and hole-doped regions.

Y. Tai made several improvements to the model in 2013 [55]. In Y. Tai's model, the inequivalent As atom property was kept, and an additional 90-degree rotation between the d_{xz} and d_{yz} intra-orbital hopping was also applied in the NNN hopping terms as shown in Fig. 1.6. Besides the orbital rotation, two more hopping terms

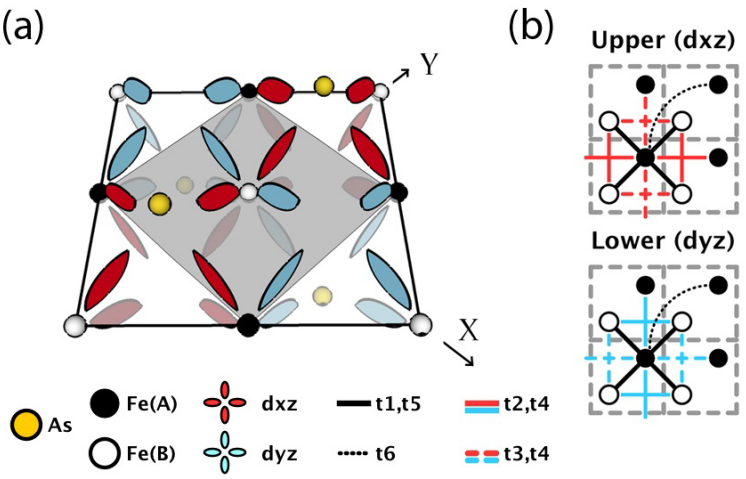

Figure 1.6: (a) Three-dimensional schematic picture of the spatial orientations of Fe d_{xz} and d_{yz} orbitals, the inter-site hopping terms are related to the spatial overlap between each orbital. (b) Illustration of the hopping terms in Fe d_{xz} (upper) and d_{yz} (lower) orbitals, lines connected between two atoms represent the inter-site hoppings, from Ref. [55].

were added in this model, t_5 is the NN interorbital hopping and t_6 is the 3rd-nearest neighbor intraorbital hopping. Y. Tai's model gave very good phase diagram results in both electron-doped and hole-doped sides as shown in Fig. 1.7. This model has also made its success in the calculation of FS evolutions [56] and multiple Zn impurities [57] in FeAs-122 family HTS.

1.4 Self-consistent field method

In the previous section, a phenomenological two-orbital model [55] proposed by Y. Tai was introduced. In order to calculate the physical quantities we are interested in, such as the SC order parameter, charge carrier density order, and LDOS on

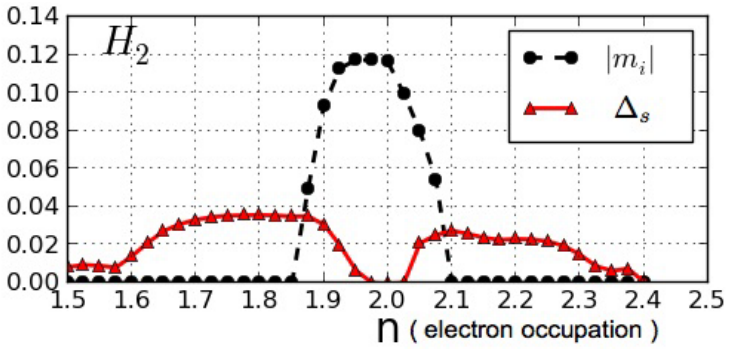

Figure 1.7: The SDW order (m_i) and SC order (Δ_s) at different doping levels in both electron-doped and hole-doped regions at zero temperature, from Ref. [55].

particular lattice site, the Hamiltonian needs to be diagonalized. This diagonalization process is equivalent to a change of bases from the current electron-operator base to a new quasi-particle-operator base, and the Hamiltonian in our model 'happens' to be a diagonal matrix in the new base. This process can be systematically done according to a self-consistent field method, so called the Bogoliubov-de Gennes (BdG) equations. This method was first proposed in P. de Gennes's book [58], and has become one of the most fundamental frameworks in the theory of superconductivity. I will go through the detail of the BdG equations in this section.

The Hamiltonian from the above phenomenological models can be written as

$$\begin{aligned} H_0 &= -\sum_{i\mu j\nu\sigma}(t_{i\mu j\nu}c^\dagger_{i\mu\sigma}c_{j\nu\sigma}) + \sum_{i\mu\sigma}(m_{i\mu\sigma}-t_0)c^\dagger_{i\mu\sigma}c_{i\mu\sigma} + \sum_{i\mu j\nu\sigma}(\Delta_{i\mu j\nu}c^\dagger_{i\mu\sigma}c^\dagger_{j\nu\bar{\sigma}} + \text{H.c.}) \\ &= \sum_{i\mu j\nu\sigma}(\mathcal{H}_{i\mu j\nu\sigma}c^\dagger_{i\mu\sigma}c_{j\nu\sigma}) + \sum_{i\mu j\nu\sigma}(\Delta_{i\mu j\nu}c^\dagger_{i\mu\sigma}c^\dagger_{j\nu\bar{\sigma}} + \text{H.c.}), \end{aligned} \tag{1.5}$$

where

$$\mathcal{H}_{i\mu j\nu\sigma} = -t_{i\mu j\nu} + (m_{i\mu\sigma}-t_0)\delta_{ij}\delta_{\mu\nu}.$$

In the above expression, the Hamiltonian is in electron-operator base, because all

the creation and annihilation operators $c^{\dagger}_{i\mu\sigma}$ and $c_{i\mu\sigma}$ are operating on electrons. Typically, the Hamiltonian is not diagonalized in this base. Assume the Hamiltonian can be diagonalized in a new quasi-particle base $\gamma^{\dagger}_{n\sigma}$ and $\gamma_{n\sigma}$, the relationship between the new base and the current one is shown below as

$$c_{i\mu\sigma} = \sum_{n=1}^{N} \left[u^{n}_{i\mu\sigma} \gamma_{n\sigma} - \sigma v^{n*}_{i\mu\sigma} \gamma^{\dagger}_{n\bar{\sigma}} \right], \tag{1.6}$$

$$c^{\dagger}_{i\mu\sigma} = \sum_{n=1}^{N} \left[u^{n*}_{i\mu\sigma} \gamma^{\dagger}_{n\sigma} - \sigma v^{n}_{i\mu\sigma} \gamma_{n\bar{\sigma}} \right], \tag{1.7}$$

where N is the total number of all possible combinations of operators $c^{\dagger}_{i\mu\sigma}$ and $c_{j\nu\sigma}$. One of the main tasks of the BdG equations is to obtain the coefficients in the above equations. The $\gamma_{n\sigma}$ and $\gamma^{\dagger}_{n\sigma}$ are new quasi-particle operators that still satisfy the anticommutation relations

$$\left\{ \gamma_{n\sigma}, \gamma^{\dagger}_{m\sigma'} \right\} = \delta_{n,m} \delta_{\sigma,\sigma'}, \tag{1.8}$$

$$\left\{ \gamma_{n\sigma}, \gamma_{m\sigma'} \right\} = \left\{ \gamma^{\dagger}_{n\sigma}, \gamma^{\dagger}_{m\sigma'} \right\} = 0. \tag{1.9}$$

Such anticommutation relation indicates that the new quasi-particles behave like fermions. According to our assumption, the new base should diagonalize the Hamiltonian, therefore after the transformations Eq. 1.6 and 1.7 our Hamiltonian can be written in the form

$$H = \sum_{n} \left(E_{n\uparrow} \gamma^{\dagger}_{n\uparrow} \gamma_{n\uparrow} + E_{n\downarrow} \gamma^{\dagger}_{n\downarrow} \gamma_{n\downarrow} \right), \tag{1.10}$$

where $E_{n\uparrow}$ and $E_{n\downarrow}$ are the diagonal elements of Hamiltonian in the new base. In order to be convenient for the following discussion, we name them eigen-energies of excitations n. To obtain the eigen-energies is another main task in the BdG

equations. We can also write this condition by using the anticommutation relation between $c_{i\mu\sigma}$ and Eq. 1.10,

$$[c_{i\mu\sigma}, H] = \sum_n \left(E_{n\uparrow} u^n_{i\mu\uparrow} \gamma_{n\uparrow} + E_{n\downarrow} v^{n*}_{i\mu\uparrow} \gamma^\dagger_{n\downarrow} \right), \tag{1.11}$$

$$\left[c^\dagger_{i\mu\bar{\sigma}}, H\right] = \sum_n \left(E_{n\uparrow} v^n_{i\mu\downarrow} \gamma_{n\uparrow} - E_{n\downarrow} u^{n*}_{i\mu\downarrow} \gamma^\dagger_{n\downarrow} \right). \tag{1.12}$$

They can be more compactly written as

$$\begin{pmatrix} [c_{i\mu\sigma}, H] \\ \left[c^\dagger_{i\mu\bar{\sigma}}, H\right] \end{pmatrix} = \sum_n \begin{pmatrix} E_{n\uparrow} u^n_{i\mu\uparrow} & -E_{n\downarrow} \left(-v^{n*}_{i\mu\uparrow}\right) \\ E_{n\uparrow} v^n_{i\mu\downarrow} & -E_{n\downarrow} u^{n*}_{i\mu\downarrow} \end{pmatrix} \begin{pmatrix} \gamma_{n\uparrow} \\ \gamma^\dagger_{n\downarrow} \end{pmatrix}. \tag{1.13}$$

The same commutation relation can also be obtained from Eq. 1.5,

$$[c_{i\mu\sigma}, H] = \sum_j \left(\mathcal{H}_{i\mu j\nu\sigma} c_{j\nu\sigma} + \Delta_{i\mu j\nu} c^\dagger_{j\nu\bar{\sigma}} \right), \tag{1.14}$$

$$\left[c^\dagger_{i\mu\bar{\sigma}}, H\right] = \sum_j \left(-\mathcal{H}_{j\nu i\mu\bar{\sigma}} c^\dagger_{j\nu\bar{\sigma}} + \Delta^*_{i\mu j\nu} c_{j\nu\sigma} \right). \tag{1.15}$$

By using the conjugate condition

$$\mathcal{H}^*_{i\mu j\nu\sigma} = \mathcal{H}_{j\nu i\mu\sigma},$$

and the relationship shown in Eq. 1.6 and 1.7, we can have

$$\begin{aligned} \begin{pmatrix} [c_{i\mu\sigma}, H] \\ \left[c^\dagger_{i\mu\bar{\sigma}}, H\right] \end{pmatrix} &= \sum_j \begin{pmatrix} \mathcal{H}_{i\mu j\nu\uparrow} & \Delta_{i\mu j\nu} \\ \Delta^*_{i\mu j\nu} & -\mathcal{H}^*_{j\nu i\mu\downarrow} \end{pmatrix} \begin{pmatrix} c_{j\nu\uparrow} \\ c^\dagger_{j\nu\downarrow} \end{pmatrix} \\ &= \sum_{j,n} \begin{pmatrix} \mathcal{H}_{i\mu j\nu\uparrow} & \Delta_{i\mu j\nu} \\ \Delta^*_{i\mu j\nu} & -\mathcal{H}^*_{j\nu i\mu\downarrow} \end{pmatrix} \begin{pmatrix} u^n_{j\nu\uparrow} & -v^{n*}_{j\nu\uparrow} \\ v^n_{j\nu\downarrow} & u^{n*}_{j\nu\downarrow} \end{pmatrix} \begin{pmatrix} \gamma_{n\uparrow} \\ \gamma^\dagger_{n\downarrow} \end{pmatrix}. \end{aligned} \tag{1.16}$$

Comparing the coefficients of $\gamma_{n\sigma}$ and $\gamma^\dagger_{n\sigma}$ of Eq. 1.13 and 1.16, we can obtain the BdG equations:

$$\sum_j^N \begin{pmatrix} \mathcal{H}_{i\mu j\nu\uparrow} & \Delta_{i\mu j\nu} \\ \Delta^*_{i\mu j\nu} & -\mathcal{H}^*_{j\nu i\mu\downarrow} \end{pmatrix} \begin{pmatrix} u^n_{j\nu\uparrow} \\ v^n_{j\nu\downarrow} \end{pmatrix} = E_{n\uparrow} \begin{pmatrix} u^n_{j\nu\uparrow} \\ v^n_{j\nu\downarrow} \end{pmatrix}, \tag{1.17}$$

$$\sum_{j}^{N}\begin{pmatrix} \mathcal{H}_{i\mu j\nu\uparrow} & \Delta_{i\mu j\nu} \\ \Delta^{*}_{i\mu j\nu} & -\mathcal{H}^{*}_{j\nu i\mu\downarrow} \end{pmatrix}\begin{pmatrix} -v^{n*}_{j\nu\uparrow} \\ u^{n*}_{j\nu\downarrow} \end{pmatrix} = -E_{n\downarrow}\begin{pmatrix} -v^{n*}_{j\nu\uparrow} \\ u^{n*}_{j\nu\downarrow} \end{pmatrix}. \tag{1.18}$$

The BdG equations above are two eigen-system problems, these two equation groups can be further written in a more compact form. We can combine these two groups of equations into one by defining $E_n = E_{n\uparrow}$ when $1 \leq n \leq N$, and $E_n = -E_{(n-N)\downarrow}$, $u^n_{j\nu\uparrow} = -v^{n-N*}_{j\nu\uparrow}$, $v^n_{j\nu\downarrow} = u^{n-N*}_{j\nu\downarrow}$ when $N+1 \leq n \leq 2N$. By these definitions, the BdG equations can be reduced to have only one group of equations:

$$\sum_{j}^{2N}\begin{pmatrix} \mathcal{H}_{i\mu j\nu\uparrow} & \Delta_{i\mu j\nu} \\ \Delta^{*}_{i\mu j\nu} & -\mathcal{H}^{*}_{j\nu i\mu\downarrow} \end{pmatrix}\begin{pmatrix} u^{n}_{j\nu\uparrow} \\ v^{n}_{j\nu\downarrow} \end{pmatrix} = E_n\begin{pmatrix} u^{n}_{j\nu\uparrow} \\ v^{n}_{j\nu\downarrow} \end{pmatrix}. \tag{1.19}$$

Eq. 1.19 is the form of BdG equations that is widely used in research works, and is also used in the following chapters. By solving for the eigenvalues and eigenvectors in the BdG equations, the quasiparticle energies E_n and the transformation coefficients defined in Eq. 1.6 and 1.7 $u^n_{j\nu\uparrow}$ and $v^n_{j\nu\downarrow}$ can be obtained.

Now we have found the new base in which the Hamiltonian is a diagonal matrix. The relation between the new base and original electron-operator base is expressed in Eq. 1.6 and 1.7. By using the solved parameters, some physical quantities of the system can be obtained. First we can calculate the local electron density in the system. The electron density for spin up can be expressed as

$$\begin{aligned} \langle n_{i\mu\uparrow}\rangle &= \left\langle c^{\dagger}_{i\mu\uparrow}c_{i\mu\uparrow}\right\rangle \\ &= \sum_{n}^{N}\left|u^{n}_{i\mu\uparrow}\right|^2\left\langle\gamma^{\dagger}_{n\uparrow}\gamma_{n\uparrow}\right\rangle + \sum_{n}^{N}\left|v^{n}_{i\mu\uparrow}\right|^2\left\langle\gamma_{n\downarrow}\gamma^{\dagger}_{n\downarrow}\right\rangle \\ &= \sum_{n}^{N}\left|u^{n}_{i\mu\uparrow}\right|^2 f(E_n) + \sum_{n=N+1}^{2N}\left|u^{n}_{i\mu\uparrow}\right|^2 f(E_n) \\ &= \sum_{n}^{2N}\left|u^{n}_{i\mu\uparrow}\right|^2 f(E_n), \end{aligned} \tag{1.20}$$

here $f(E_n)$ is the Fermi function. Similarly we can get the electron density for spin down

$$\begin{aligned}
\langle n_{i\mu\downarrow}\rangle &= \left\langle c^{\dagger}_{i\mu\downarrow}c_{i\mu\downarrow}\right\rangle \\
&= \sum_{n}^{N}\left|v^{n}_{i\mu\downarrow}\right|^{2}\left\langle \gamma_{n\uparrow}\gamma^{\dagger}_{n\uparrow}\right\rangle + \sum_{n}^{N}\left|u^{n}_{i\mu\downarrow}\right|^{2}\left\langle \gamma^{\dagger}_{n\downarrow}\gamma_{n\downarrow}\right\rangle \\
&= \sum_{n}^{N}\left|v^{n}_{i\mu\downarrow}\right|^{2}\left[1-f(E_n)\right] + \sum_{n=N+1}^{2N}\left|v^{n}_{i\mu\downarrow}\right|^{2}\left[1-f(E_n)\right] \\
&= \sum_{n}^{2N}\left|v^{n}_{i\mu\downarrow}\right|^{2}\left[1-f(E_n)\right]. \qquad (1.21)
\end{aligned}$$

The electron density is an essential order parameter to indicate the magnetization order and SDW order.

The pairing order parameter can show the amount of electrons which can form Cooper pairs, and is a very good indicator of superconductivity. The pairing order parameter can be defined and obtained from

$$\begin{aligned}
\Delta_{i\mu j\nu} &= \frac{V}{2}\left\langle c_{i\mu\uparrow}c_{j\nu\downarrow} - c_{i\mu\downarrow}c_{j\nu\uparrow}\right\rangle \\
&= \frac{V}{2}\sum_{n}^{N} u^{n}_{i\mu\uparrow}v^{n*}_{j\nu\downarrow}\left\langle \gamma_{n\uparrow}\gamma^{\dagger}_{n\uparrow}\right\rangle - v^{n*}_{i\mu\uparrow}u^{n}_{j\nu\downarrow}\left\langle \gamma^{\dagger}_{n\downarrow}\gamma_{n\downarrow}\right\rangle \\
&\quad -u^{n}_{j\nu\downarrow}v^{n*}_{i\mu\downarrow}\left\langle \gamma_{n\downarrow}\gamma^{\dagger}_{n\downarrow}\right\rangle + v^{n*}_{j\nu\downarrow}u^{n}_{i\mu\uparrow}\left\langle \gamma^{\dagger}_{n\uparrow}\gamma_{n\uparrow}\right\rangle \\
&= \frac{V}{2}\sum_{n}^{N} -v^{n*}_{i\mu\uparrow}u^{n}_{j\nu\downarrow}\left[f(E_{n\downarrow}+f(-E_{n\downarrow}))\right] \\
&\quad + \sum_{n}^{N} u^{n}_{i\mu\uparrow}v^{n*}_{j\nu\downarrow}\left[f(-E_{n\uparrow})+f(E_{n\uparrow})\right] \\
&= \frac{V}{2}\sum_{n}^{2N}\left[u^{n}_{i\mu\uparrow}v^{n*}_{j\nu\downarrow}f(-E_n) - v^{n*}_{i\mu\downarrow}u^{n}_{j\nu\uparrow}f(E_n)\right] \\
&= \frac{V}{4}\sum_{n}^{2N}\left(u^{n}_{i\mu\uparrow}v^{n*}_{j\nu\downarrow} + v^{n*}_{i\mu\downarrow}u^{n}_{j\nu\uparrow}\right)\left[1-2f(E_n)\right] \\
&= \frac{V}{4}\sum_{n}^{2N}\left(u^{n}_{i\mu\uparrow}v^{n*}_{j\nu\downarrow} + v^{n*}_{i\mu\downarrow}u^{n}_{j\nu\uparrow}\right)\tanh\left(\frac{\beta E_n}{2}\right). \qquad (1.22)
\end{aligned}$$

Typically the s±-wave symmetry pairing order is induced by a NNN pairing, which means that the V in Eq. 1.22 has a non-zero value only when i and j are next-nearest neighbors. However if d-wave symmetry appears, then NN pairings should also be taken into consideration in some systems, for example the highly electron-doped KFe_2Se_2 sample which will be further discussed in chapter 3. In such cases the V in Eq. 1.22 has a non-zero value not only when i and j are next-nearest neighbors but also when they are nearest neighbors.

In order to solve the eigensystem problem from the BdG equations as shown in 1.19, the electron density $\langle n_{i\mu\uparrow}\rangle$, $\langle n_{i\mu\downarrow}\rangle$ and pairing order parameter $\Delta_{i\mu j\nu}$ shounld be set up before obtaining the eigen values E_n and eigen vectors $u^n_{j\nu\uparrow}$, $v^n_{i\mu\downarrow}$. However according to equations 1.20, 1.21, and 1.22, the calculated results should satisfy those self-consistent conditions; otherwise they are not solutions for the actual system. In order to obtain the self-consistent solution, initially the electron density and pairing order parameter are given some initial values. By solving the eigen system problem a new set of conditions are calculated and served as new initial values, this iteration is continued until the self-consistent condition is satisfied. More numerical details about solving BdG equations will be discussed in Sec. 1.6.

1.5 Supercell and local density of states

Magnetic, SC, and charge density order parameters reflect the system's local electronic properties. However, these parameters are very hard to be measured directly in an experiment. LDOS is also very helpful to understand the behavior of a system's

local electronic properties, and can be directly measured in a STM experiment. So it is very important for us to calculate the LDOS based on our model in order to compare the theoretical calculation results directly with the experimental measurements. The resolution of LDOS spectra depends on the size of lattice in the calculation. A supercell technique was developed by J. Zhu [59] to improve the resolution in the LDOS calculation.

The BdG equations (Eq. 1.19) in the previous section are solved within the lattice size $N_x \times N_y$. By using the periodic boundary condition, this $N_x \times N_y$ lattice can be treated as a unit cell (or can be called a supercell) in a larger system which has $M_x \times M_y$ such supercells. According to Bloch's theorem, the wave functions in a Bloch's state will have the property

$$\psi_{n\mathbf{k}}(r_i) = e^{i\mathbf{k}\cdot\mathbf{r}} u_{n\mathbf{k}}(r_i), \tag{1.23}$$

where $u_{n\mathbf{k}}(r_i)$ is a function which remains unchanged among different supercells. $\mathbf{k}$ is the Bloch wave vector, and can be expressed as $k_x\hat{x} + k_y\hat{y}$ where

$$k_x = \frac{2\pi m_x}{M_x N_x} \qquad m_x = 0, 1, \cdots, M_x - 1 \tag{1.24}$$

$$k_y = \frac{2\pi m_y}{M_y N_y} \qquad m_y = 0, 1, \cdots, M_y - 1. \tag{1.25}$$

Then the BdG equations Eq. 1.19 can be rewritten as

$$\sum_{j}^{2N} \begin{pmatrix} \mathcal{H}_{i\mu j\nu\uparrow} e^{i\mathbf{k}\cdot\mathbf{r}} & \Delta_{i\mu j\nu} e^{i\mathbf{k}\cdot\mathbf{r}} \\ \Delta^*_{i\mu j\nu} e^{-i\mathbf{k}\cdot\mathbf{r}} & -\mathcal{H}^*_{j\nu i\mu\downarrow} e^{-i\mathbf{k}\cdot\mathbf{r}} \end{pmatrix} \begin{pmatrix} u^n_{j\nu\uparrow} \\ v^n_{j\nu\downarrow} \end{pmatrix} = E_n \begin{pmatrix} u^n_{j\nu\uparrow} \\ v^n_{j\nu\downarrow} \end{pmatrix}, \tag{1.26}$$

here $\mathbf{r} = \mathbf{r_i} - \mathbf{r_j}$ is the distance vector from lattice site i to j. By solving the BdG equations with different Bloch wave vectors $\mathbf{k}$ in every supercell, the solution for a system totally sized $M_x N_x \times M_y N_y$ will be obtained.

According to a thermal Green's function calculation [60], the LDOS from BdG equations can be obtained from

$$\rho_i(\omega) = \frac{1}{M_x M_y} \sum_{n\mu}^{2N} \sum_{\mathbf{k}} [\left|u_{i\mu\uparrow}^{n\mathbf{k}}\right|^2 \delta(E_{n\mathbf{k}} - \omega) + \left|v_{i\mu\downarrow}^{n\mathbf{k}}\right|^2 \delta(E_{n\mathbf{k}} + \omega)], \tag{1.27}$$

here $\mathbf{k}$ is the Bloch wave vector, the summation over $\mathbf{k}$ needs to sum over every possible value of $\mathbf{k}$, which means $M_x \times M_y$ supercells. The LDOS is averaged over $M_x \times M_y$ supercells, which gives the result in only one supercell sized $N_x \times N_y$. The resoluation of LDOS depends on the total number of eigenstates in the system. Bringing the supercells in the system greatly increase the number of eigenstates, therefore it helps to improve the resolution in the calculation of LDOS. However the cost is the considerable computing time to solve the BdG equations in each supercell, the final resolution of LDOS is still limited by computing abilities.

1.6 Numerical realization of BdG equations

In this section, several issues about the numerical realization of BdG equations in the program are discussed. There are four major parts in the program: the initialization part, the diagonalization part, the self-consistent part, and the output part. In the initialization part, the elements in the Hamiltonian matrix of Eq. 1.19 are set up. At first a 1-D array $\mathbf{A}$ is declared. With lattice size $N_x \times N_y$, the size of the array would be $(N_x \times N_y \times 2)^2$. This size can be used to estimate the memory cost of the program. This array is used to store the Hamiltonian matrix. The matrix element at i-th row and j-th column can be stored at the $[i \times (N_x \times N_y \times 2) + j]$-th position of the array. Such a 1-D array storage structure is required by the matrix diagonalization

package which will be discussed in the next paragraph. One big problem in this part is that a set of initial values of pairing orders and electron density orders should be given before they can be calculated. By principle there is no restrictions on the initial values as long as they are non-zero. However several numerical tricks can be played here to speed up the program. Apparently the program will converge faster if the initial condition is relatively close to the final one. Therefore it is very important to set up an initial condition that is not far away from the final result. For example, if the FeAs-122 family parent compound is studied, since there is strong magnetization and no SC orders in the system, then the initial SC orders should be set a small value and magnetization should have a large one. Another way to set up the initial values is to use an output of another calculated system. This is very useful when the new system is very close to the old one. For example it can be used in the impurity calculation from the system without impurity to the system with single impurity, and the phase diagram calculation from one doping level to another neighboring one.

The diagonalization part of the program solves the eigen system problem in Eq. 1.19, and the eigenvalues and eigenfunctions are obtained. A lot of effort has been made in this part since it is the most time-consuming part in the whole program. If the calculation is done on a CPU, the *cheev*() function included in the Linear Algebra Package (LAPACK) developed by Intel is called to diagonalize the matrix. The data structure and input/output formations can be found in the comment part of the function. This function can be accelerated on a GPU machine, it is because unlike CPU, the GPU can run program in parallel. A numerical package named MAGMA based on CUDA language is used to make the program work on GPU. According to

my experience, the GPU program can run 10 times faster than the CPU one when diagonalizing the same matrix.

Now that the eigenvalues and eigenfunctions in Eq. 1.19 have been obtained, the next step is the self-consistent part. The pairing order and electron density order are calculated according to Eq. 1.20, 1.21, and 1.22. The newly calculated orders are compared with those calculated in the previous step. If the new orders are the same as the previous ones, then the system has converged; or else the new orders will be used as initial values in the new loop. Practically setting up the initial values totally from the newly calculated orders may result in an oscillation between two bouncing states, and the program will never converge then. A better way to do it is that the initial values are set by an average of new and old orders. Another numerical trick in this part is to adjust the chemical potential. We know that the electron filling is decided by the value of chemical potential. In order to reach the target electron doping level, the chemical potential has to be adjusted. In order to control the fluctuations in the program, the chemical potential is changed every four loops in the form $t_{new} = t_{old} - (N - N_0) \times 0.2$, here t_{old} and t_{new} are the chemical potentials before and after the adjustment, N is the calculated average electron density and N_0 is the target electron doping level, the coefficient 0.2 can be altered according to different situations in the program.

After the program converges, magnetic order, SC order and electron density order parameters can be calculated and output to the files. Here comes the output part. The output data formation can be chosen case by case, depending on the graphic method afterward. Only non-zero elements of Δ matrix are necessary to output to

file. Since the program may take as long as a couple of weeks time, it is highly recommended to output temporary files after several loops. Then one does not have to run everything from the very beginning if the program is shut down accidently.

1.7 Overview of chapters

In this section I would like to briefly introduce the following chapters. The magnetic domain wall structure observed near twin-boundary structure in several Fe-based HTS was reported. Interestingly the SC order will be enhanced along some of the twin boundaries. Therefore in chapter 2, the magnetic, SC, and electron density properties of magnetic domain walls induced by twin boundaries are studied in the electron-under-doped region of $BaFe_2As_2$. Four different types of twin boundaries are investigated. The pairing symmetry type plays an essential role in understanding the SC order, and the discovery of robust SC phase in doped $A_xFe_2Se_2$ system provides us a possible way to study the SC and pairing symmetry in highly electron-doped regime of FeAs-122 family HTS. In chapter 3, the NN pairing additional to the NNN one is added in the Hamiltonian. The phase diagram is calculated based on the new model and predictions of LDOS near a single impurity are made. Vortex core states can be formed in Fe-based HTS under the effect of external magnetic field. Such a state is able to provide information of magnetic and electronic properties of the system. So in chapter 4, a single strong non-magnetic Zn impurity is placed in the center of vortex core when the system is under the effect of magnetic field. The LDOS spectra is calculated in order to be compared to the impurity away from the

vortex core. Inspired by the recent Zn impurity experiments, the impurity effect based on a single orbital Zn model is studied in chapter 5. The LDOS spectra near single impurity and the evolution of multiple impurity effect are discussed. The calculated suppression of SC order with different concentrations of Zn impurities agrees quantitatively with the experimental data.

Chapter 2

Magnetic domain walls induced by twin boundaries in low-doped Fe-pnictides

2.1 Introduction

Most of the work in this chapter was shown in a published paper [1]. Recently, twin boundaries (TBs) oriented 45° from the x(a)-axis were observed in the normal state of $Ca(Fe_{1-x}Co_xAs)_2$ by STM experiments [15]. Across these TBs, the a-axis of the crystal rotates by 90°, and the modulation direction of AF order that exists is rotated by 90° as well. That is, 90° magnetic domain walls (DWs) are formed at the TBs. Also, in the SC state of under-doped $Ba(Fe_{1-x}Co_xAs)_2$ with $x < 0.07$, it has been

[1] B. Li, J. Li, K. E. Bassler, and C. S. Ting, *New J. Phys.*, 15:103018, 2013

found that the diamagnetic susceptibility is increased and that the superfluid density is enhanced on the same type of TB in superconducting-quantum-interference-device miscroscopy (SQIDM) experiments [16]. Consistent with these experiments, a theoretical study [61] found that 90° DWs can be formed at low doping levels and that SC is enhanced on them. However, the DWs considered in that study were formed in the absence of TBs, and were induced instead by a strong effective Coulomb interaction between charge carriers, while in the experiments [15, 16] the DWs were pinned at TBs.

In this chapter, in order to better understand the effects that TBs have on the spatial profiles of magnetic and superconducting order, I investigate the magnetic, SC, and charge density orders near two different types of TBs using the BdG equations for very under-doped Ca(or Ba)$(FeAs)_2$ compounds. The lattices on the opposite sides of the type-1 TB have a 90° orientation difference, and the As atoms across the type-2 TB are asymmetrically placed. I predict that the enhancement or suppression of SC, the location of DWs and the electron-density distributions are largely dependent on the nature of TBs. The relationship between magnetism, SC and the charge order is always one of the most important problems in the research of unconventional superconductors. Our work provides the first study on different kinds of twin boundaries, which involves all the three aspects mentioned above. More importantly, it shows where and how the superconductivity can be enhanced/suppressed in the presence of TBs.

2.2 Hamiltonian and methodology

In this chapter D. Zhang's model discussed in Sec. 1.3 is used to do the calculation. As mentioned in Sec. 1.3, this model works well in the electron-doped region. Since all the calculations here are in electron-under-doped region, the model is valid here. Consider the Hamiltonian $H = H_0 + H_{SC} + H_{int}$ that describes the energy of charge carriers. H_0 is the hopping terms and chemical potential, H_{SC} is the pairing interaction energy of the electrons, and H_{int} is the mean-field magnetic interaction energy. The specific forms of these three terms can be found in Eq. 1.2, 1.3, and 1.4. The eigenvalues and eigenfunctions of the total Hamiltonian H can be obtained by self-consistently solving the BdG equations shown in Eq. 1.19. The chemical potential t_0 is determined by the electron filling per site n ($n = 2 + x$), and for the values of the hopping terms, $t_{i\mu j\nu}$ are assumed to be $t_{(1-4)} = (1, 0.4, -2, 0.04)$ according to [53, 54]. Only the electron pairings of the same orbital between the NNN Fe sites are considered. For example, I choose $V_{i\mu j\nu} = 1.4$ for $\mu = \nu$ and $|i - j| = \sqrt{2}$, and zero for all other cases. As mentioned in Sec. 1.4, this choice of the pairing potential gives rise to the SC order with $s_{\pm}$-wave symmetry [62, 63].

The numerical steps to solve the system in this chapter are basically the same as discussed in Sec. 1.6. The only difference is that the hopping terms here are not uniform. The hopping terms along x- and y-directions in different domains have different values. One needs to be very careful to set these values especially near the TBs and lattice boundaries. Since the periodic boundary condition is used, it is very important to make the TBs continuous at the lattice boundaries. Otherwise

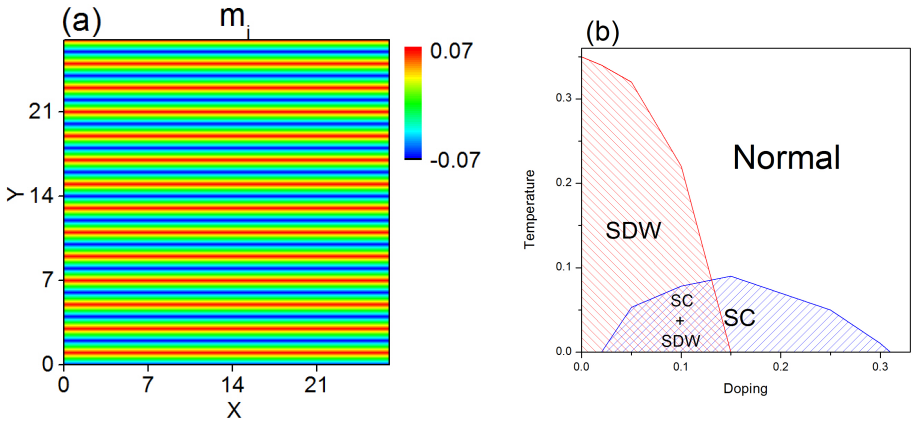

Figure 2.1: (a) The orientations of magnetic moments of Fe ions on a 28×28 lattice at zero temperature and doping $x = 0.04$. (b) The phase diagram as a function of electron doping (x).

the boundary effects will make the system too complicated to be studied.

2.3 Phase diagram

The phase diagram of the electron-doped $Ba(Fe_{1-x}Co_xAs)_2$ compounds as a function of temperature T and doping x has been qualitatively mapped out with $U = 3.4$, $J_H = 1.3$, and the NNN pairing interaction $V = 1.2$ [54]. The distribution of the 2×1 collinear AF order and the SC order are spatially uniform. In reality, the lattice in the Fe-plane of these compounds is almost square, having slightly different lattice constants a and b ($a > b$) along x- and y-directions [64]. In the present work, nearest-neighbor hoping terms are chosen to be $t_a = 1.0$ and $t_b = 1.2$. I also slightly increase the magnitudes of our interaction parameters ($U = 3.8$, $J_H = 1.3$, and $V = 1.4$) in order to generate more pronounced inhomogeniety of the order parameters near the TBs. With the new set of the interaction parameters, I recalculate the magnetic

configuration at $x = 0.4$ on a 28×28 lattice and the phase diagram as a function of the electron doping which are respectively shown in Fig. 2.1(a) and (b). Fig. 2.1(a) exhibits the 2×1 collinear AF order, where the spins of the Fe ions on the red lines are pointing upward, and the spins on the blue lines are pointing downward. Since the magnetic order is originated in itinerant interacting electrons, the magnetic configuration in Fig. 2.1(a) is also refered as the SDW order. The spins of the Fe ions are always aligned ferromagnetically along a (or x)-direction. The obtained phase diagram indicates that the SC order is completely suppressed by the SDW near $x = 0$. The SDW and SC are coexisting with each other between $x \sim 0.02$ and $x \sim 0.15$. For $x > 0.15$ while the SDW order disappears, the SC still prevails. All these features in our phase diagram are in qualitative agreements with both surface- and bulk-sensitive experiments [33, 65–68].

2.4 Magnetic domain-wall structures and twin boundaries

In the absence of the TBs, the SDW order discussed above is unstable against the formation of the 90° magnetic DWs oriented 45° from the x-axis as the strength of U is increased to $U = 4.8$ for small x at $T = 0$ [61]. In the presence of TBs, the magnetic DWs could be formed at much weaker U as demonstrated in the present work. There are two types of TBs. The first one is that the orientations of the lattices across the TB differ by a 90° rotation. The second one is that the As atoms are asymmetrically placed across the TB as compared with a perfect crystal lattice.

For each type of the TBs, there are two configurations: one is oriented along 90° from x-axis and the other is oriented along 45° from the x-axis. In the following, the spatial profiles of magnetic, SC and charge density order near four different TBs at $T = 0$ are investigated. Throughout this work, I set $x = 0.04$, $U = 3.8$, $J_H = 1.3$ and $V = 1.4$. Note that DWs do not form spontaneously in the absence of TBs at these parameter values, and all the order parameters have uniform solutions.

2.4.1 A. Type-1 twin boundary oriented 45° from the x-axis

TBs can be formed by exchanging the lattice constants a and b on the opposite side of the TB. Fig. 2.2(a) shows the structure of a single such TB oriented at 45° with respect to the x-axis. Since the magnitude of a is lightly larger that that of b, this TB can be realized by assuming slightly different NN hoping terms $t_a = 1.0$ and $t_b = 1.2$ across the TB. To analyze the effect of this TB, I considered a 28×28 lattice divided into 4 different domains separated by three parallel TBs (see Fig. 2.2(a)) along the lines $y = x + 14$, $y = x$ and $y = x - 14$, in order to satisfy the periodic boundary conditions. As shown in Fig. 2.2(b) and Fig. 2.3(a), there are three 90° DWs formed and pinned on the TBs. The patterns of these quantities are very similar to those found in [61] without the TBs (see Fig. 2(a)-(c) in [61]). However, in this case, the DW forms with a smaller value of the Coulomb interaction U, indicating that the existence of this type of TB is beneficial to the formation of the 90° DWs. The solutions presented in Fig. 2.3 are always stable against the uniform 2×1 collinear AF order [54].

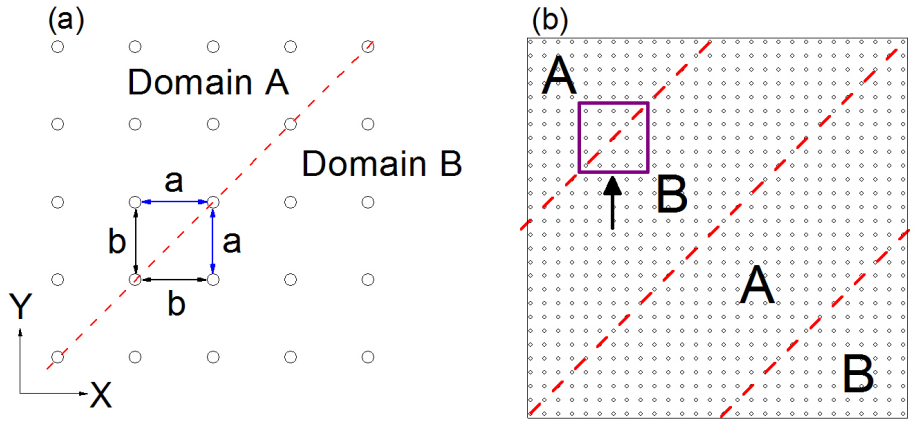

Figure 2.2: (a) The lattice structure near a diagonal TB (red dashed line), the open circles represent the positions of Fe atoms, a (blue solid line) and b (black solid line) are the lattice constants along x and y directions in domain A. (b) Three TBs in the 28×28 lattice, the black arrow indicates the position of the lattice structure shown in (a) in the whole lattice.

Similar to the results without TBs [61], the SC as well as the charge density get significantly enhanced on the DWs, which occur at the TBs, and suppressed in the middle of the magnetic domains (see Fig. 2.3(b) and (c)). All of these are in good agreement with experiments [15, 16]. It is important to note that the lattices on both sides of this TB should be well matched at the TB, and each of the unit cells along the TB is only slightly deformed from the square shape. Thus, I do not expect that scattering of the electrons from the lattice mismatch across the TB would be strong.

2.4.2 B. Type-1 twin boundary oriented 90° from the x-axis

A TB formed by exchanging the a and b lattice constants across it can also be oriented parallel to the x- or y-axis (as shown in Fig. 2.4(a)). The periodic boundary condition

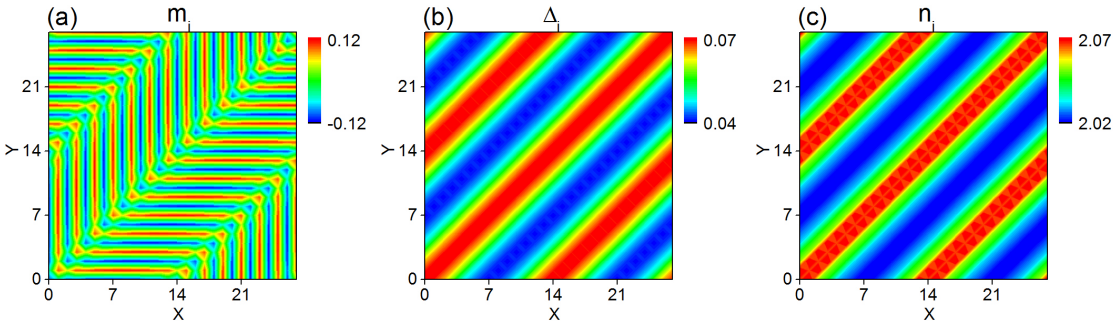

Figure 2.3: Spatial profiles of (a) the magnetic order, (b) the superconducting order, and (c) the charge density order are presented for type-1 TB oriented 45° from the x-axis.

of this case is achieved by dividing the system into 3 different domains separated by two TBs (see Fig. 2.4(a)) along the lines $x = 7$ and $x = 20$, as shown in Fig. 2.4(b).

Here the magnetic DWs are pinned at the TBs (see Fig. 2.5(a)) on which existing a weak local ferromagnetic order which a periodic modulation. The SC also has a similar periodic modulation and is enhanced on the DWs, but suppressed in the middle of the magnetic domains (see Fig. 2.5(b)). A charge density wave appears near the DWs (see Fig. 2.5(c)), while the electron density gets suppressed in the middle of the magnetic domains. It is important to point out that in this case, the lattices on the opposite sides of a TB are not well matched. Therefore, there may be considerable scattering of the electrons due to the lattice mismatches near these TBs. If this effect is included, I expect that the SC would get suppressed, instead of being enhanced when the mismatch becomes strong across the DWs or the TBs. This issue will be discussed in Section 2.5.

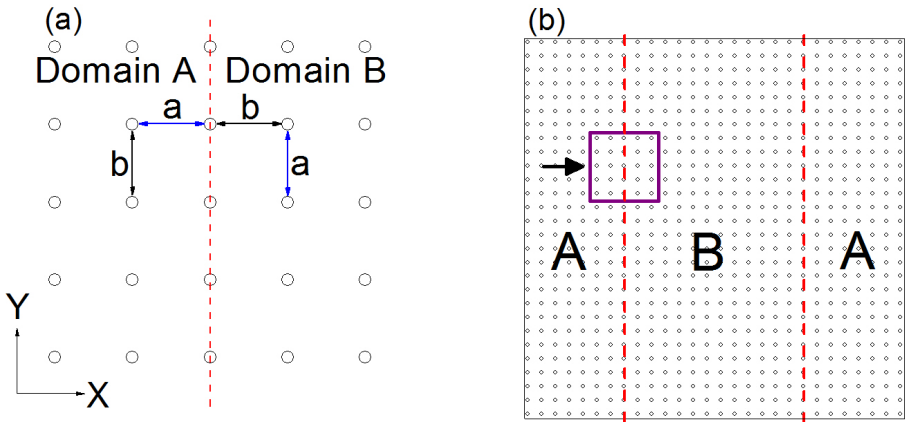

Figure 2.4: (a) The lattice structure near a TB parallel to the y-direction (red dashed line), the open circles represent the positions of Fe atoms, a (blue solid line) and b (black solid line) are the lattice constants along x and y directions in domain A. (b) Two TBs in the 28×28 lattice, the black arrow indicates the position of the lattice structure shown in (a) in the whole lattice.

2.4.3 C. Type-2 twin boundary oriented 90° from the x-axis

Another possible TB can be generated by slipping the lattice on the right side of the TB by a lattice constant along the y-direction with respect to the lattice on the left of the TB. There are two different types of As atoms in our model. I label them as As(up) and As(down) atoms which are asymmetrically place above and below the Fe plane. This type of TBs can be clearly seen from Fig. 2.6(a), in which the TB is represented by the red-dashed line. The crystal lattice for the FeAs layer has D_{2d} symmetry; namely the 4 NN As atoms of a 'down'-As atom should be all 'up'. The hopping terms between the NNN Fe ions via the hybridization of the 4p orbital with the As atom in the middle should have different values depending on whether the As atom is above (t_2) or below (t_3) the Fe plane [53, 69]. The D_{2d} symmetry is broken by the presence of the TB. I considered a 28×28 lattice with periodic

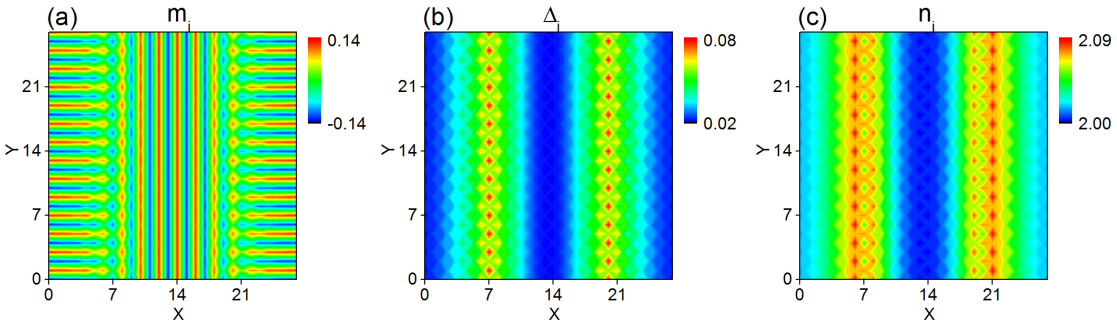

Figure 2.5: Spatial profiles of (a) the magnetic order, (b) the superconducting order, and (c) the charge density order are presented for type-1 TB oriented 90° from the x-axis.

boundary conditions divided into three domains by two TBs located at $x = 7$ and $x = 20$ (see Fig. 2.6(b)). Fig. 2.7(a) shows the magnetic order is enhanced near the TBs. The magnetic DWs are defined to be where the magnetic order is suppressed, that is, near the middle between two TBs. Then, clearly, the DWs are not located at the TBs. On the opposite sides of a DW, there is no change in the magnetic phase, thus I could label the DWs as the 0-phase DWs. Fig. 2.7(b) shows that the SC is enhanced along the DWs, and that it is suppressed near the TBs. Fig. 2.7(c) shows that the electron density is depleted near the TBs and becomes lightly hole doped. Apparently, the depleted electron density leads to strong magnetic order that suppresses the SC order. On the DWs, the electron density appears to be close to optimal-doping, thus SC gets enhanced and the magnetic order is suppressed. I shall also point out in Sec. 2.6 that the magnetic and SC structures near a TB oriented 0° from the x-axis are very different from the present case, and antiphase DWs are predicted.

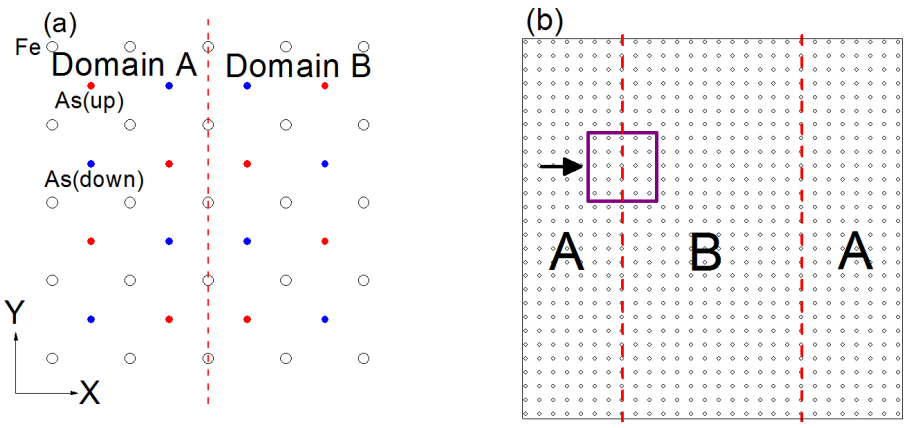

Figure 2.6: (a) The lattice structure near a twin boundary (red-dashed line) parallel to the y-direction formed by misplacing As atoms. The open circles represent the positions of Fe atoms, and the red and blue dots respectively denote the As(up) and As(down) atoms. (b) Two TBs in the 28×28 lattice, the black arrow indicates the position of the lattice structure shown in (a) in the whole lattice.

2.4.4 D. Type-2 twin boundary oriented 45° from the x-axis

A TB due to missing one line of the lattice which contains both Fe and As(down) atoms oriented along 45° from the x-axis is shown in Fig. 2.8(a). In fact this "TB" could also be regarded a line of missing Fe-As atoms. The D_{2d} symmetry of the lattice is also broken by the presence of this TB. Note that the geometry of this TB is fundamentally different from the one showed in Fig. 2.6(a) since the TB does not pass through any of the Fe or As atoms. To study this case, I considered a 30×30 lattice and three identical TBs oriented 45° from the x-axis (see Fig. 2.8(b)), in order to satisfy the periodic boundary condition. The TBs are located along $y = x - 15$, $y = x$, and $y = x + 15$.

Different from the case in Fig. 2.7(a), the magnetic order shown in Fig. 2.9(a) is suppressed along the TBs where DWs are located. The magnetic domain between the

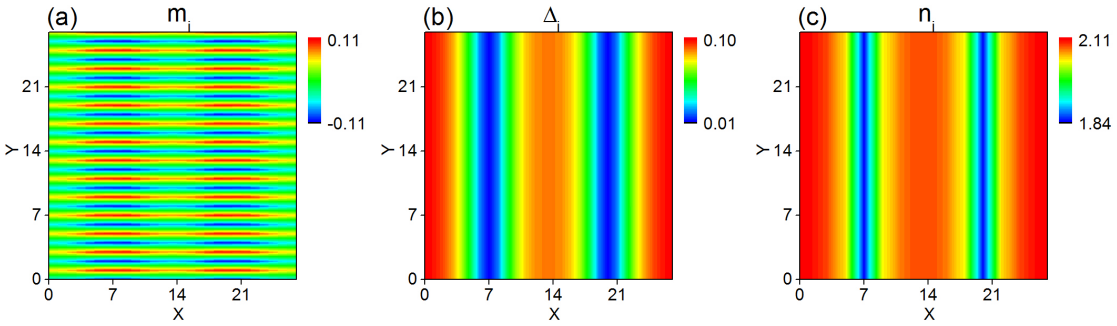

Figure 2.7: Spatial profiles of (a) the magnetic order, (b) the superconducting order, and (c) the charge density order are presented for type-2 TB oriented 90° from the x-axis.

TBs still has the usual 2×1 collinear AF structure, except the magnetic moments are strongly and periodically modulated along the x-axis, which may be due to finite size effects of the TB and the small distance between two NN TBs. It also appears that the local 2×1 collinear AF structure could be represented by a stripe-like $\sqrt{2}\times\sqrt{2}$ AF structure oriented 45° from the x-axis. Furthermore, the SC is enhanced in these regions (see Fig. 2.9(b)). From Fig. 2.9(c), I can find that on the TBs or DWs the carrier density is corresponding to that in the overly hole-doped case ($x\approx-0.3$), which explains why the magnetic and SC orders are suppressed on both sides of the TB. Interestingly, stripe-like charge density waves oriented 45° from the x-axis occur on both sides of each TB.

2.5 Twin boundary with lattice mismatch

In the previous section I assumed the lattices are well matched at the TBs. In the case that the lattice on both sides of the TB are not well matched, such as the case

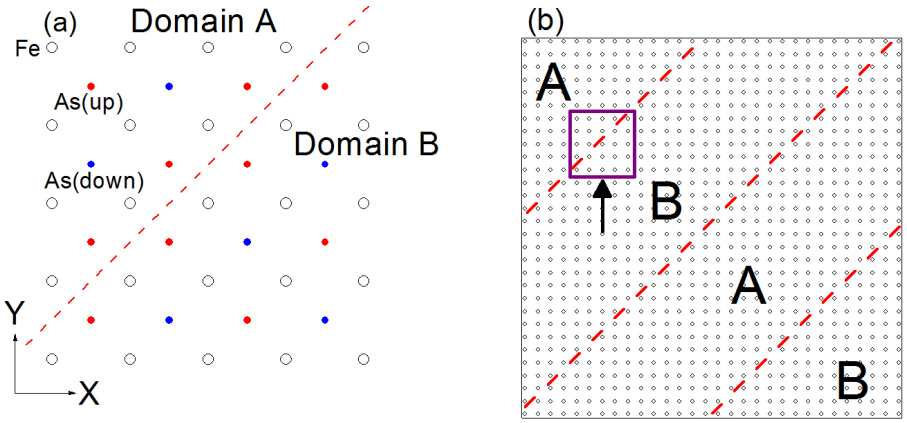

Figure 2.8: (a) The lattice structure near a twin boundary (red dashed line) with misplacing the As atoms along diagonal (or 45°) direction. The open circles represent the positions of Fe atoms, and the red and blue dots respectively denote the As(up) and As(down) atoms. (b) Three TBs in the 30×30 lattice, the black arrow indicates the position of the lattice structure shown in (a) in the whole lattice.

B in Section 2.4.2, the electrons could subject to strong disordered scattering along the TBs. To take this effect into consideration, I add an impurity-like potential of random strength to each of the Fe ions along the TBs. The Hamiltonian of this part is $H_{scat} = \sum_{s\mu\sigma} V_s c^{\dagger}_{s\mu\sigma} c_{s\mu\sigma}$, where V_s is the impurity potential at the s-th Fe site along the TBs.

Fig. 2.10 shows the magnetic order, SC order, and charge density for a random scattering potential $V_s = w$ along the TBs. The strengths of w are chosen to be randomly distributed within the ranges $(-0.5, 0.5)$, $(-1.0, 1.0)$, and $(-2.0, 2.0)$ respectively for Fig. 2.10(a), (b), (c), Fig. 2.10(d), (e), (f), and Fig. 2.10(g), (h), (i). The results are averaged over 100 configurations. In Fig. 2.10(a), (b), and (c) with weak scattering potential $w = (-0.5, 0.5)$, the periodic modulations in the magnetic, SC and the charge density orders which appearing in Fig. 2.5 are now smoothed by

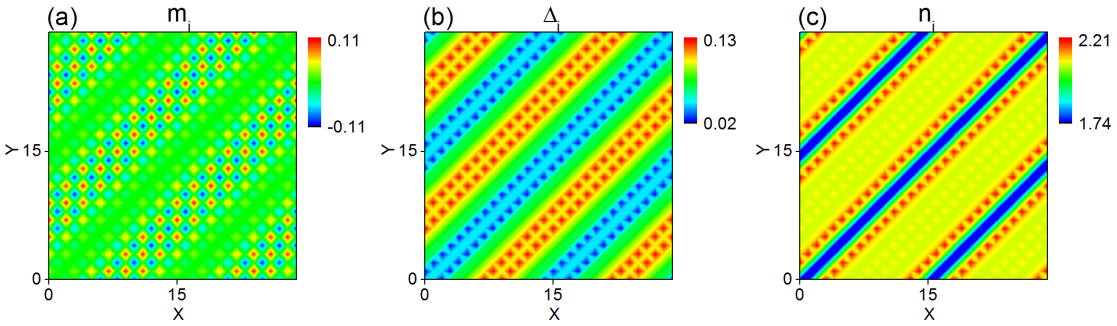

Figure 2.9: Spatial profiles of (a) the magnetic order, (b) the superconducting order, and (c) the charge density order are presented for type-2 TB oriented 45° from the x-axis.

the weak disorder. The magnetic order is somewhat suppressed along the TBs by the disorder, thus the SC gets enhanced near the DW regions. If the random potential is increased to w=$(-1.0, 1.0)$, the results are shown in Fig. 2.10(d), (e), and (f). The SC order (see Fig. 2.10(e)) is now becoming weakened as compared to that in Fig. 2.10(b). When the random potential gets strong, such as $w = (-2.0, 2.0)$, the magnetic, SC, and charge density orders are exhibited in Fig. 2.10(g), (h), and (i). In this case the SC is suppressed on the magnetic DWs. Similar results could also be obtained in cases A, C, and D if the strength of mismatch across the TBs varying from weak to strong. So far the observation of type-1 TB oriented 90° from the x-axis (as shown in case B) has not been reported in the literatures, but an unpublished work of Pan detected such a rugged-shaped kind of TB by STM experiments in $CaFe_2As_2$, and indicates that the SC order is greatly suppressed there. This is consistent with the our theoretical study in the present section.

In a very recent STM experiment for FeSe [70], similar type-1 TBs oriented 45° from the x-axis were detected, but the SC is suppressed on the TBs. This can be

explained either by the fact that the electron structure of FeSe is different from that of $Ba(Ca)(FeAs)_2$, or there exist strong disordered scatterings along the TBs.

2.6 Comparing with NMR experiments

Recently there were indirect measurements of the magnetic structures in a very under-doped or undoped $Ca(FeAs)_2$ sample by the NMR experiments [71]. The authors not only observed the magnetic DW along the 45°-oriented type-1 TB as demonstrated in Fig. 2.2(a) and 2.3(a), but also detected the antiphase magnetic DWs as indicated by the green-dashed and the black-dotted lines as shown in Fig. 2.11. The SC is found to be enhanced on these DWs. It is still unclear what type of TBs or defect lines are able to generate such antiphase DWs. Here I wish to point out that a similar antiphase DW like the black-dotted line in Fig. 2.11 could be generated by a type-2 TB (see Fig. 2.6), but oriented along x-axis. The results for the magnetic, SC, and charge density orders are shown in Fig. 2.12(a), (b) and (c) respectively. The magnetic DWs are pinned at the TBs (see Fig. 2.12(a)) with a spin-density wave of a period $4a$ existing along the DW. It is straightforward to see that the phases of the magnetic order above and below the DWs (or the TBs) in Fig. 2.12(a) differ from those in Fig. 2.7(a) by 180°. Since the charge density (see Fig. 2.12(c)) along the DWs corresponds to that of lightly hole-doped case, the SC is suppressed (see Fig. 2.12(b)). Although Fig. 2.12(a) gives rise to antiphase DWs, the SC is suppressed on them. This is not completely in agreement with experiments [71].

Since the formation of DWs may not need TBs, they could be induced by magnetic interactions [61]. It is useful to note that in the work of [61], only the magnetic DW in Fig. 2.3(a) appears to be stable at very low doping and there exist no other types of DWs. In order to understand the experimental observations, I try to numerically simulate the magnetic DWs by choosing a stronger U. What I found is that the magnetic structure shown in Fig. 2.3(a) without the TBs [61] is always stable, even when the onsite Coulomb interaction U is increased to a reasonable magnitude. As U is increased from 3.8 to 5.5, similar DWs to that indicated by the green-dashed line in Fig. 2.11 could also be generated (see Fig. 2.13(a)), in addition to the DWs in Fig. 2.3(a). The magnetic DW is defined where the magnetic order parameter is suppressed the most. On the opposite sides of the DWs, the magnetic moments of the Fe atoms point to opposite directions. This should correspond to the antiphase DWs predicted in [72]. However, the magnetic configuration in Fig. 2.13(a) appears to have slightly higher energy than that in Fig. 2.3(a), and thus it should be regarded as a meta-stable or local stable. This type of DWs may become detectable in experiments under proper local condition of the sample. In Fig. 2.13(b), the spatial distribution of the SC order parameter is presented, and it is shown that the SC order is suppressed at the middle of the magnetic domains where the charge density corresponding to that of slightly hole-doped case (see Fig. 2.13(c)), but enhanced near the boundary between the magnetic domain or the edges of the DW where the charge density corresponding to the optimal electron-doped case. On the DWs, the charge density is in the over-doped region where the magnetic order is completely suppressed. Here, it needs to be pointed out that the width of our

numerically obtained DWs as shown in Fig. 2.12(a)and 2.13(a) span several lattice constants. While in the experiments [71] (or see Fig. 2.11), the width of the DW covers only one lattice constant. This should not be the physical picture, because it would cost large exchange energy at the DW, as one line of spins is being flipped among the two adjacent spin lines close to the DW. I also spent a lot of effort trying to numerically simulate the magnetic DW indicated by the black-dotted line as shown in Fig. 2.11 using only U but no TBs. This task so far has not been successful, and it implies that the cost of energy in creating such a DW is high, because one has to flip the spins of the Fe atoms on the right-hand side of the DW in order to make the NN spins across the DW ferromagnetically oriented. Since the NMR experiments [71] have indirectly detected all the three magnetic DWs discussed above, which could indicate that their sample may not be homogeneous, so that it could accommodate all these DWs of different characteristics in different parts of the sample. It is also interesting to note that the antiphase DWs so far have not been confirmed by other more direct measurements.

In summary for this section, although the results obtained from the present work seem able to qualitatively reproduce the the antiphase DWs or boundaries as observed by experiments, the positions of the enhanced SC are not at the DWs; instead they are near the edges of the DWs. I either have to find the proper TBs or the defect lines for generating exactly the kind of antiphase DWs with the SC pinned at the DWs as observed by the NMR experiments, or the experimental measurements have to be reinterpreted.

2.7 Conclusions

Based on the BdG equations and the mean-field approach, I studied the effects of TBs on the complex interplay between the magnetism and superconductivity in slightly electron-doped $Ba(Ca)(FeAs)_2$ compounds, particularly, to examine whether the SC order would be enhanced at the TBs. There are three points that need to be emphasized here. First, the formation and the location of the DWs strongly depend on the nature of TBs. For the four kinds of TBs studied in Section 4, the DWs in cases A, B, and D are found to be pinned at the TBs, while in case C the DWs are separated from the TBs. Intuitively, the electrons are subject to additional potentials induced by the TBs. For cases A and B, these potentials are negative, and thus the electron density is slightly enhanced on the TBs. This causes a higher electron-doping level and the SC get enhanced near the TBs than on other sites. The magnetic order near the TBs in this case becomes weakened. Additionally, the 90° lattice rotation across the TB splits the degeneracy between different orientated 2×1 AF states. Therefore 90° orientated AF states are favored on different sides of the TBs, and the DWs are naturally pinned at the TBs. For cases C and D, the additional potentials for the electrons appear to be positive, and thus the electron density is decreased to such a value that the effective doping level corresponds to that of hole-doping along the TBs. For case C, the charge density along the TB is slightly hole-doped while the magnetic order is still quite strong. As a result, the SC near the TB becomes quite suppressed. As a result, the DW is located between two neighboring TBs and the SC gets much enhanced there. For case D, the charge density near the TB corresponds to the over hole-doped case. The strengths of the

magnetic order and the SC are greatly reduced there. Thus the DW is pinned near the TB. This naturally explains why the magnetic order is enhanced along the TBs in case C and becomes rather weak in case D. Moreover, the reflection symmetry with respect to the TBs is preserved in case C and broken in case D. This makes it more difficult to form a symmetric magnetic order near the TBs in case D than in case C.

Second, the formation of the DWs implies that the magnetism is inhomogeneous. This inhomogeneity is accompanied by the non-uniform distribution of the SC and the charge density orders. In cases of A, B, and C, the SC is enhanced in the regions near the DWs where the magnetic order is suppressed. The reason for this is that the electron densities are enhanced to the optimal doped level around the DWs. However in case D, on the DWs where the magnetic order is suppressed, the carrier density is close to the over(hole)-doping level, and this is also unfavorable to SC. As a result, SC coexists with the magnetism in the middle of magnetic domains. In summary, the SC along the TBs gets enhanced in cases A and B, while it is much suppressed in cases C and D. The predictions for cases C and D could be tested by measuring the superfluid density on the TBs using SQIDM [16].

Finally, I point out that our results on the type-1 TB oriented 45° from the x-axis (see Fig. 2.3) are in good agreement with experiments [15, 16]. The two types of antiphase DWs or boundaries as detected indirectly by NMR experiments [71] could also somewhat be generated respectively by a type-1 TB oriented along x-axis and a larger onsite Coulomb interaction U. The SC is found to be enhanced near the edges of the DWs, but not at the DWs as observed in the experiments. There are

two possibilities for this: one is that the calculated TBs are not the proper structure to form the antiphase DWs; the other is that the experimental measurements have to be reinterpreted.

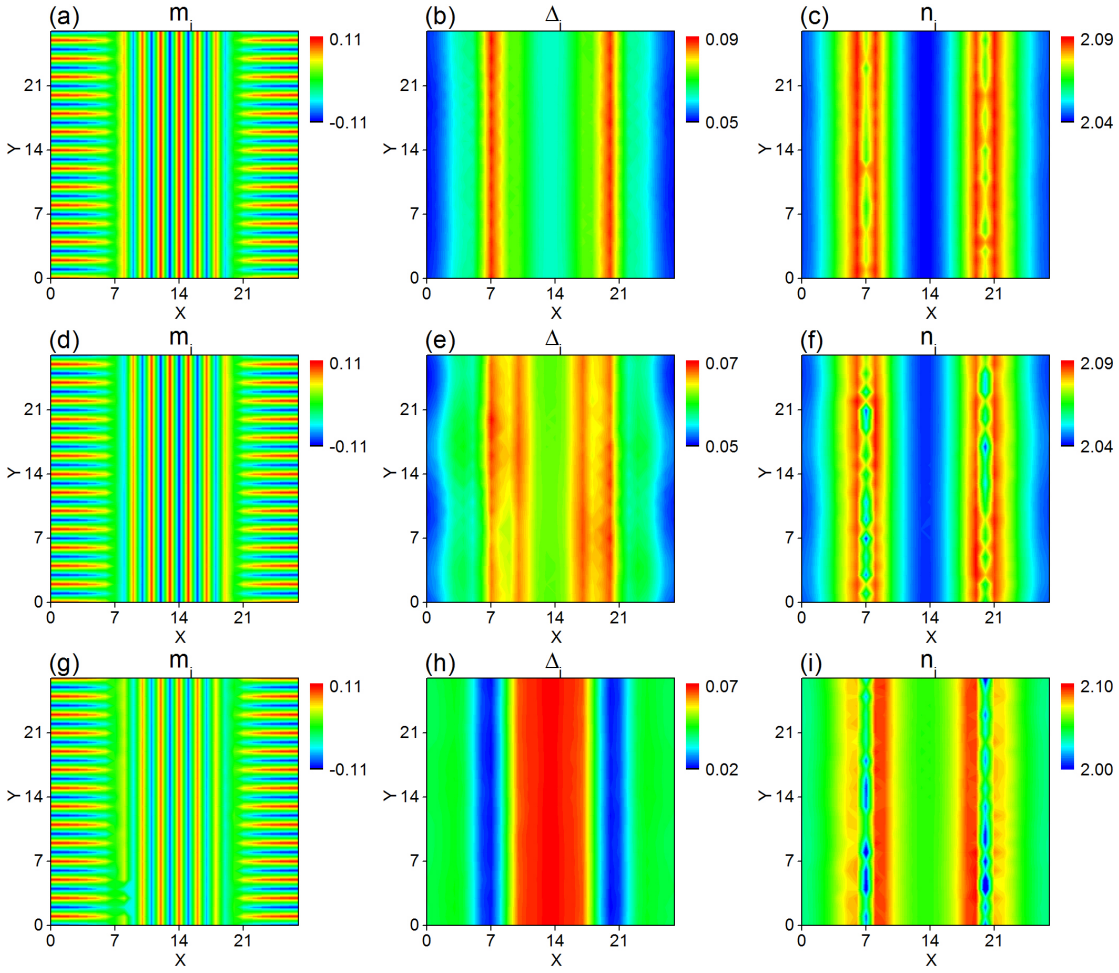

Figure 2.10: The spatial profiles of magnetic order, superconducting order and charge density for different mismatch scattering potential $V_s = w$, where w is randomly chosen from the range (-0.5, 0.5) ((a), (b), and (c)), range (-1.0, 1.0) ((d), (e), and (f)) and range (-2.0, 2.0) ((g), (h), and (i)).

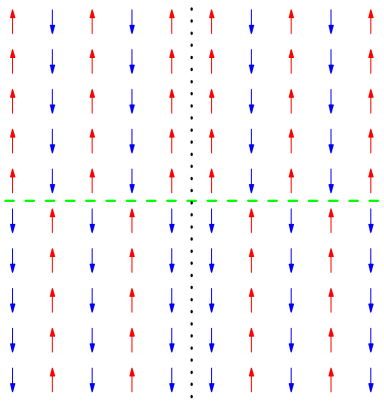

Figure 2.11: Two types of magnetic domain walls observed in [71]. The green-dashed line representing the antiphase DW while the black-dotted line representing the DW across which the nearest neighboring spins of the Fe atoms are ferromagnetically oriented. The arrow here indicating the direction of the spin or the magnetic moment of an Fe atom.

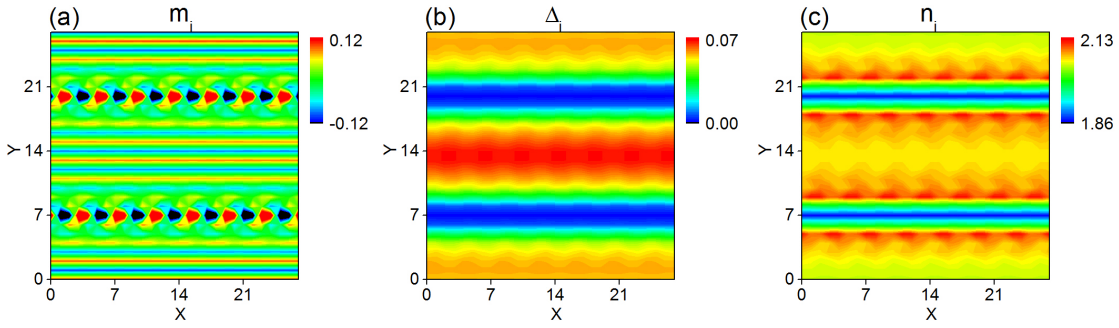

Figure 2.12: Spatial profiles of (a) the magnetic order, (b) the superconducting order, and (c) the charge density order are presented for a type-2 TB oriented along x-axis.

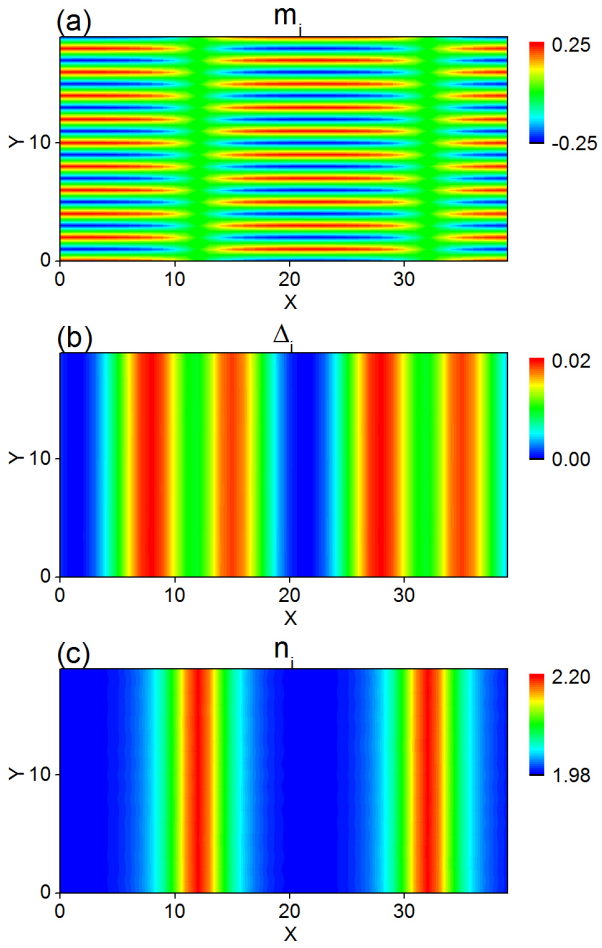

Figure 2.13: Spatial profiles of (a) the magnetic order, (b) the superconducting order, and (c) the charge density order in a 20×40 lattice.

Chapter 3

Transition of pairing symmetry from $s_{\pm}$-wave to d-wave in highly electron-doped $A_xFe_2Se_2$

3.1 Introduction

Recently, a new series of iron-based superconductors, $A_xFe_2Se_2$ (A=K, Cs), has been discovered with relatively high transition temperature of about 31 K [17–20]. These superconductors are the most heavily electron-doped among the iron-based superconductors, therefore it provides an opportunity to study the electronic structures and pairing mechanisms in iron-based superconductors in the highly electron-doped end. Band structure calculations [73–77] show that there are only electron pockets

existing near the M point of the Brillouin zone (BZ). Recent angle-resolved photoemission spectroscopy (ARPES) experiments [38–42] also showed the presence of electron pockets around the M point and the absence or near absence of a hole pocket around the Γ point. The $A_xFe_2Se_2$ can be considered similar to $Ba(Fe_{1-x}Co_xAs)_2$ with regard to the electron-pocket structure, however, the relatively strong superconductivity along with the absence of hole pocket would be a huge challenge for the $s_\pm$-wave pairing models of SC. Therefore a substituted pairing mechanism other than the interaction between electron and hole pockets in $A_xFe_2Se_2$ arises naturally at this place. Besides the strong SC phase in highly electron-doped end, it should also be capable of explaining the absence of the SC phase in the same doping level of the $Ba(Fe_{1-x}Co_xAs)_2$.

In this chapter, I will show that a d-wave symmetry pairing mechanism will switch on a robust SC phase in highly electron-doped region of the $A_xFe_2Se_2$ as the hole Fermi pockets are completely filled with doped electrons. I consider a real-space model with both NN and NNN pairings. This contrasts with a previous model [78, 79] that only includes NNN pairings into consideration for $Ba(Fe_{1-x}Co_xAs)_2$. According to the new pairing mechanism, the calculated phase diagram is qualitatively consistent with the experimental resutls [17–20]. There is a pairing symmetry type transition from $s_\pm$-wave to d-wave at about $x = 0.8$. Such symmetry transition has not been studied in any previous works. Our result also shows that the interplay between NN and NNN pairings leads to a competition between $s_\pm$-wave and d-wave states, while each state dominates in different doping levels. This competitive relationship has been observed in the recent Raman spectra experiment [80]. The evolution of

FS based on our model clearly demonstrates the process of the disappearance of the hole pockets in highly electron-doped region. The $s_{\pm}$-pairing symmetry is shown to persist from under- to over-doped regions, while the d-wave SC order emerges in $A_xFe_2Se_2$ at the same doping level where the hole pockets are completely occupied by doped electrons. As in the $Ba(Fe_{1-x}Co_xAs)_2$ scenario, the d-wave pairing is completely suppressed by weak impurity scatterings due to Co impurities in the highly doped samples. All these results are consistent with experiments [81–84], and previous $s_{\pm}$-wave pairing models [78, 85]. In order to test our prediction, the LDOS spectra near a strong impurity to distinguish $s_{\pm}$-wave and d-wave scenarios are calculated for highly doped $A_xFe_2Se_2$ superconductors. Our results demonstrate that there exist in-gap states for d-wave SC around the impurity while these states are absent for $s_{\pm}$ (or simply s)-wave SC. Hopefully the existence of d-wave pairing symmetry will be tested by future STM experiments.

3.2 Hamiltonian and methodology

In this chapter, Y. Tai's model, discussed in Sec. 1.3, is used to do the calculations of FS, LDOS, magnetic, and SC order parameters. The model has been successfully used to theoretically describe the magnetic, SC, and band structure properties of FeAs-122 family superconductors [79, 85, 86]. Based on the fact that $A_xFe_2Se_2$ shares the similar crystal and band structures with FeAs-122 family, it is reasonable that I apply our two-orbital model which is built for FeAs-122 family to do the calculation for $A_xFe_2Se_2$ compounds after an additional NN pairing is considered.

Consider the Hamiltonian $H = H_0 + H_{SC} + H_{int}$ that describes the energy of charge carriers. H_0 is the hopping terms and chemical potential, H_{SC} is the pairing interaction energy of the electrons, and H_{int} is the mean-field magnetic interaction energy. The specific forms of these three terms can be found in Eq. 1.2, 1.3, and 1.4. The eigenvalues and eigenfunctions of the total Hamiltonian H can be obtained by self-consistently solving the BdG equations shown in Eq. 1.19. Since an additional NN pairing is included in this chapter, the pairing order parameter $\Delta_{i\mu j\nu}$ is a little different with the one in Eq. 1.22

$$\Delta_{i\mu j\nu} = \Delta^{\mathrm{NN}}_{i\mu j\nu} + \Delta^{\mathrm{NNN}}_{i\mu j\nu}. \tag{3.1}$$

Here the NN and NNN components are calculated from the following equations

$$\Delta^{\mathrm{NN}}_{i\mu j\nu} = \frac{V_{\mathrm{NN}}}{4}\sum_n (u^n_{i\mu\uparrow}v^{n*}_{j\nu\downarrow} + u^n_{j\nu\uparrow}v^{n*}_{i\mu\downarrow}) \tanh\frac{E_n}{2k_BT}, \tag{3.2}$$

$$\Delta^{\mathrm{NNN}}_{i\mu j\nu} = \frac{V_{\mathrm{NNN}}}{4}\sum_n (u^n_{i\mu\uparrow}v^{n*}_{j\nu\downarrow} + u^n_{j\nu\uparrow}v^{n*}_{i\mu\downarrow}) \tanh\frac{E_n}{2k_BT}. \tag{3.3}$$

Throughout this work, the hopping terms are set as $t_{(1-6)} = (0.09, 0.08, 1.35, -0.12, -1, 0.25)$ and the onsite Coulomb interaction and Hunds coupling parameters are $U = 3.2$, $J_H = 0.6$ [79], while the chemical potential t_0 is determined by the electron filling per site n. V_{NN} is the intraorbital pairing interaction between NN sites, and V_{NNN} is the intraorbital pairing interaction between NNN sites. All energies are measured in unit of $|t_1|$. In the following calculations, the SDW order parameter is defined as $m_i = (-1)^{i_x}\frac{1}{4}\sum_\mu(\langle n_{i\mu\uparrow}\rangle - \langle n_{i\mu\downarrow}\rangle)$, and the pairing order parameters of NN d-wave, NN s-wave, NNN d-wave and NNN $s_\pm$-wave are defined as $\Delta_d = \frac{1}{8N}\left|\sum_{ij\mu\nu}\epsilon_x\epsilon_y\Delta_{i\mu j\nu}\right|$, $\Delta_s = \frac{1}{8N}\sum_{ij\mu\nu}\Delta_{i\mu j\nu}$, $\Delta'_d = \frac{1}{8N}\left|\sum_{ij'\mu\nu}\epsilon_x\epsilon_y\Delta_{i\mu j'\nu}\right|$, $\Delta'_{s_\pm} = \frac{1}{8N}\sum_{ij'\mu\nu}\Delta_{i\mu j'\nu}$ correspondingly, where $\mathbf{j} = \mathbf{i} \pm \hat{x}(\hat{y})$ which indicates the NN

sites of site $\mathbf{i}$, $\mathbf{j}' = \mathbf{i} \pm \hat{x} \pm \hat{y}$ which indicates the NNN sites of site $\mathbf{i}$, $\epsilon_{x(y)} = (\mathbf{j}^{(\prime)} - \mathbf{i}) \cdot \hat{x}(\hat{y})$ and N is the number of Fe lattice sites. The LDOS proportional to the differential tunneling conductance as measured by STM experiment can be calculated according to Eq. 1.27, where the delta function $\delta(x)$ is taken as $\Gamma/\pi(x^2 + \Gamma^2)$, with $\Gamma = 0.002$. All the numerical calculations are performed on 28×28 lattice with periodical boundary conditions. A 64×64 supercell is taken to calculate the LDOS.

Based on the steps listed in Sec. 1.6, the system can be numerically solved. It should be noticed that the pairing orders are non zero for both NN sites and NNN sites. The SC order parameters from different types of pairing symmetries are calculated separately based on the definitions listed in the previous paragraph.

3.3 Phase diagram and Fermi surface with nearest neighbor pairings

In two previous works [78, 85], it has been shown that the $s_{\pm}$-wave superconductivity in the phase diagram for $Ba(Fe_{1-x}Co_xAs)_2$ is due to the NNN intraorbital pairing interaction. The approach in these works [78, 85] gives a unified description of the entire phase diagram covering both the electron- and hole-doped regimes, and the k-sapce $s_{\pm}$-wave SC order parameter $\Delta_{s_{\pm}}(k) = 2\Delta'_{s_{\pm}}[\cos(k_x) + \cos(k_y)]$ vanishes in highly doped regime ($n \geq 2.4$) where the hole pocket on the FS at the Γ point is shrinking to zero. On the other hand, it is known that the SC has been observed in recently discovered $A_xFe_2Se_2$ at higher doping level than $n = 2.4$ [17–20] with an

unsettled pairing symmetry. A new pairing interaction in addition to that of our previous work should be taken into consideration.

In order to seek a unified theme for the pairing symmetry in the electron doped $A_xFe_2Se_2$ and other FeAs-122 compounds, it is natural to include the NN intraorbital pairing interaction in our study. The phase diagram thus obtained is shown in Fig. 3.1. The coexistence of SC order parameters from different pairing symmetry are labeled in the figure, together with 2×1 collinear SDW order. In order to study how the new NN pairings affect the SC phase in different doping levels, in the calculation the NNN pairing is set to be constant $V_{\mathrm{NNN}} = 1.05$, but the NN pairing is changing from $V_{\mathrm{NN}} = 1.1$ to 1.3. When $V_{NN} = 1.1$ as shown in Fig. 3.1(a), from $n = 2.0$ to $n = 2.4$, the pairing symmetry is dominantly $s_{\pm}$-wave-like, while in the doping region $2.4 < n < 2.5$, the SC has a d-wave-like symmetry originating in the NN pairing interaction. When the NN pairing is increased to 1.2 as shown in Fig. 3.1(b), the d-wave-dominant region expands to $2.38 < n < 2.5$, meanwhile the d-wave SC order is also enhanced in the highly electron-doped region ($2.4 < n < 2.5$). The SC and AFM orders remain unchanged in all the other doping levels. When the NN pairing is further increased to 1.3 as shown in Fig. 3.1(c), the d-wave SC order is again enhanced in the highly electron-doped region, there is no expansion for d-wave-dominant region, and all the other doping levels remain the same as the previous two diagrams. If the NN pairing is larger than 1.3, the d-wave pairing order will emerge even at under- and optimal-doped regions, and the $s_{\pm}$-wave order will no longer dominate in those doping levels.

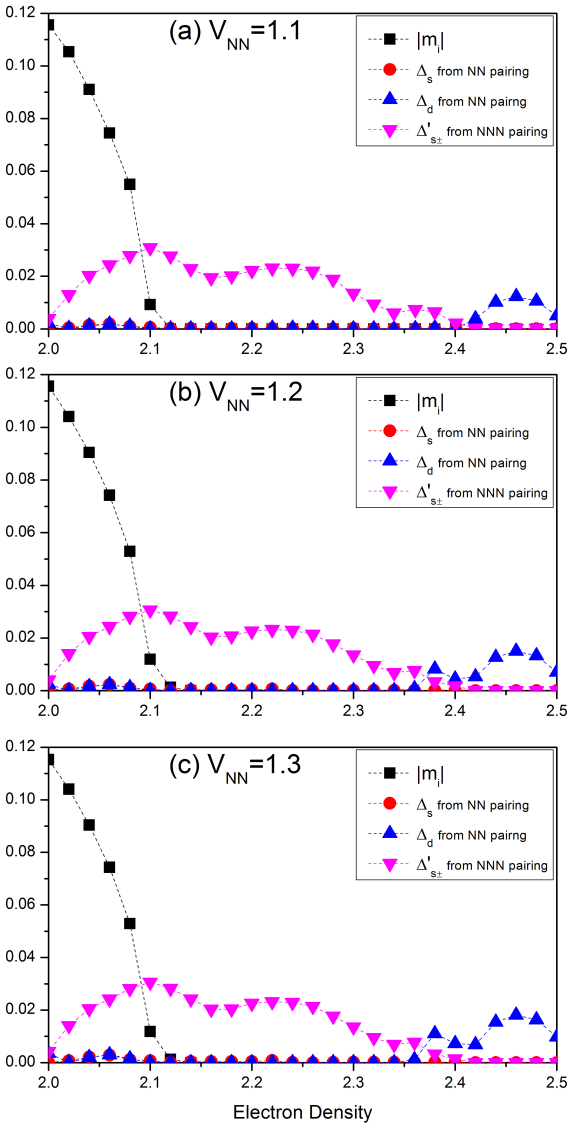

Figure 3.1: SC and AFM phase diagram at $T = 0K$ for electron-doped $A_xFe_2Se_2$ and from under- to over-doped $Ba(Fe_{1-x}Co_xAs)_2$ by a single model with NN pairing V_{NN} to be (a) 1.1, (b)1.2 and (c)1.3. Black squares, red circles, blue, and pink triangles represent the collinear SDW order parameter, pairing order parameter of NN s-wave, NN d-wave and NNN $s_{\pm}$-wave correspondingly. The NNN d-wave order is not shown since it is zero in all doping levels. The NNN pairing is set to be constant $V_{\mathrm{NNN}} = 1.05$.

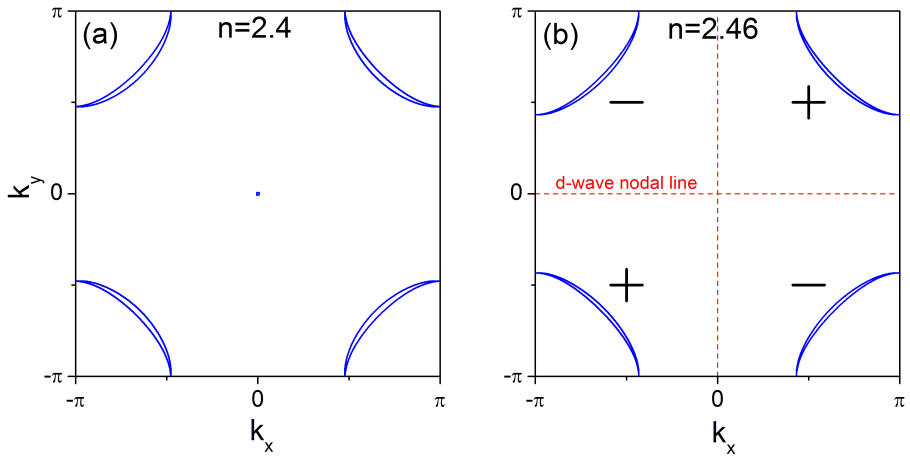

Figure 3.2: Fermi surface at doping level $n =$ (a) 2.4 and (b) 2.46 in the first Brillouin zone of a two-Fe unit cell. Blue (solid) lines represent the Fermi surface, and the red (dashed) lines represent the nodal lines of d-wave SC order parameter which are not crossing the Fermi surface. The plus and minus sign indicates the sign of pairing order parameter in each region. The NN and NNN pairing are set to be $V_{\mathrm{NN}} = 1.1$ and $V_{\mathrm{NNN}} = 1.05$.

In addition to the pairing order parameter, the FS structure may also be responsible for the systems pairing symmetry. The zero-temperature FS is defined by zero-energy contours of the quasiparticles, which can be drawn by using the Fourier transformation of the minimal hopping Hamiltonian. In highly electron-doped samples, the SDW order is completely suppressed and thus I show the corresponding FSs in the BZ of two-Fe atoms per unit cell. In the following calculation I choose $V_{\mathrm{NN}} = 1.1$ and $V_{\mathrm{NNN}} = 1.05$, the same parameter as shown in the phase diagram Fig. 3.1(a). Fig. 3.2(a) shows the FS at $n = 2.4$, where the $s_{\pm}$-wave SC is suppressed to zero and the hole pocket on the FS shrinks to a point at the center of the BZ by doped electrons. Our calculation shows there is no hole-pocket structure for all

doping levels higher than $n = 2.42$, which is consistent with the ARPES experimental observations [38–42]. Fig. 3.2(b) shows the FS at $n = 2.46$, where k-space d-wave pairing order parameter $\Delta_d(k) = 2\Delta_d \sin(k_x)\sin(k_y)$ is maximized. The red-dashed lines here denote the nodes (or zeros) of $\Delta_d(k)$ and they do not cross the FS. In other words, $\Delta_d(k)$ is positive on the FS near (π, π) and $(-\pi, -\pi)$, and negative near $(-\pi, \pi)$ and $(\pi, -\pi)$. The sign change over neighboring electron pockets demonstrates that the SC phase from $n = 2.4$ to 2.5 shown in Fig. 3.1(a) is of d-wave symmetry without nodes. Our FS calculation result is in good agreement with a random phase approximation (RPA) calculation [87]. It should be noticed that the symmetry type transition from $s_{\pm}$-wave to d-wave occurs at the same doping level where the hole pocket disappears on the FS, which reveals the intrinsic correlation between FS structure and system's pairing symmetry.

3.4 Phase diagram with weak impurity effect

In contrast to the robust SC phase, particularly at highly electron-doped $A_xFe_2Se_2$ compounds, I have to address the outstanding question as to why the SC has not been observed in $Ba(Fe_{1-x}Co_xAs)_2$ for $n > 2.4$ where the SC has a d-wave symmetry according to the calculation in a previous part of this dissertation. In this type of compound, Fe atoms in the Fe-As layer are replaced by doped Co atoms. It is commonly believed that the difference between a Co atom and the replaced Fe atom is no more than just a doped electron. However due to slightly different electronegativity of both atoms, or different interaction energy with electrons, it is more accurate to

consider the Co atoms as impurities in the Fe-plane. In this part, I treat Co atoms in the Fe-plane as a weak and random scattering-centers, which should suppress the SC of d-wave symmetry in the highly electron-doped end. On the contrary, the Fe-planes in $A_xFe_2Se_2$ are quite clean, and the doped inpurities are off the Fe-planes. The scattering potentials due to A-atoms are rather weak for conduction electrons and the the SC with d-wave symmetry could hardly suppressed. To consider the scattering effect of the Co impurities in $Ba(Fe_{1-x}Co_xAs)_2$, the Hamiltonian due to the impurity part can be written as $H_{imp} = \sum_{i\mu\sigma} V_i c^{\dagger}_{i\mu\sigma} c_{i\mu\sigma}$, where V_i is the impurity intensity at the i-th Co site in the lattice, the summation is over all randomly distributed impurity atoms. In this work, the impurity of potential of Co is known to be weaker than those of Ni and Cu [88], and I set it to be $V_i = -1$.

Our numerical result for the phase diagram of $Ba(Fe_{1-x}Co_xAs)_2$ is shown in Fig. 3.3 as a function of electron density, which is also propotional to concentration of Co impurities. I choose the NN and NNN pairing to be $V_{\rm NN} = 1.1$ and $V_{\rm NNN} = 1.05$, the same parameter as shown in the phase diagram Fig. 3.1(a). Each point of the phase diagram in Fig. 3.3 is numerically averaged over 10 different randomly distributed impurity configurations on a 28×28 lattice. Since the error bar of each point is smaller than the point itself, they are not shown on the graph. As seen, in the under-doped and optimal-doped region ($n = 2.0 \sim 2.34$), the SC order is partial suppressed under the influence of impurity effects as compared with the results without impurities as shown in Fig. 3.1(a), although the SC with $s_{\pm}$-symmetry still exists in these regions. But the SC is completely suppressed in the over-doped region ($n > 2.34$). And this is the reason why the SC with d-wave symmetry never

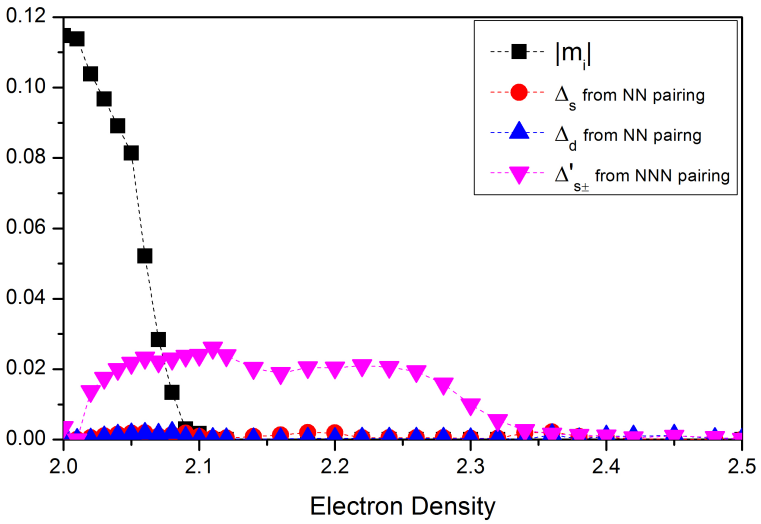

Figure 3.3: SC and AFM phase diagram at $T = 0$ K of $Ba(Fe_{1-x}Co_xAs)_2$ after the weak impurity effect is considered in addition to the doping effect. Black squares, red circles, blue and pink triangles represent the collinear SDW order parameter, pairing order parameter of NN s-wave, NN d-wave and NNN $s_{\pm}$-wave correspondingly. The impurity intensity is set to be $V_i = -1$, the NN and NNN pairing are set to be $V_{\mathrm{NN}} = 1.1$ and $V_{\mathrm{NNN}} = 1.05$.

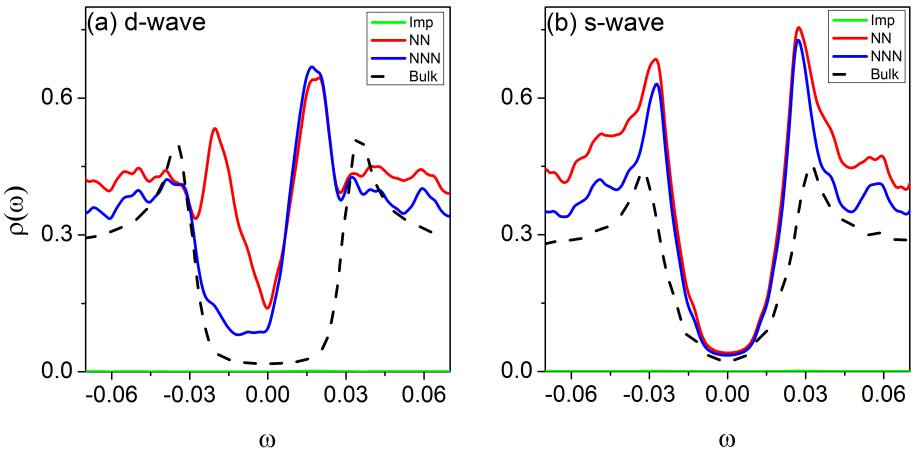

Figure 3.4: LDOS spectra for $n = 2.46$ near single strong nonmagnetic impurity for (a) d-wave pairing symmetry state and (b) $s_{\pm}$-wave pairing symmetry state. Green, red, and blue (solid) lines are results of LDOS at impurity site, NN site and NNN site respectively. Black (dashed) lines are bulk results without impurity effect. The impurity intensity is set to be $V = -100$ in both cases, the NN and NNN pairing are set to be $V_{\rm NN} = 1.1$ and $V_{\rm NNN} = 1.05$.

shows up in the $Ba(Fe_{1-x}Co_xAs)_2$ compound.

3.5 Single impurity in s-wave and d-wave pairing symmetry

In order to examine how the SC with d-wave pairing symmetry predicted for highly electron-doped $A_xFe_2Se_2$ could be tested by future experiments, I calculate the LDOS spectra near a single strong nonmagnetic impurity for SC respectively with d-wave and $s_{\pm}$-wave symmetry. For d-pairing symmetry, the SC order parameter has sign changes on neighboring electron Fermi pockets (see Fig. 3.2). I thus expect that

near the impurity, a quasiparticle could be scattered from a FS with positive SC order parameter to the FS with negative order parameter. This mechanism leads to the formation of Andreev bound states which can manifest themselves as the in-gap peaks in LDOS spectra near the impurity. For SC with $s_{\pm}$(or s)-pairing symmetry, the SC order parameter has no sign change across the electron Fermi pockets, and there should be no in-gap states or peaks in the LDOS. Calculated results for the LDOS near a strong impurity with $V = -100$ are shown in Fig. 3.4, the NN and NNN pairings are set to be $V_{\mathrm{NN}} = 1.1$ and $V_{\mathrm{NNN}} = 1.05$. Fig. 3.4(a) and (b) are for SC respectively with the d-wave and $s_{\pm}$-wave pairing symmetry. It is expected to see from Fig. 3.4(a) that there are two in-gap resonance peaks at the NN site. On the NNN site, the peak at negative energy disappears, only one positive-energy peak remains. At the impurity site the LDOS is suppressed to zero by the strong impurity. For SC with $s_{\pm}$-pairing symmetry, there is no in-gap resonance peaks formed at neither NN nor NNN site. Although the above results are obtained for a strong impurity, but the predictions should remain the same if the impurity potential becomes positive and its magnitude decrease to moderate strength. Similar signature property has also been proposed in a theoretical work [89]. Hopefully the signature of the d-wave pairing symmetry will be measured by future STM experiments.

3.6 Conclusions

In this chapter, by including both of the NN and the NNN intraorbital pairing interactions, I showed that the pairing symmetry of the SC changes from $s_{\pm}$-wave to

d-wave like in highly electron-doped $A_xFe_2Se_2$. The transition occurs when the hole pockets near the Γ point in the FS are just completely filled up by doped electrons. The absence of SC phase with d-wave symmetry in highly doped $Ba(Fe_{1-x}Co_xAs)_2$ can be attributed to the presence of the weak scattering effect due to the randomly distributed Co impurities in this compound. In order to test the existence of the d-wave SC in highly electron-doped $A_xFe_2Se_2$, I suggest to look for the signature of the in-gap states by STM experiments.

Chapter 4

Strong impurity in the vortex core of hole-doped Fe-pnictide

4.1 Introduction

Most high temperature superconductors, including Fe-pnictide, are of type II, which means that magnetic fields can penetrate into the SC state in the form of a vortex core structure, and that the SC order is destroyed at the center of the vortex cores. Investigating the vortex states in Fe-pnictides can provide useful information on the interplay between the SDW and SC, as well as the pairing symmetry. Recent STM experiments [90–92] reported fruitful results about the vortex structure and vortex core states in Fe-pnictides. For example, the results of hole-doped $Ba_{2-x}K_xFe_2As_2$ revealed that a single conductance peak appears at a negative-biased voltage at the vortex center [93, 94]. In contrast, this negative-biased peak has not been observed

in electron-doped $Ba(Fe_{1-x}Co_x)_2As_2$ [90].

Several experimental and theoretical results suggested that Fe-pnictides have an $s_{\pm}$-wave pairing symmetry, the so called extended s-wave pairing with opposite signs of the order parameters between the hole pockets and the electron pockets. In general, the effect of non-magnetic impurities is promising in addressing the pairing symmetry [95–98]. Moreover, impurities have also been used to account for the absence of the bound states in the vortex core for the electron-doped $Ba(Fe_{1-x}Co_x)_2As_2$ [99]. The interplay between the impurity and vortex is of great interest and has been studied in cuprates. However, this topic has not been studied in hole-doped Fe-pnictides.

Therefore in this chapter, I will investigate the key role of the strong impurity at the vortex core as a pinning center. Prior to the impurity effect, the vortex core state without impurities is calculated in both optimal-doped and under-doped cases. Resonance peak splitting is observed in the optimal-doped case while superlattice modulation emerges in the under-doped case. Then the impurity effect inside and far away the vortex core is investigated. Impurities with both positive and negative scattering potentials are considered. Due to the competitive relationship between AFM order and the resonance peak near Fermi energy induced by vortex core state, the peak will emerge at under-doped case when AFM order is suppressed by strong impurity effect. The results are robust under either positive or negative impurity scattering potential. Consequently, the impurity resonance peak may be used to identify the nature of vortex core state of hole-doped Fe-pnictide superconductors.

4.2 Model and Landau gauge

In this chapter, Y. Tai's model discussed in Sec. 1.3 is used to do the calculations. This model has been proved to work well in both electron- and hole-doped regimes for FeAs-122 family, therefore it is reasonable for me to use it here. The effective mean-field Hamiltonian can be written as $H = H_0 + H_{SC} + H_{int}$. H_{SC} is the pairing interaction energy of the electrons, and H_{int} is the mean-field magnetic interaction energy. The specific forms of these two terms can be found in Eq. 1.3 and 1.4. H_0 is is the hopping terms and chemical potential, the hopping terms are different with the ones shown in Eq. 1.2 under the effect of magnetic field

$$H_0 = -\sum_{i\mu j\nu\sigma} (t_{i\mu j\nu} e^{i\varphi_{ij}} c^\dagger_{i\mu\sigma} c_{j\nu\sigma} + \text{H.c.}) - t_0 \sum_{i\mu\sigma} c^\dagger_{i\mu\sigma} c_{i\mu\sigma}. \tag{4.1}$$

The phase factor $e^{i\varphi_{ij}}$ in the hopping terms comes from the the presence of a magnetic field B perpendicular to the plane, where

$$\varphi_{ij} = \frac{\pi}{\Phi_0} \int_{r_i}^{r_j} \mathbf{A}(\mathbf{r}) \cdot d\mathbf{r} \tag{4.2}$$

is the Peierl's phase factor. The superconducting flux quantum

$$\Phi_0 = \frac{hc}{2e} = 2.07 \times 10^{-15} \text{Tm}^2, \tag{4.3}$$

here is a constant. Within the Landau gauge, the vector potential can be written as

$$\mathbf{A}(\mathbf{r}) = (-By, 0, 0), \tag{4.4}$$

where y is the y-component of the position vector $\mathbf{r}$. Under the Landau gauge, two superconducting vortices form one magnetic unit cell. Each vortex carries a total flux of Φ_0 and is located at the center of a square area containing $N \times N$ lattice sites,

where N is a positive integer. Therefore the minimum lattice size to calculate one complete magnetic unit cell would be $2N \times N$. Once the lattice size N is chosen, then the magnetic field on the lattice can be decided by

$$B = \frac{\Phi_0}{N_x N_y}, \tag{4.5}$$

where $N_x = 2N$ and $N_y = N$. Then the eigenvalues and eigenfunctions of the total Hamiltonian H can be obtained by self-consistently solving the BdG equations shown in Eq. 1.19. The s±-wave SC order parameter at position i is defined as $\Delta_i = \frac{1}{4}\left[\Delta_{i,i+\hat{x}+\hat{y}} + \Delta_{i,i-\hat{x}-\hat{y}} + \Delta_{i,i+\hat{x}-\hat{y}} + \Delta_{i,i-\hat{x}+\hat{y}}\right] e^{i\varphi_{ij}}$, the collinear SDW order parameter is defined as $m_i = (-1)^{i_x}\frac{1}{4}\sum_\mu(\langle n_{i\mu\uparrow}\rangle - \langle n_{i\mu\downarrow}\rangle)$.

Throughout this work, the hopping terms are set as $t_{(1-6)} = (-1, 0.08, 1.35, -0.12, 0.09, 0.25)$ as shown in [55], and the onsite Coulomb interaction, Hunds coupling parameter, and SC-pairing strength are $U = 3.5$, $J_H = 0.4$, and $V_{i\mu j\nu} = 1.3$, while the chemical potential t_0 is determined by the electron filling per site n. All energies are measured in unit of $|t_1|$. The LDOS proportional to the differential tunneling conductance as measured by STM experiment can be calculated according to Eq. 1.27, where the delta function $\delta(x)$ is taken as $\Gamma/\pi(x^2 + \Gamma^2)$, with $\Gamma = 0.005$. All the numerical calculations are performed on 48×24 lattice with periodical boundary conditions. A 24×24 supercell is taken to calculate the LDOS.

The numerical steps discussed in Sec. 1.6 can be used here to solve the system. One major difference for the Hamiltonian in this chapter with the previous ones is that there is an extra phase change caused by magnetic field in the hopping terms. The phase factor can be decided by Eq. 4.6, 4.8, and 4.9. These factors should be

set up very carefully. One easy way to test the correctness of these phase factors is to calculate the phase change after a loop around one lattice square. Specifically, by setting all the hopping constants $t_{(1-6)}$ to be 1, multiply the H matrix elements around one lattice square $H_{i\mu(i+\hat{x})\mu\sigma} \times H_{(i+\hat{x})\mu(i+\hat{x}+\hat{y})\mu\sigma} \times H_{(i+\hat{x}+\hat{y})\mu(i+\hat{y})\mu\sigma} \times H_{(i+\hat{y})\mu i\mu\sigma}$ and check if this value stays constant with different lattice site i. If this value is not a constant over all lattice squares, then there is something wrong in the phase factors.

4.3 Vortex core state without impurity

Before studying the impurity effect, a homogeneous system in a magnetic field is calculated. The results at doping level $n = 1.80$ are shown in Fig. 4.1. In this region, a collinear AFM-SDW is slightly induced. The AFM-SDW reaches its maximum at the vortex center and decays at the scale of ξ to zero into the superconducting region. The superconductivity is vanished at the vortex center and starts to increase at the scale of the coherence length ξ to its bulk value. On the other hand, the charge density is strongly enhanced at the vortex center. Fig. 4.1(d) shows the LDOS at different positions from the vortex center along the x-axis. At the vortex center, the Andreev bound states corresponding to a negative-energy in-gap peak located at $\omega = -0.03$. When moves away from the center, not only the height of the peak decreases, but also it gradually splits into two. The width of the two-peak increases as moving further away from the vortex center. Finally, the LDOS evolves continuously into its bulk features. It should be noticed that besides the peak which splits into two, there is another peak located in the positive side of the Fermi energy. This peak

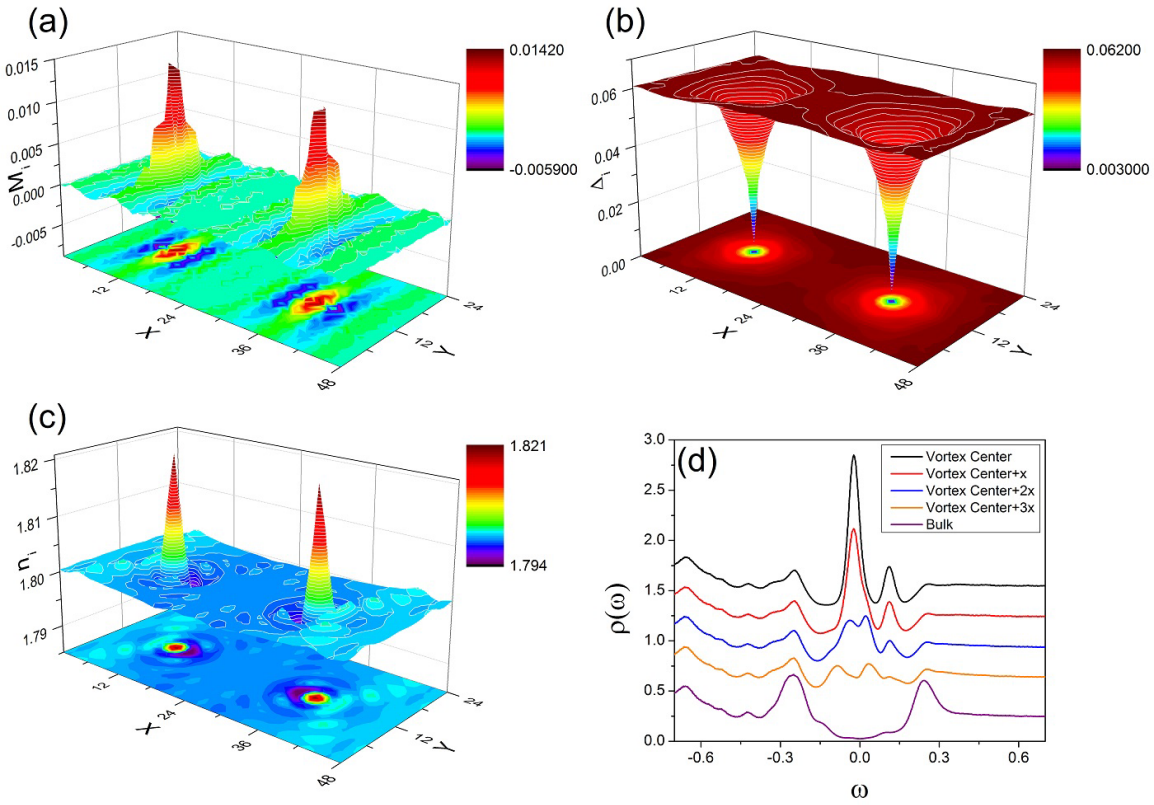

Figure 4.1: Spatial variation of (a) magnetic order parameter M_i, (b) SC order parameter Δ_i and (c) electron density n_i are plotted on a 48×24 lattice. (d) The LDOS spectra at five typical positions along the x-axis from the vortex center towards positive x direction. The curves are displaced vertically with offsets for clarity. The doping level is $n = 1.8$.

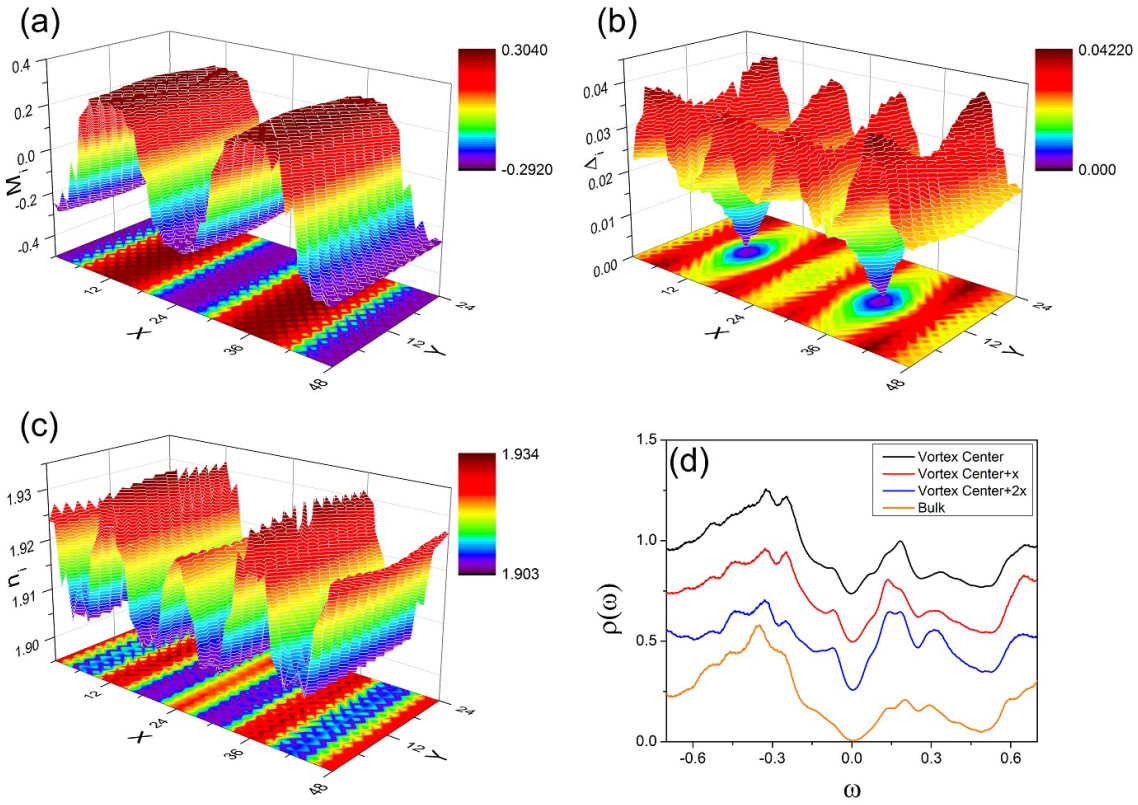

Figure 4.2: Spatial variation of (a) magnetic order parameter M_i, (b) SC order parameter Δ_i and (c) electron density n_i are plotted on a 48×24 lattice. (d) The LDOS spectra at four typical positions along the x-axis from the vortex center towards positive x direction. The curves are displaced vertically with offsets for clarity. The doping level is $n = 1.92$.

will not split but only decreases its height until fully disappears. These features agree with the STM experimental results [92].

Fig. 4.2(a)-(c) show the spatial variation of the staggered magnetization M_i, $s_{\pm}$-wave superconductivity (Δ_i) and the charge density (n_i) respectively at $n = 1.92$. The results in this doping region shows a remarkable phenomenon. Additional to the emergence of the CAF-SDW in the entire lattice, an extra pattern with period

$24a_0$ modulates the existence SDW and forms a stripe-like structure. Besides the SDW, the Δ_i and n_i also show a stripe pattern with period $24a_0$. The origin of such superlattice modulation is understandable in terms of the nesting vector $Q \sim \frac{2\pi}{24a_0}$ connecting the hole and electron pockets around Γ and M points along the x-axis in the magnetic Brillouin zone. In addition, due to the appearance of the superlattice modulation, the vortex core size has been enlarged and has also been stretched along the y-axis as shown in Fig. 4.2(b). The increased size of the vortex core will induce a larger area of AFM, thus leads to the suppressing of the superconductivity near the core. The stripe feature can also be identified in the LDOS as a peak closed to the coherence peak, the dotted arrow shown in Fig. 4.2(d). Besides of the stripe feature peak, a weak single in-gap peak appears at the negative side to the Fermi energy. Unlike the optimal-doped case, these is no strong in-gap peak formed close to the Fermi energy here, which means the existence of AFM order suppresses the formation of that peak.

4.4 Vortex core state with strong impurity effect

4.4.1 Impurity with positive scattering potential

In addition to the magnetic field-induced vortex core state that I studied in the previous section, impurity effects pinning inside and away from the vortex core center have been taken into consideration. In the following calculations, two impurities with positive scattering potential are located at the vortex core center in the left-hand

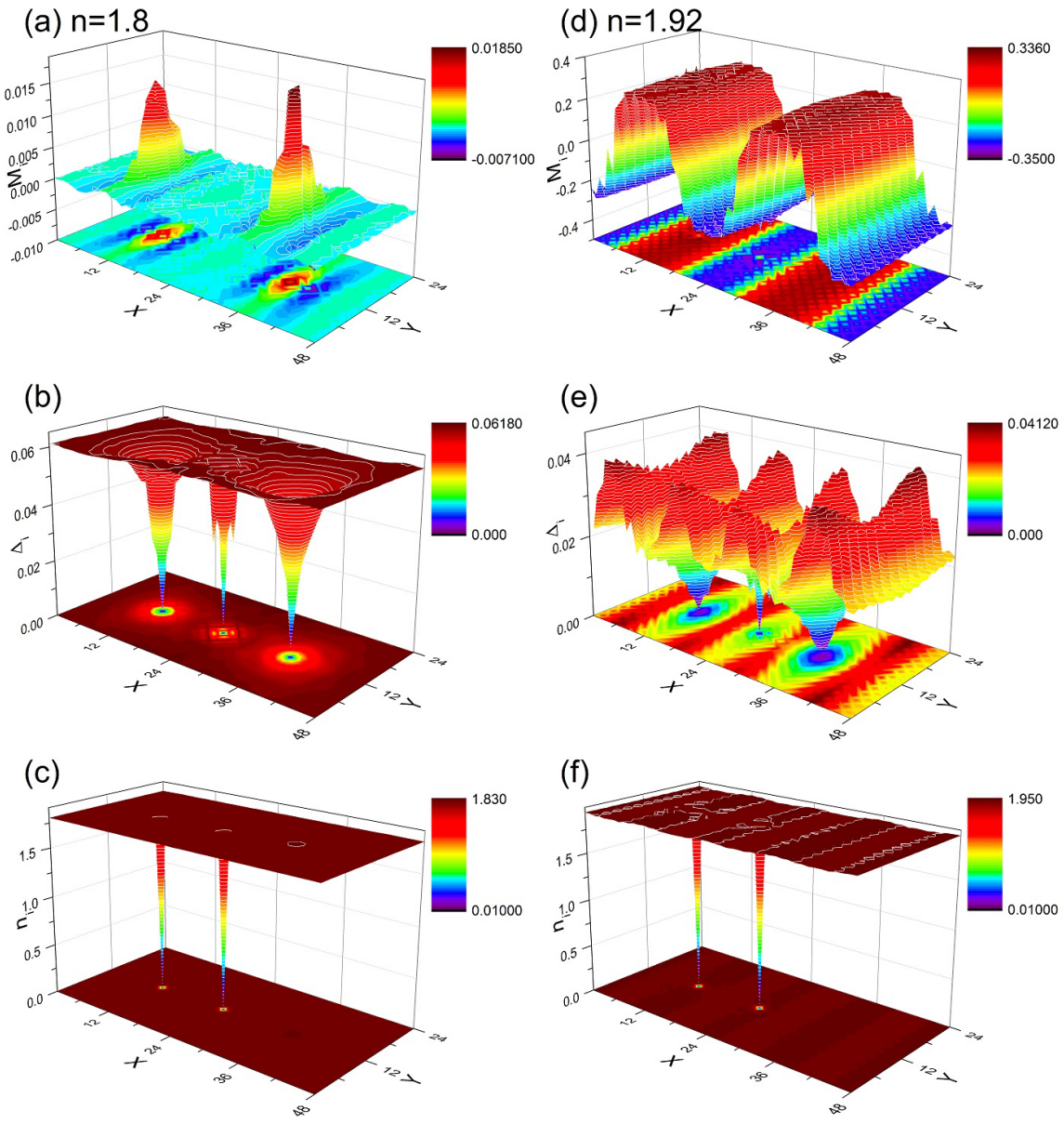

Figure 4.3: Spatial variation of (a) magnetic order parameter M_i, (b) SC order parameter Δ_i and (c) electron density n_i with doping level $n = 1.8$, (d) magnetic order parameter M_i, (e) SC order parameter Δ_i, and (f) electron density n_i with doping level $n = 1.92$ are plotted on a 48×24 lattice. Two impurities with scattering potential $V = +20$ are placed at the center of vortex core $(12, 12)$ and far away from the vortex core $(24, 12)$.

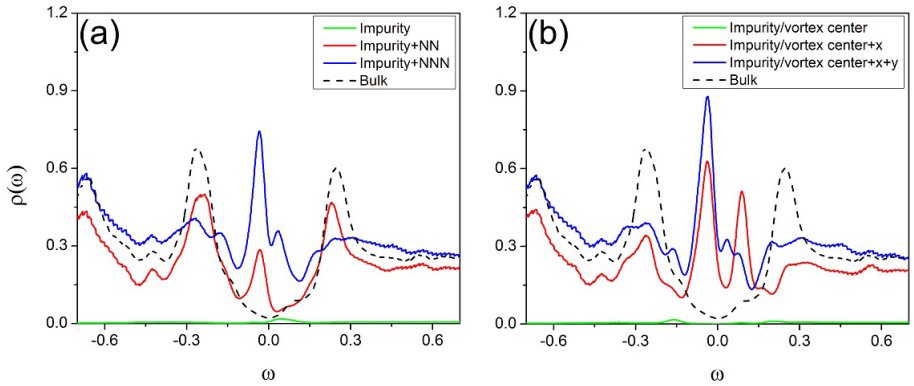

Figure 4.4: The LDOS spectra at four typical positions near the impurity (a) away from the vortex center $(24, 12)$ and (b) at the center of the vortex core $(24, 12)$. The scattering potential of the impurity is $V = +20$, and the doping level is $n = 1.8$.

side $(12, 12)$ and in between two vortex cores $(24, 12)$. These two impurities would help us to learn the impurity effects both under and not under the impact of vortex core state. In Fig. 4.3 the AFM, SC and electron density order with two impurities of intensity $V = +20$ are presented. For the strong repulsive impurity, electrons at the impurity site are repelled and the electron density is suppressed. As shown in Fig. 4.3(a) and (d), the CAF-SDW is slightly induced around the vortex core. On top of the field-induced CAF-SDW around the vortex, the strong impurity induces the local SDW nearby the impurity. Due to the impurity effect, the total induced SDW is stronger in the pinned vortex. When the superlattice modulation is induced, the impurity is no more as a pinning center, instead, the vortex core is pinned at the ridge of the stripelike-SDW, where the field-induced SDW is stronger than the one induced by an strong impurity.

The LDOS spectra near the impurities are shown in Fig. 4.4 ($n = 1.8$, the optimal-doped case) and 4.5($n = 1.92$, the under-doped case). Fig. 4.4(a) shows

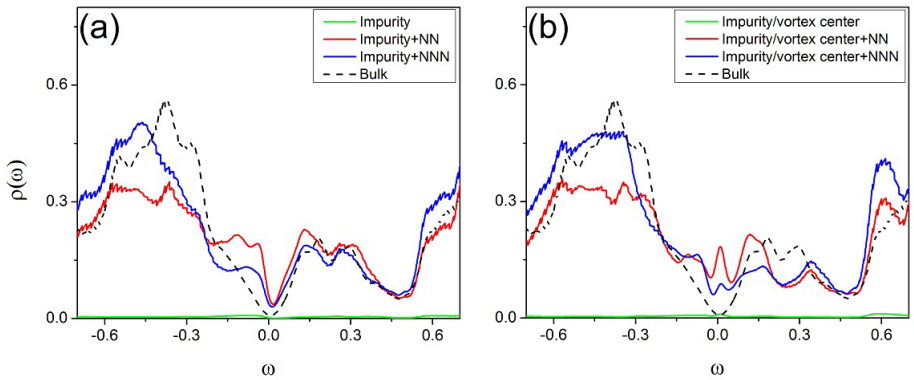

Figure 4.5: The LDOS spectra at four typical positions near the impurity (a) away from the vortex center $(24, 12)$ and (b) at the center of the vortex core $(24, 12)$. The scattering potential of the impurity is $V = +20$, and the doping level is $n = 1.92$.

the LDOS near the impurity away from the vortex core. Due to the strong impurity intensity, the LDOS on the impurity site is very close to zero. At the NN site, one in-gap peak located at the negative side of the Fermi energy appears. At the NNN site, the peak at negative side gets much higher and at the mean time another peak at positive side of the Fermi energy emerges. This result is consistent with another theoretical calculation [100]. Fig. 4.4(b) shows the LDOS results near the impurity inside the vortex core. As shown in the figure, the spectra on NNN site does not change much compared to the one away from vortex core. However on the NN site, besides the negative side peak we see in Fig. 4.4(a), another peak at the positive side of the Fermi energy emerges. This peak is not located at the same energy level as the NNN site, but very close to the position where we mentioned in Fig. 4.1(d), which means the peak is from the vortex core state, not the impurity effect.

Fig. 4.5 shows the LDOS near the impurity at under-doped case ($n = 1.92$). In Fig. 4.5(a), where the impurity is placed away from the vortex core, the LDOS on

the impurity site is very close to zero similar to the optimal doped case. There are two in-gap peak formed, one at the negative side and the other at the positive side of the Fermi energy. Again the results are very similar to those calculated in [100]. As in Fig. 4.5(b), the LDOS near the impurity inside the vortex core is calculated. Although the two in-gap peaks still remain at opposite side of the Fermi energy, there is another single peak formed very close to the Fermi energy. By considering the difference between Fig. 4.5(a) and (b), it is reasonable to correlate this new peak with the vortex core state. In fact according to the results in the previous section, vortex core state will form a robust peak very close to the Fermi energy near the vortex core center, as shown in Fig. 4.1(d). But the existence of strong AFM order will suppress the peak near Fermi energy, as shown in Fig. 4.2(d). According to Fig. 4.3(d), the strong impurity effect will suppress the local AFM order, and the vortex core state peak is no longer suppressed locally. Therefore this peak shows up again here.

4.4.2 Impurity with negative scattering potential

In order to check the robustness of our main results above, a negative scattering potential is used to do a similar calculation. In Fig. 4.6 the AFM, SC and electron density order with two impurities of intensity $V = -20$ are presented. For the strong attractive impurity, electrons at the impurity site are attracted and the electron density is enhanced. Therefore the electron density at impurity site is maximized to $n = 4$. Except for the differences in electron density map, the other two orders, AFM and SC orders, are very similar to the results shown in Fig. 4.3 where the positive

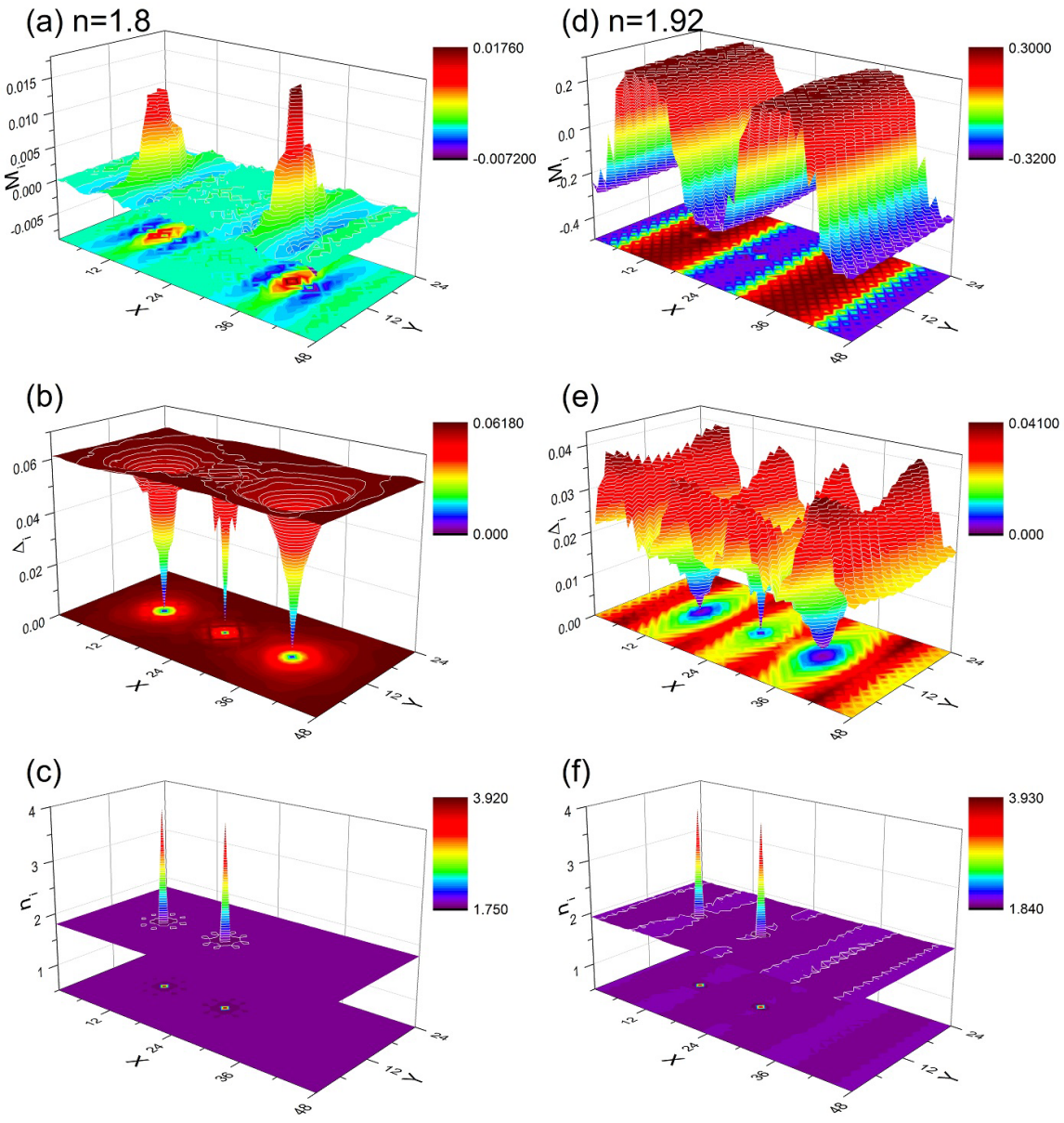

Figure 4.6: Spatial variation of (a) magnetic order parameter M_i, (b) SC order parameter Δ_i and (c) electron density n_i with doping level $n = 1.8$, (d) magnetic order parameter M_i, (e) SC order parameter Δ_i and (f) electron density n_i with doping level $n = 1.92$ are plotted on a 48×24 lattice. Two impurities with scattering potential $V = -20$ are placed at the center of vortex core $(12, 12)$ and far away from the vortex core $(24, 12)$.

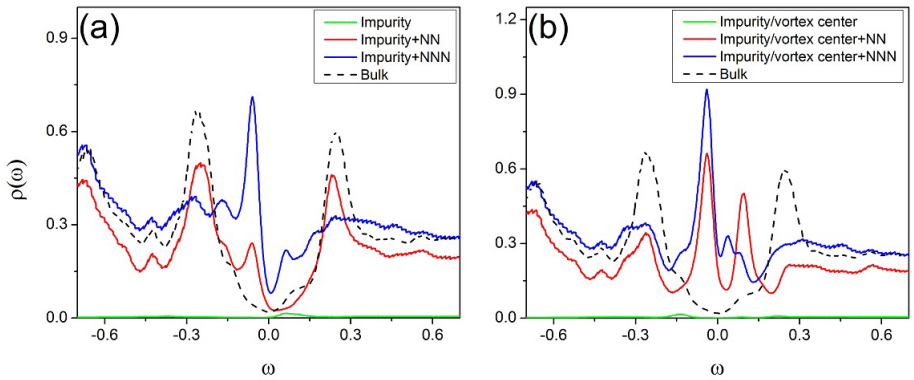

Figure 4.7: The LDOS spectra at four typical positions near the impurity (a) away from the vortex center $(24, 12)$ and (b) at the center of the vortex core $(24, 12)$. The scattering potential of the impurity is $V = -20$, and the doping level is $n = 1.8$.

scattering potential impurities are placed.

Fig. 4.7 shows the LDOS spectra results in optimal-doped case $n = 1.8$. Fig 4.7(a) shows the results away from the vortex. Still the LDOS on the impurity site is very small. At the NN site, there is only one in-gap peak located at the negative side of the Fermi energy. At the NNN site, the peak at negative side gets much higher and another peak at positive side of the Fermi energy emerges. In Fig. 4.7(b) the impurity is located inside the vortex core. Similar to the scenario in the previous section, the negative-side peak on the NN site is enlarged and another positive-side peak appears at the same location as shown in Fig. 4.1(d). All these results are consistent with those shown in Fig 4.4.

The results of under-doped case $n = 1.92$ are shown in Fig. 4.8. In Fig. 4.8(a) where impurity is away from vortex core, two in-gap peaks are located on the positive and negative side of the Fermi energy in both NN and NNN sites. When the impurity is placed inside the vortex core, as shown in Fig. 4.8(b), the single gap

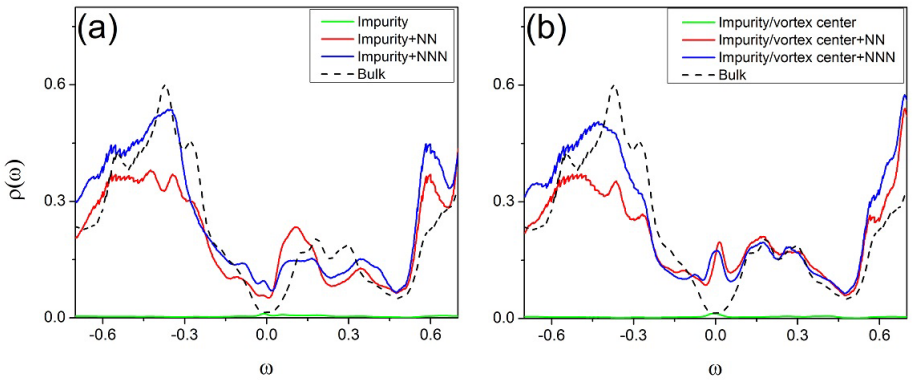

Figure 4.8: The LDOS spectra at four typical positions near the impurity (a) away from the vortex center $(24, 12)$ and (b) at the center of the vortex core $(24, 12)$. The scattering potential of the impurity is $V = -20$, and the doping level is $n = 1.92$.

close to the Fermi energy emerges again. Fig. 4.6(d) shows that the AFM order is suppressed near the impurity site inside the vortex core. Such results reinforce the competition relationship between AFM order and the single in-gap peak near Fermi energy induced by the vortex core state.

4.5 Conclusions

In this chaptor I have studied the single strong impurity effect in the vortex core state as a pinning center in hole-doped Fe-pnictide superconductivity. For the system without impurities, in the optimal doped case the resonance peak located slightly negative to the Fermi energy gradually splits into two when moving from the vortex core center to the outside, while another peak at the positive side does not split but only decreases its height. In the under-doped case additional to the emergence of the CAF-SDW in the entire lattice, an extra pattern with period $24a_0$ modulates

the existence SDW and forms a stripe-like structure. Due to the appearance of the superlattice modulation, the vortex core size has been enlarged and has also been stretched along the y-axis. LDOS calculation shows that the existence of AFM order will suppress the formation of the in-gap resonance peak slightly negative to the Fermi energy.

The system with strong impurities inside and far away the vortex core was also investigated. In the optimal-doped case, comparison between impurities placed inside and away from the vortex core does not give much difference on the NN site LDOS. As to the NNN site, the LDOS within the vortex core shows an extra peak on the positive side of Fermi energy compared to the other. This peak can be recognized as the vortex core state property. In the under-doped case, the superlattice modulation appears again. Since the AFM order is suppressed near the impurities by strong impurity effect, the in-gap resonance peak slightly negative to the Fermi energy induced by vortex core state is no longer suppressed by AFM and shows up in the LDOS spectra on both NN and NNN sites. Consequently, the impurity resonance peak may be used to identify the nature of vortex core state of hole-doped Fe-pnictide superconductors.

Chapter 5

Disorder effect with single or multiple Zn impurities in doped 122 Fe-pnictides

5.1 Introduction

The role of the doped atoms in the Fe-based superconductors (FeSC) is still controversial [101–105]. It is hotly debated whether the doping effect is dominated by providing extra charge carriers in the system, or inducing scattering potential near the doped atoms, or a combination of the both [106]. The experience on studying the cuprate superconductor suggested that disorder effects in superconductors is promising in addressing the pairing symmetry. Therefore the study of impurity scattering effect on FeSC has gathered much attention since their discoveries. The

Zn-doped FeAs-122 family is among these works. Some recent experiments [107, 108] on high quality single crystalline $Ba(Fe_{1-(x+y)}Zn_xCo_y)_2As_2$ compounds suggested that the SC order is almost fully suppressed above a concentration of roughly 8% Zn doping, no matter whether the sample is in under-, optimal- or over-doped regimes. Further measurements [109] on the hole-doped $Ba_{0.5}K_{0.5}(Fe_{1-x}Zn_x)_2As_2$ compound also showed that the superconductivity is suppressed by Zn impurities. The disorder effect of a single Zn impurity in doped Fe-pnictides was carefully studied in different doping regimes [100]. In that work the magnetic, SC order parameter, electron density, and LDOS were calculated near the impurity site, a suppression of SC order near impurity was obtained according to the calculated results. A recent theoretical work [110] has investigated the effect of Zn impurity induced disorder in FeSC with both s±- and s++-wave pairing symmetries based on a two-orbital model [47]. In this work, both on-site (favoring s++-wave symmetry) and NNN inter-site (favoring s±-wave symmetry) pairing interaction are taken into consideration, and the reap-space BdG calculations showed that the NNN order would be suppressed by Zn impurities while the on-site order remains barely unchanged. This proposal may provide a flexibility to explain various experimental data, although further experimental evidence for s++-wave symmetry is needed. Another theoretical work [57] based on a minimal two-orbital model [50] which includes only NNN pairing interactions made its own success in explaining some of the Zn doping experimental results. Unlike an earlier theoretical prediction that the SC order is fully suppressed at only 1% of Zn impurity concentration in FeSC, this work [57] showed that the SC order will not be destroyed until the impurity concentration reaches roughly 10% in the optimal-doped

regime, which is very close to the experimental measurements [107, 108]. However a calculation in the under-doped regime where SDW and SC orders coexist has not been made.

In the previous works [57, 100], Zn atoms were treated as a nonmagnetic impurity with negative scattering potential in the strong unitary scattering limit. This is based on the first-principle calculations which showed that the Zn-3d impurity level is considerably far below the Fe-3d level [106, 111, 112]. However Zn-3d orbital has already been fully occupied by its own electrons, so there is no more orbitals to store extra electrons from other Fe sites. The Zn-4s orbital electrons are more chemically active than 3d when forming chemical bonds, which means that it is reasonable to focus on the Zn-4s, rather than 3d orbital, when considering the disorder effect of Zn impurities. The electronegativity of Fe (1.83) is larger than that of Zn (1.65), which means the Fe atoms are more powerful in attracting electrons than Zn when they are forming chemical compounds. Hence I treat the Zn impurity as a repulsive center to electrons in the system, which will make the scattering potential on the Zn impurity site to be positive. One significant difference between 4s and 3d orbital electrons is that the s-wave orbital is isotropic in real space, therefore the hopping integral differences caused by the different spacial orientation of Fe d-orbitals will vanish around the Zn impurity sites.

In this chapter, I will study the disorder effect of the single and multiple Zn impurities on the superconducting and LDOS properties of FeAs-122 family superconductors. In particular, I aim to address the question of how the SC order can be completely suppressed at 8% of Zn doping in 122-type compounds at both optimal-

and under-doped regimes. In order to address this issue, I start from a minimal two-orbital model for FeAs-122 family compounds [50], and use the mean-field BdG equations to calculate the local magnetization, the SC order parameter, the electron density, and LDOS spectra. I first calculate the single impurity effect in different doping regimes. Both magnetization and SC orders are locally suppressed near Zn impurity, as expected in experiments [107, 108] and other theoretical works [57, 100]. Our LDOS calculation results show that in-gap resonance peaks are formed in almost every doping regime. The C_4 symmetry around the impurity site in the system is broken due to the single orbital in Zn impurities. Then I study the disorder effect of multiple impurities in both under-doped and optimal-doped regimes. Our calculation results indicate that the SC order can be fully suppressed when the impurity concentration reaches as high as about 8%, which agrees very well with the experiments on the $Ba(Fe_{1-(x+y)}Zn_xCo_y)_2As_2$ compounds [108]. These studies reveal that our analysis on the Zn impurity takes a solid step towards fully understanding the disorder effect in doped 122 Fe-pnictides. The obtained LDOS spectra on single Zn impurity in different dopings could be tested by future STM experiments.

5.2 Model and formalism

In the present chapter, Y. Tai's model, mentioned in Sec. 1.3, is used to perform calculations of the magnetic, SC order parameters, and LDOS spectra. The model has been successfully used to theoretically describe the magnetic, SC, and band structure properties of FeAs-122 family superconductors [56, 57, 100]. Consider the

Hamiltonian $H = H_0 + H_{SC} + H_{int} + H_{imp}$ that describes the energy of charge carriers. H_0 is the hopping terms and chemical potential, H_{SC} is the pairing interaction energy of the electrons, and H_{int} is the mean-field magnetic interaction energy. The specific forms of these three terms can be found in Eq. 1.2, 1.3, and 1.4. H_{imp} is the impurity term

$$H_{imp} = \sum_{Ij\nu\sigma} \{-t'_{I\mu j\nu} c^{\dagger}_{I\mu\sigma} c_{j\nu\sigma} + V_I c^{\dagger}_{I\mu\sigma} c_{I\mu\sigma}\}, \tag{5.1}$$

where I represents the impurity site. Here the impurity means that an Fe atom at lattice site I is substituted by Zn atom. The t' term is the hopping term between one Zn impurity and one Fe atom. Based on the spherical spatial orientation of the Zn 4s orbital, the hoppings should be isotropic along different directions. The specific hopping terms Zn-4s to Fe-3d_{xz} and Zn-4s to Fe-3d_{yz} are shown in Fig. 5.1. The first-nearest-neighbor (1NN) hopping, second-nearest-neighbor (2NN) hopping, and third-nearest-neighbor (3NN) hopping are included in the model. The impurity potential V_I means that the Fe atom is replaced and has a different on-site energy that acts as a scattering center. The summation is over all the impurity sites in the system, there is no summation over orbital μ because the Zn 4s contains only one orbital.

The eigenvalues and eigenfunctions of the total Hamiltonian H can be obtained by self-consistently solving the BdG equations shown in Eq. 1.19. Throughout this work, the hopping terms are set as $t_{(1-6)} = (-1, 0.08, 1.35, -0.12, 0.09, 0.25)$, and the pairing interaction strength, onsite Coulomb interaction, and Hunds coupling parameters are $V = 1.05$, $U = 3.2$, and $J_H = 0.6$, as shown in [55] that led to a phase diagram qualitatively consistent with experiments. The chemical potential

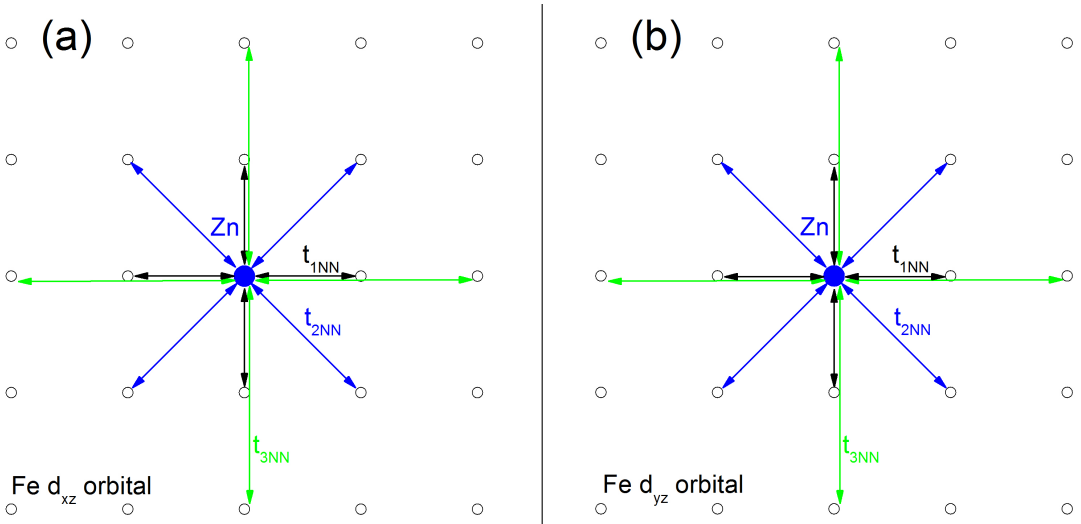

Figure 5.1: The illustration diagram of the Zn-Fe hopping terms between Zn-4s orbital and (a) Fe-3d_{xz} orbital and (b) Fe-3d_{yz} orbital. The blue solid ball represents the Zn-4s orbital and the black open balls represent the Fe-3d orbitals. The black, blue, and green solid lines are the first-nearest-neighbor (1NN), second-nearest-neighbor (2NN), and third-nearest-neighbor (3NN) hopping terms respectively.

t_0 is determined by the electron filling per orbital. I consider only NNN pairing interaction between same orbitals on Fe sites. Such a choice would give rise to SC order parameters with a sign change between the electron- and hole-like FS pockets with s±-wave pairing symmetry [95, 95, 113–115]. The impurity hopping terms are $t_{1\mathrm{NN}-3\mathrm{NN}} = (-1, 1.35, 0.25)$, and the scattering potential on the impurity site is set to be $V_I = 20$. In the following calculations, the collinear SDW order parameter is defined as $m_i = (-1)^{i_x} \frac{1}{4} \sum_\mu (\langle n_{i\mu\uparrow} \rangle - \langle n_{i\mu\downarrow} \rangle)$, and the s±-wave pairing order parameter is defined as $\Delta_i = \frac{1}{8} \sum_{j\mu} \Delta_{i\mu j\mu}$. The LDOS proportional to the differential tunneling conductance as measured by STM experiment can be calculated according to Eq. 1.27, where the delta function $\delta(x)$ is taken as $\Gamma/\pi(x^2 + \Gamma^2)$, with $\Gamma = 0.004$. All the numerical calculations are performed on 32×32 lattice with periodical boundary conditions. A 32×32 supercell is used to calculate the LDOS.

The system can be numerically solved according to the steps listed in Sec. 1.6. The only difference in this chapter is that the Zn atoms which replace Fe atoms have only one orbital each, so the total orbital number of the entire lattice is $(N_x \times N_y \times 2 - N_{imp})$ where N_{imp} is the number of Zn impurities. Then the matrix size in the BdG equations in Eq. 5.5 is $[(N_x \times N_y \times 2 - N_{imp}) \times 2]^2$.

5.3 Single impurity effect

Before I study the complex multiple impurity system, the effect of a single Zn impurity in different doping regimes is discussed in this section. Both the spatial modulation of order parameters and the LDOS spectra near the impurity site are

investigated. In the absence of an impurity, our two orbital model naturally captures the relation between magnetic and SC orders and successfully obtained the whole phase diagram in both electron- and hole-doped regions. Hence I shall restrict the calculations within this set of interaction parameters except the modification near impurity site.

5.3.1 Spatial modulation of order parameters

I begin by discussing the spatial modulation of the charge, SC and magnetic order parameters under the effect of a single Zn impurity. In all of my calculations, the single impurity is placed at the center of lattice site $I = (16, 16)$. For the impurity site, the order parameters are not averaged over different orbitals since only one orbital Zn-4s is considered. The SC order parameter in this work considers only s-wave component, because the d-wave component is only 8% in magnitude compared to the dominant s-wave [50], and it does not change our discussion and conclusions of the spatial modulations of order parameters.

The three-dimensional (3D) images of spatial profiles of charge and SC orders at electron filling $n = 2.08$ are shown in Fig. 5.2. Due to the strong repulsive potential at the Zn impurity site, the site is fully non-occupied with local electron density to be zero. As shown in Fig. 5.2(a), the sharp drop of electron density in the center of the lattice is induced by this repulsive scattering potential. At a distance of about three lattice constants from the impurity site, the charge order will recover to its bulk value $n = 2.08$. The SC order parameter as shown in Fig. 5.2(b) is very close

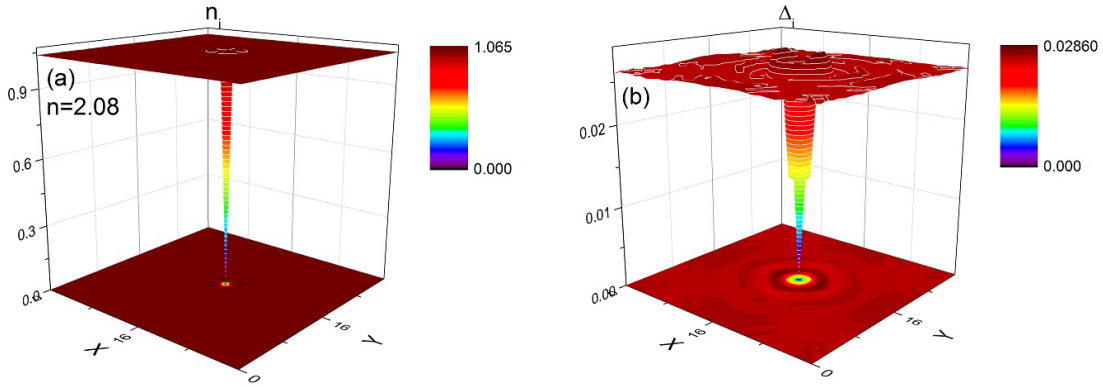

Figure 5.2: The typical three-dimensional spacial modulation of (a) the charge density order and (b) SC order parameters with a single impurity at electron-doping level $n = 2.08$.

to zero at the impurity site. The SC order of the neighboring sites is also partially suppressed, until it returns to its bulk value at a distance of $4 \sim 5$ lattice constants.

Fig. 5.3 shows the two-dimensional (2D) images of spatial profiles of charge and SC order parameters at different electron-doping levels. Form the left panel of Fig. 5.3, the charge density of four NNN sites around the Zn impurity will be enhanced due to the repulsive potential of the disorder effect. For the under-doped cases Fig. 5.3 (a) and (c), the charge density of NN sites along x-direction is slightly different from those along y-direction, this can be explained from the inhomogeneity induced by the collinear SDW order coexisting with the SC phase. When it goes to the optimal- and over-doped cases as shown in Fig. 5.3(e) and (g), this difference betwen x- and y-directions NN sites disappears along with the SDW order. The right panel of Fig. 5.3 shows the SC order parameters. The SC orders do not show any spatial inhomogeneity along x- and y-direction, they just gradually return to the bulk values after $4 \sim 5$ lattice constants. Fig. 5.4 shows the 3D spatial profiles of

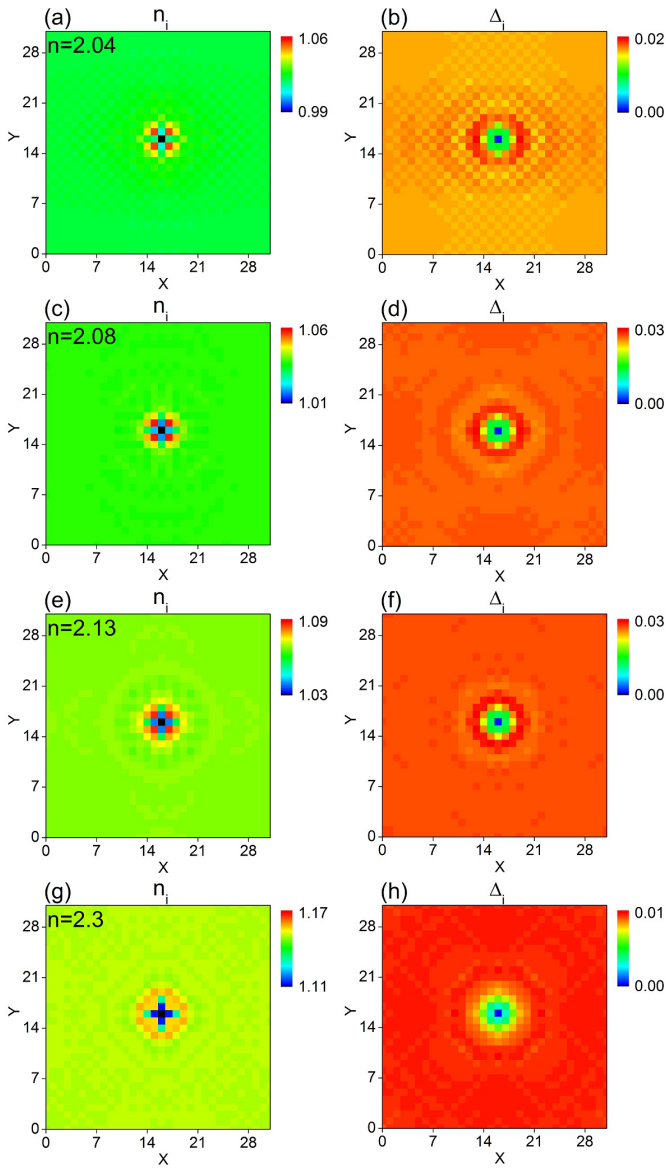

Figure 5.3: The two-dimensional images of charge density order and SC order parameters with a single impurity in the electron-doped region at different doping levels (a)(b) $n = 2.04$, (c)(d) $n = 2.08$, (e)(f) $n = 2.13$ and (g)(h) $n = 2.3$. The left panel shows the charge density, and the right panel shows the SC order parameter.

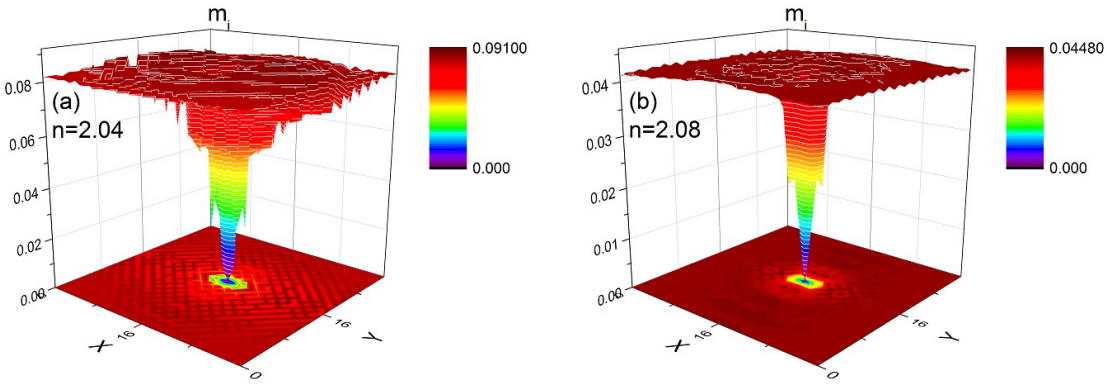

Figure 5.4: The spacial profiles of the magnetic order parameter m_i around the single impurity site in the electron-doped region at different doping levels (a) $n = 2.04$ and (b) $n = 2.08$.

the magnetic order for two different electron-doping levels inside the under-doped regime. The magnetism at the impurity site is very close to zero in both cases. The magnetic order returns to its bulk value at a distance of about $4 \sim 5$ lattice constants in x-direction and 2 lattice constants in y-direction, which is also can be explained by the spacial inhomogeneity induced by the collinear SDW order. In the optimal- and over-electron-doped regimes, there exists practically no magnetism in the bulk as well as near the impurity site.

After the electron-doped cases, I will investigate the spatial modulation of the order parameters in the hole-doped region. Fig. 5.5 shows the 2D images of charge density and SC order parameters at different hole-doping levels. In the under-doped case $n = 1.9$ as shown in Fig. 5.5(a), the charge density of four NNN sites around the impurity site is enhanced. And similarly to the electron-doped cases, the charge density of NN sites along x-direction is different from those along y-direction. The right panel of Fig. 5.5 shows the SC order parameters in the hole-doped regimes.

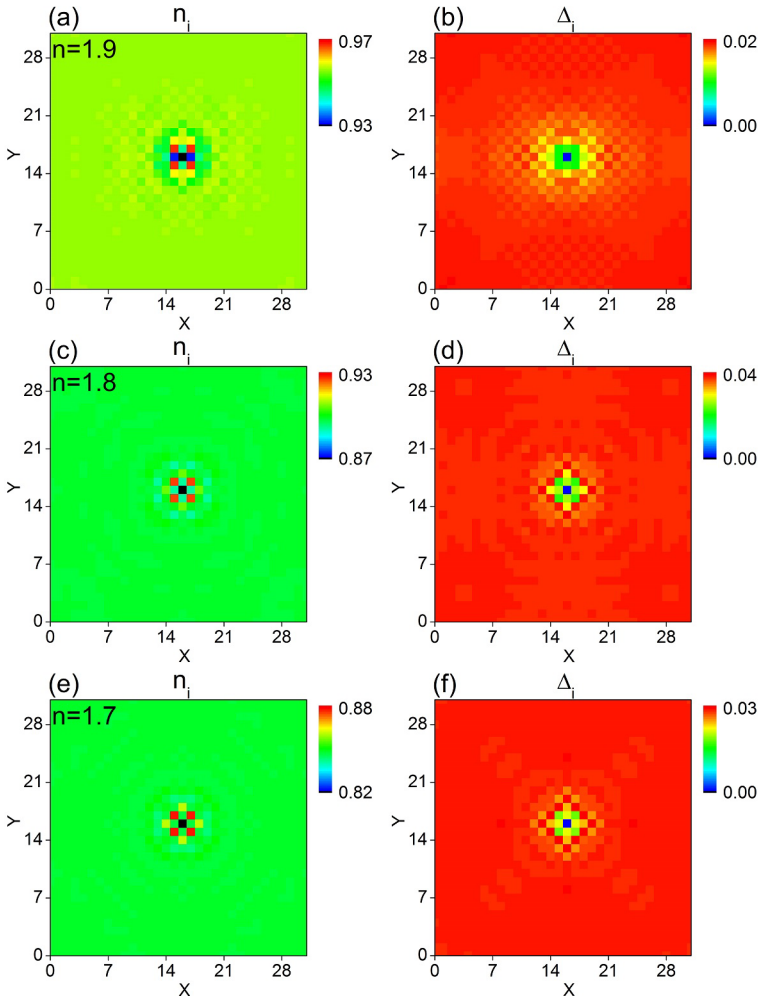

Figure 5.5: The two-dimensional images of charge density order and SC order parameters with a single impurity in the hole-doped region at different doping levels (a)(b) $n = 1.9$, (c)(d) $n = 1.8$ and (e)(f) $n = 1.7$. The left panel shows the charge density, and the right panel shows the SC order parameter.

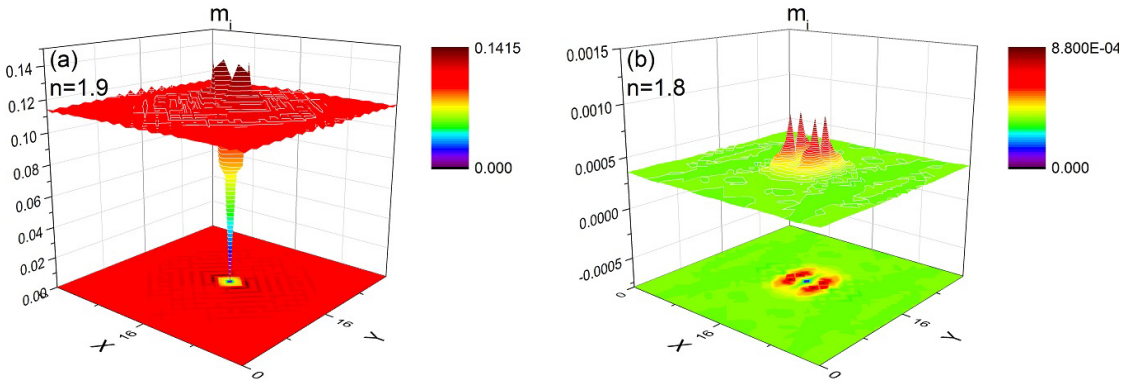

Figure 5.6: The spacial profiles of the magnetic order parameter m_i around the single impurity site in the hole-doped region at different doping levels (a) $n = 1.9$ and (b) $n = 1.8$.

Again there is no spatial inhomogeneity along x- and y-directions according to the SC orders, they will gradually return to the bulk values after $4 \sim 5$ lattice constants. Fig. 5.6 shows the 3D spatial profiles of the magnetic order for different hole-doping levels. The under-doped case in Fig. 5.6(a) where $n = 1.9$ is very similar to the electron-doped one Fig. 5.4(a) and (b) except that the magnetic order on the NNN sites of the impurity is enhanced under the impurity effect. However, unlike the electron-optimal-doped case, in the hole under-doped case Fig. 5.6(b) where $n = 1.8$, weak magnetic order around the impurity site is induced. This weak magnetic order induced near the impurity site is not observed in the optimal-electron-doped cases. This feature has also been reported in a previous study [100] of the single impurity effect.

5.3.2 The local density of states

In order to further investigate the disorder effect of a single Zn impurity, the LDOS spectra near the impurity site is calculated. Due to the strong repulsive scattering potential on the impurity site, the LDOS will vanish on that site. However the impurity-induced in-gap bound states can be found on the neighboring sites. Two previous works [57, 100] mentioned that when the impurity scattering potential V is large enough ($|V| > 15$), the characteristics of the in-gap bound states and other calculated results would be very insensitive to the precise value of $|V|$. Therefore our calculations should be comparable to the STM experimental measurements.

Fig. 5.7 shows the calculated LDOS spectra results for under- and optimal-electron-doped cases. As shown in Fig. 5.7(a) for the under-doped $n = 2.04$ case, two in-gap resonance peaks emerge at both positive and negative sides of the Fermi energy at NN and NNN sites of the impurity. The intensity of the left peak is much higher than for the right one on every NN and NNN sites. With doping level increasing to $n = 2.08$ in Fig. 5.7(b), these two in-gap peaks will move further away from each other and get closer to the SC coherence peaks on each side. When going into the optimal-doped region $n = 2.13$ as shown in Fig. 5.7(c), the intensity of the in-gap peak on the negative side of Fermi energy significantly shrinks. In the over-doped case $n = 2.3$ in Fig. 5.7(d), the intensities of the resonance peaks at both positive and negative sides are getting similar. Based on the existence of collinear SDW in the under-doped regimes, it is easy to understand the nonequivalent LDOS results on the NN sites along x- and y-directions. However, the LDOS spectra results on the NNN sites along $(1, 1)$ direction are different with those on the NNN sites along $(-1, 1)$

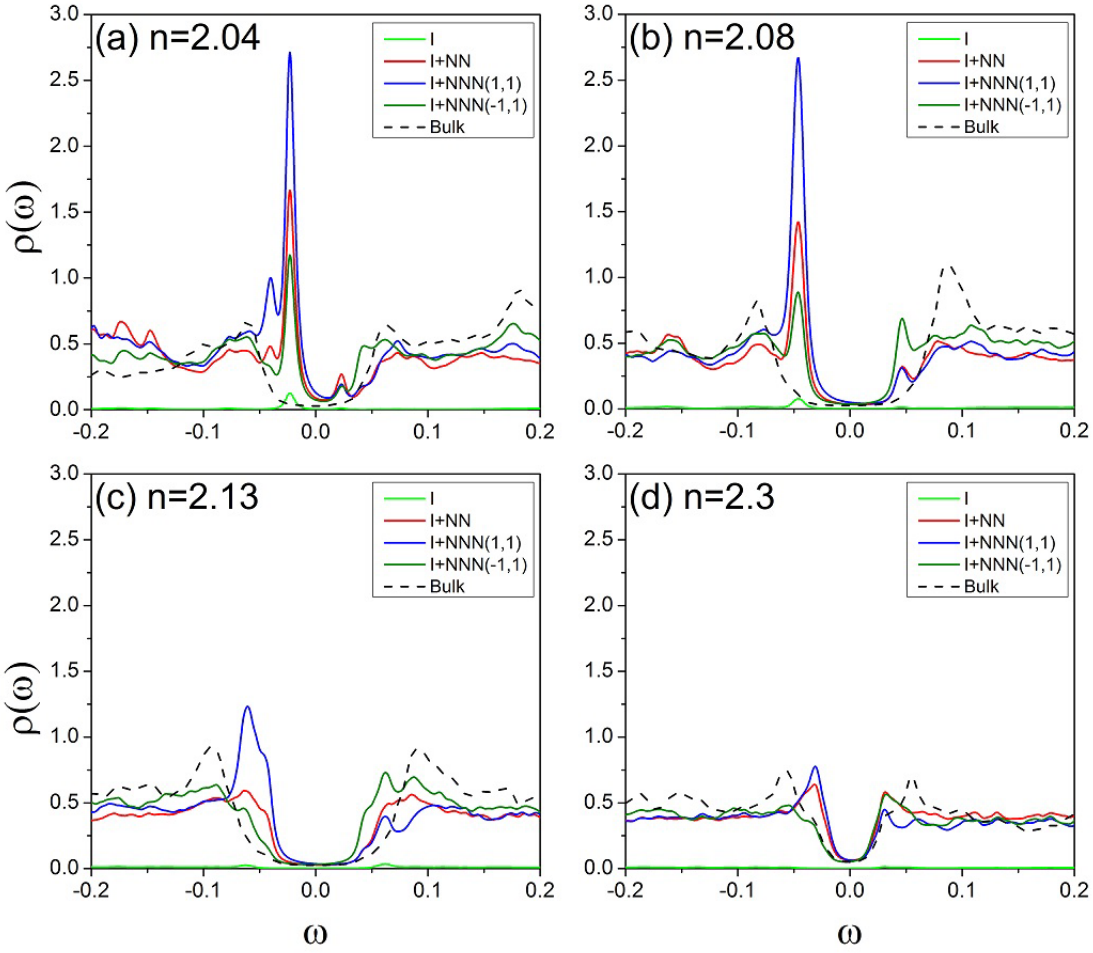

Figure 5.7: The local density of states spectra in the electron-doped region at different doping levels (a) $n = 2.04$, (b) $n = 2.08$, (c) $n = 2.13$ and (d) $n = 2.3$. The green, red, blue and dark green solid lines represent the results at the impurity site, at the nearest-neighbor site of the impurity, at the next-nearest-neighbor site along the $(1, 1)$ direction of the impurity and at the next-nearest-neighbor site along the $(-1, 1)$ direction of the impurity respectively. The black dashed lines represent the bulk values.

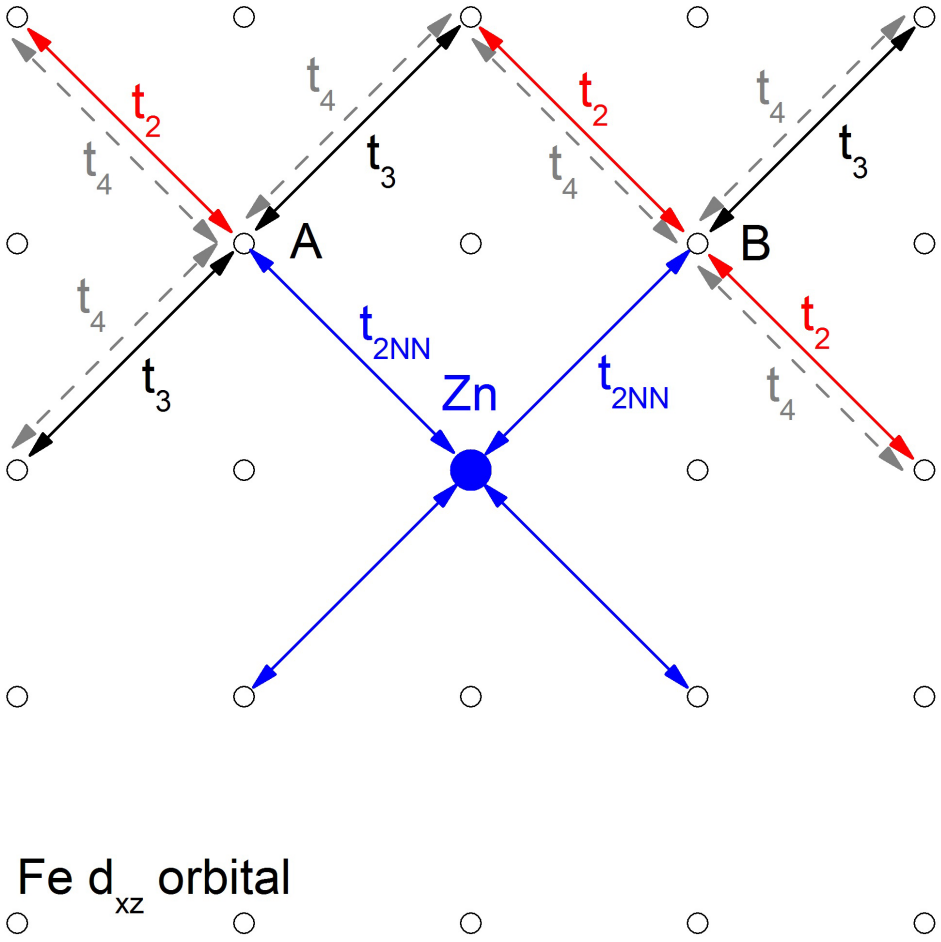

Figure 5.8: All the next-nearest-neighbor hoppings of Fe-3d_{xz} orbital at lattice sites A and B. The blue solid ball represents the Zn-4s orbital and the black open balls represent the Fe-3d_{xz} orbitals. Blue solid lines are Zn-Fe hoppings while all the other lines are Fe-Fe hoppings.

direction not only in the under-doped region, but also in the optimal- and over-doped regions where collinear SDW order no longer exists. In contrast, a previous study on the single Zn impurity effect [100] showed that the system has C_4 symmetry in optimal- and over-doped regimes where SDW order vanishes, which means that the LDOS spectra results on the NNN sites along $(1,1)$ direction are the same as those along $(-1,1)$ direction. Such asymmetric phenomenon in our calculation can be understood from the one-orbital property of the Zn impurity. All the NNN hoppings related to the d_{xz} orbital of two Fe sites at $(1,1)$ and $(-1,1)$ direction of a Zn impurity site are shown in Fig. 5.8. According to the NNN hoppings as shown in the Fig. 5.8, one hopping is replaced by the new Zn-Fe hopping terms. Apparently the replaced NNN hoppings are different in these two Fe sites, which makes these two Fe sites are longer equivalent to each other. This nonequivalent hopping term leads to the asymmetric LDOS spectra on different NNN sites, and furthermore breaks the C_4 symmetry even in the optimal- and over-doped regions where collinear SDW order no longer exists. This property can be regarded as a signature of the Zn-4s orbital model, and can be tested in the future experimental measurements.

Fig. 5.9 shows the LDOS results for two hole-doped cases. At the under-doped case $n = 1.9$, two ingap resonance peaks emerge at both positive and negative sides of the Fermi energy. These peaks are relatively small compared to the SC coherence peaks. As in the optimal-hole-doped case $n = 1.8$, four ingap peaks appear on the NNN sites along $(-1,1)$ direction with two on each side of the Fermi energy, the intensities of the peaks on both sides are very close. However on the NNN sites along $(1,1)$ direction, the resonance peaks on the positive side shrink to a small

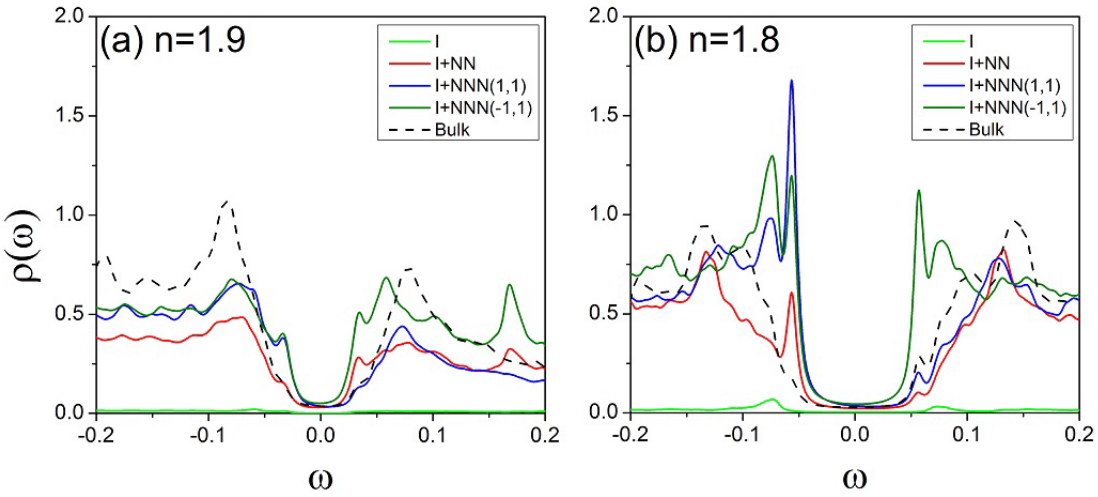

Figure 5.9: The local density of states spectra in the hole-doped region at different doping levels (a) $n = 1.9$ and (b) $n = 1.8$. The green, red, blue, and dark green solid lines represent the results at the impurity site, at the nearest-neighbor site of the impurity, at the next-nearest-neighbor site along the $(1, 1)$ direction of the impurity and at the next-nearest-neighbor site along the $(-1, 1)$ direction of the impurity respectively. The black dashed lines represent the bulk values.

one, which enlarges the difference between the peaks on both sides significantly. The asymmetric LDOS results in the optimal-doped region where no collinear SDW order exists can also be understood by the nonequivalent hopping terms in our model.

5.4 Multiple impurity effect

In this section, I will investigate the disorder effect on SC order parameters by multiple Zn impurities. In order to do that, the SC order averaged over the entire lattice $\Delta = \frac{1}{N}\sum_i \Delta_i$ is calculated, here N is the total number of lattice sites. The final SC orders shown in this section are averaged over 20 different configurations of randomly-distributed Zn impurities. Since the error bar of each point is smaller than the point itself, they are not shown on the graph. As most of the multiple Zn impurities measurements are on the electron-doped $Ba(Fe_{1-(x+y)}Zn_xCo_y)_2As_2$ compounds, I will focus on the electron-doped region in the following calculations.

As shown in Fig. 5.10, the suppression of SC order with increasing Zn impurity concentration in both under- and optimal-electron-doped regimes is calculated. I find that the averaged SC order decreases while the concentration of Zn impurities increases, and finally vanishes to zero at a critical concentration of about $n_{imp} = 8\%$ in both under- and optimal-doped case. Our results here are in very good agreement with the experimental measurements in $Ba(Fe_{1-(x+y)}Zn_xCo_y)_2As_2$ compounds [108].

In order to provide an intuitive picture of the disorder effect on the SC order parameter with increasing Zn impurity concentration, the spatial profiles of SC order parameter in optimal-doped region on two realizations of Zn impurity configurations

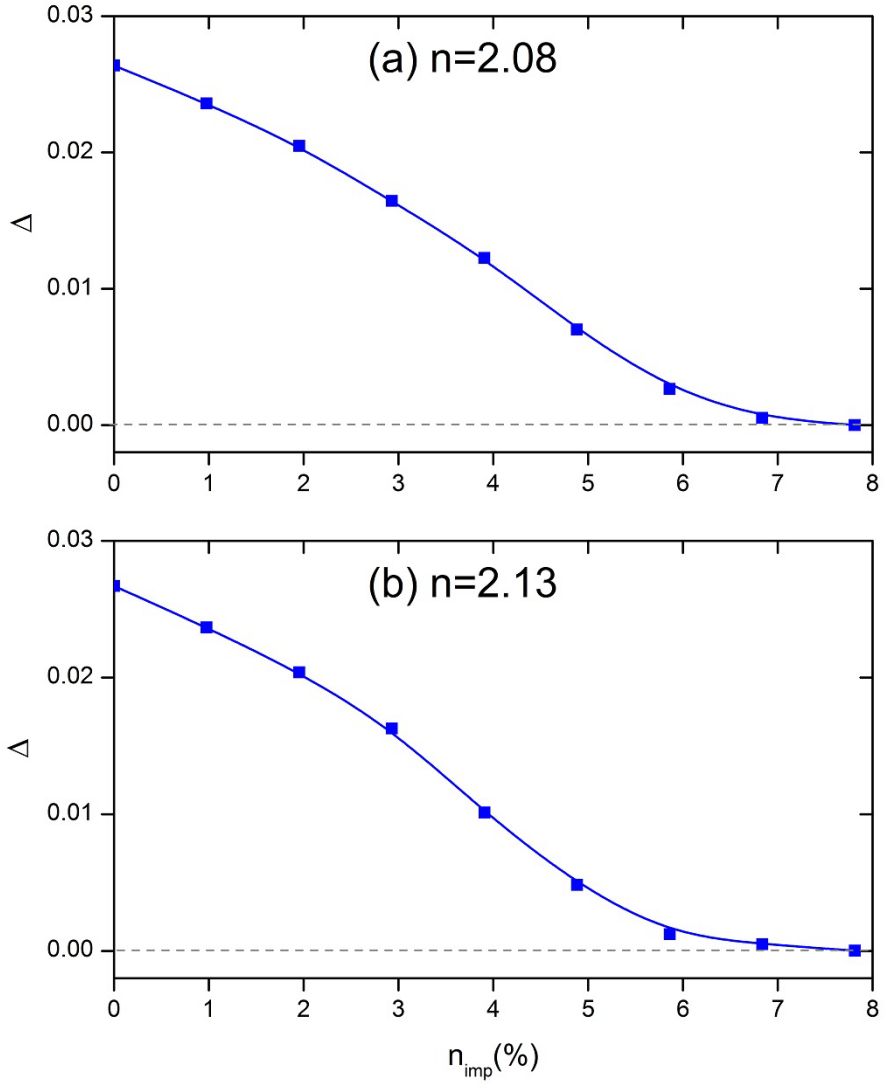

Figure 5.10: The averaged superconducting order parameter over the entire lattice in the electron-doped region at doping levels (a) $n = 2.08$ and (b) $n = 2.13$. The SC orders are averaged over 20 different configurations of randomly distributed Zn impurities. The solid line is fitted to guide the eye.

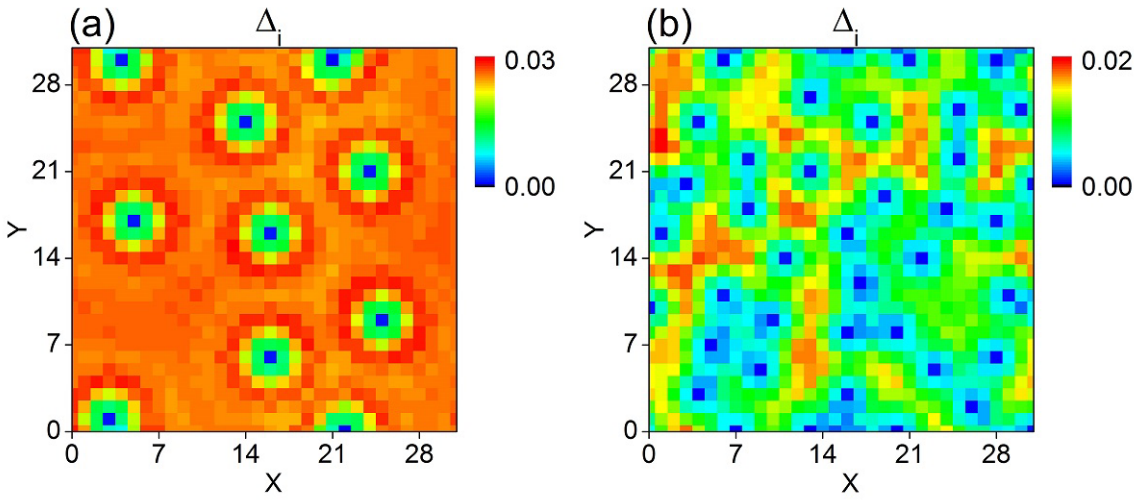

Figure 5.11: The two-dimensional spacial profiles of SC order parameters for a typical impurity configuration with the Zn impurity concentration (a) $n_{imp} = 0.97\%$ and (b) $n_{imp} = 3.9\%$.

are investigated. As shown in Fig. 5.11, the SC order parameters with impurity concentrations $n_{imp} = 0.97\%$ and $n_{imp} = 3.9\%$ are calculated. In Fig. 5.11(a), it is clear to see that the SC order is suppressed near the impurity site while the bulk value remains unchange compared to the impurity-free system. This means that the impurities behave individually when the impurity concentration is small enough. However when the impurity concentration is relatively large as shown in Fig. 5.11(b), the interference of the local order parameter at each impurity site is observed. These correlated sites form islands and break the system into several SC and non-SC clusters. Similar SC order parameter structure was also observed in a previous theoretical work [57].

5.5 Conclusions

In summary, by solving the lattice BdG equations self-consistently, I have studied disorder effect with single and multiple Zn impurities based on a two-orbital model with s±-wave pairing symmetry. The Zn impurity sites are considered as repulsive centers to electrons with positive scattering potential. The single Zn-4s orbital, instead of Zn-3d, is included in the model. The magnetic, SC, charge density order, and LDOS with single Zn impurity are investigated. Our calculations show that all the order parameters are suppressed near the impurity. In-gap resonance peaks on both negative and positive sides of the Fermi energy are observed in LDOS spectra. I have also investigated the disorder effect with multiple Zn impurities. The results of both under- and optimal-doped cases show that the SC order will be fully suppressed when the Zn concentration reaches as high as 8%. This result agrees very well with the recent experimental measurements on $Ba(Fe_{1-(x+y)}Zn_xCo_y)_2As_2$ compounds [108]. The local SC order calculation shows that although the impurities behave individually when the impurity concentration is small, the interference of the local order parameter at each impurity site is observed in a relatively large concentration percentage. The LDOS results near a single Zn impurity on the NNN sites along $(1,1)$ direction are different with those on the NNN sites along $(-1,1)$ direction in the optimal- and over-doped regions where collinear SDW order no longer exists. Such asymmetric phenomenon is induced by the spatially nonequivalent Zn-Fe hopping terms and reveals a broken of C_4 symmetry. This property can be regarded as a signature of the Zn-4s orbital model, and can be tested in the future experimental measurements.

Chapter 6

Summary

The Fe-based HTS system is highly complicated, and no theory has given a satisfying explanation to it so far. My work was intended to narrow the gap between experimental frontier and the following theoretical study. Driven by several interesting experiments, the Fe-based HTS systems under different types of effects are investigated.

First, the system was under the effect of different types of twin boundaries. For the four kinds of twin boundaries studied in chapter 2, the domain wall structures in cases A, B, and D were found to be pinned at the twin boundaries, while in case C the domain walls are separated from the twin boundaries. In cases of A, B, and C, the SC is enhanced in the regions near the domain walls where the magnetic order is suppressed. The reason for this is that the electron densities are enhanced to the optimal-doped level around the domain walls. However in case D, on the domain walls where the magnetic order is suppressed, the carrier density is close

to the over(hole)-doping level, and this is also unfavorable to SC. As a result, SC coexists with the magnetism in the middle of magnetic domains. Cases of C and D have not been detected directly in an experiment, the calculated results can be treated as predictions which could be tested by measuring the superfluid density on the twin boundaries using SQIDM [16].

Second, the system was under the effect of highly electron-doped charge carriers. By including both of the NN and the NNN intraorbital pairing interactions, in chapter 3 I showed that the pairing symmetry of the SC changes from $s_{\pm}$-wave to d-wave like in highly electron-doped $A_xFe_2Se_2$. The transition occurs when the hole pockets near the Γ point in the FS are just completely filled up by doped electrons. The absence of SC phase with d-wave symmetry in highly electron-doped $Ba(Fe_{1-x}Co_xAs)_2$ can be attributed to the presence of the weak scattering effect due to the randomly distributed Co impurities in this compound. In order to test the existence of the d-wave SC in highly electron-doped $A_xFe_2Se_2$, I suggested to look for the signature of the in-gap states by STM experiments.

Third, the system was under the effect of magnetic field and single Zn impurity. As shown in chapter 4, I studied the system with strong impurities inside and far away the vortex core. In the optimal-doped case, comparison between impurities placed inside and away from the vortex core does not give much difference on the NN site LDOS. As to the NNN site, the LDOS within the vortex core showed an extra peak on the positive side of Fermi energy compared to the other. This peak can be recognized as the vortex core state property. In the under-doped case, the superlattice modulation appears. Since the magnetic order is suppressed near the

impurities by strong impurity effect, the in-gap resonance peak slightly negative to the Fermi energy induced by vortex core state is no longer suppressed by antiferromagnetic order and shows up in the LDOS spectra on both NN and NNN sites. Consequently, the impurity resonance peak may be used to identify the nature of vortex core state of hole-doped Fe-pnictide superconductors.

Lastly, the system was under the effect of single or multiple Zn impurities in chapter 5. The Zn impurity sites were considered as repulsive centers to electrons with positive scattering potential. The single Zn-4s orbital, instead of Zn-3d, was included in the model. The magnetic, SC, charge density order, and LDOS with single Zn impurity were investigated. My calculations showed that all the order parameters are suppressed near the impurity. In-gap resonance peaks on both negative and positive sides of the Fermi energy were observed in LDOS spectra. I also investigated the disorder effect with multiple Zn impurities. The results of both under- and optimal-doped cases showed that the SC order will be fully suppressed when the Zn concentration reaches as high as 8%. This result agrees very well with the recent experimental measurements on $Ba(Fe_{1-(x+y)}Zn_xCo_y)_2As_2$ compounds [108]. The local SC order calculation showed that although the impurities behave individually when the impurity concentration is small, the interference of the local order parameter at each impurity site is observed in a relatively large concentration percentage. The LDOS results near a single Zn impurity on the NNN sites along $(1,1)$ direction are different with those on the NNN sites along $(-1,1)$ direction in the optimal- and over-doped regions where collinear SDW order no longer exists. Such asymmetric

phenomenon is induced by the spatially nonequivalent Zn-Fe hopping terms and reveals a broken of C_4 symmetry. This property can be regarded as a signature of the Zn-4s orbital model, and can be tested in the future experimental measurements.

To summarize, my work showed that based on the two-orbital model which was proposed by D. Zhang [53] and improved by Y. Tai [55], a lot of Fe-based HTS phenomena observed in experiments could be theoretically explained. This indicated that this model along with the containing pairing symmetry as least captures part of the intrinsic physics within the Fe-based HTS systems. It is a solid step towards the fully understanding of such system. Hopefully my research can be helpful in the future study of Fe-based HTS system.

Bibliography

[1] Y. Kamihara, T. Watanabe, M. Hirano, and H. Hosono. *J. Am. Chem. Soc.*, 130:3296, 2008.

[2] Z.-A. Ren, W. Lu, J. Yang, W. Yi, X.-L. Shen, Z.-C., G.-C. Che, X.-L. Dong, L.-L. Sun, F. Zhou, and Z.-X. Zhao. *Chinese Phys. Lett.*, 25:2215, 2008.

[3] X. H. Chen, T. Wu, G. Wu, R. H. Liu, H. Chen, and D. F. Fang. *Nature*, 453: 761, 2008.

[4] C. de la Cruz, Q. Huang, J. W. Lynn, J. Li, W. R. Ii, J. L. Zarestky, H. A. Mook, G. F. Chen, J. L. Luo, N. L. Wang, and P. Dai. *Nature*, 453:899, 2008.

[5] G. F. Chen, Z. Li, D. Wu, G. Li, W. Z. Hu, J. Dong, P. Zheng, J. L. Luo, and N. L. Wang. *Phys. Rev. Lett.*, 100:247002, 2008.

[6] M. Rotter, M. Tegel, and D. Johrendt. *Phys. Rev. Lett.*, 101:107006, 2008.

[7] A. Leither-Jasper, W. Schnelle, C. Geibel, and H. Rosner. *Phys. Rev. Lett.*, 101:207004, 2008.

[8] N. Ni, S. L. Budko, A. Kreyssig, S. Nandi, G. E. Rustan, A. I. Goldman, S. Gupta, J.D. Corbett, A. Kracher, and P. C. Canfield. *Phys. Rev. B*, 78: 014507, 2008.

[9] H. Q. Luo, Z. S. Wang, H. Yang, P. Cheng, X. Y. Zhu, and H. H. Wen. *Supercond. Sci. Technol.*, 21:125014, 2008.

[10] G. F. Chen, Z. Li, J. Dong, G. Li, W. Z. Hu, X. D. Zhang, X. H. Song, P. Zheng, N. L. Wang, and J. L. Luo. *Phys. Rev. B*, 78:224512, 2008.

[11] A. S. Sefat, R. Y. Jin, M. A. McGuire, B. C. Sales, D. J. Singh, and D. Mandrus. *Phys. Rev. Lett.*, 101:117004, 2008.

[12] L. J. Li, Y. K. Luo, Q. B. Wang, H. Chen, Z. Ren, Q. Tao, Y. K. Li, X. Lin, M. He, Z. W. Zhu, G. H. Cao, and Z. A. Xu. *New J. Phys.*, 11:025008, 2009.

[13] S. R. Saha, N. P. Butch, K. Kirshenbaum, and J. Paglione. *Phys. Rev. B*, 79: 224519, 2009.

[14] R. T. Gordon, H. Kim, N. Salovich, R. W. Giannetta, R. M. Fernandes, V. G. Kogan, T. Prozorov, S. L. Budko, P. C. Canfield, M. A. Tanatar, and R. Prozorov. *Phys. Rev. B*, 82:054507, 2010.

[15] T.-M. Chuang, M. P. Allan, Jinho Lee, Yang Xie, Ni Ni, S. L. Budko, G. S. Boebinger, P. C. Canfield, and J. C. Davis. *Science*, 327:181, 2010.

[16] B. Kalisky, J. R. Kirtley, J. G. Analytis, J.-H. Chu, A. Vailionis, I. R. Fisher, and K. A. Moler. *Phys. Rev. B*, 81:184513, 2010.

[17] J. Guo, S. Jin, G. Wang, S. Wang, K. Zhu, T. Zhou, M. He, and X. Chen. *Phys. Rev. B*, 82:180520, 2010.

[18] J. J. Ying, X. F. Wang, X. G. Luo, A. F. Wang, M. Zhang, Y. J. Yan, Z. J. Xiang, R. H. Liu, P. Cheng, G. J. Ye, and X. H. Chen. *Phys. Rev. B*, 83: 212502, 2011.

[19] W. Li, H. Ding, P. Deng, K. Chang, C. Song, K. He, L. Wang, X. Ma, J.-P. Hu, X. Chen, and Q.-K. Xue. *Nat. Phys.*, 8:126, 2012.

[20] T. P. Ying, X. L. Chen, G. Wang, S. F. Jin, T. T. Zhou, X. F. Lai, H. Zhang, and W. Y. Wang. *Sci. Rep.*, 2:426, 2012.

[21] J. Paglione and R. L. Greene. *Nat. Phys.*, 6:645, 2010.

[22] S. Avci, O. Chmaissem, D. Y. Chung, S. Rosenkranz, E. A. Goremychkin, J. P. Castellan, I. S. Todorov, J. A. Schlueter, H. Claus, A. Daoud-Aladine, D. D. Khalyavin, M. G. Kanatzidis, and R. Osborn. *Phys. Rev. B*, 85:184507, 2012.

[23] J. M. Tranquada, J. D. Axe, N. Ichikawa, A. R. Moodenbaugh, Y. Nakamura, and S. Uchida. *Phys. Rev. Lett.*, 78:338, 1997.

[24] H. A. Mook, Pengcheng Dai, and F. Dogan. *Phys. Rev. Lett.*, 88:097004, 2002.

[25] D. K. Pratt, W. Tian, A. Kreyssig, J. L. Zarestky, S. Nandi, N. Ni, S. L. Budko, P. C. Canfield, A. I. Goldman, and R. J. McQueeney. *Phys. Rev. Lett.*, 103: 087001, 2009.

[26] C. Lester, J. H. Chu, J. G. Analytis, S. C. Capelli, A. S. Erickson, C. L. Condron, M. F. Toney, I. R. Fisher, and S. M. Hayden. *Phys. Rev. B*, 79: 144523, 2009.

[27] X. F. Wang, T. Wu, G. Wu, R. H. Liu, H. Chen, Y. L. Xie, and X. H. Chen. *New J. Phys.*, 11:045003, 2009.

[28] Y. Laplace, J. Bobroff, F. Rullier-Albenque, D. Colson, and A. Forget. *Phys. Rev. B*, 80:140501, 2009.

[29] S. Avci, O. Chmaissem, D. Y. Chung, S. Rosenkranz, E. A. Goremychkin, J. P. Castellan, I. S. Todorov, J. A. Schlueter, H. Claus, A. Daoud-Aladine, D. D. Khalyavin, M. G. Kanatzidis, and R. Osborn. *Phys. Rev. B*, 85:184507, 2012.

[30] M. Rotter, M. Pangerl, M. Tegel, and D. Johrendt. *Angew. Chem. Int. Ed.*, 47:7947, 2008.

[31] H. Chen, Y. Ren, Y. Qiu, W. Bao, R. H. Liu, G. Wu, T. Wu, Y. L. Xie, X. F. Wang, Q. Huang, and X. H. Chen. *Europhys. Lett.*, 85:17006, 2009.

[32] F.-C. Hsu, J.-Y. Luo, K.-W. Yeh, T.-K. Chen, T.-W. Huang, P. M. Wu, Y.-C. Lee, Y.-L. Huang, Y.-Y. Chu, D.-C. Yan, and M.-K. Wu. *PNAS*, 105:14262, 2008.

[33] X. F. Wang, T. Wu, G. Wu, R. H. Liu, H. Chen, Y. L. Xie, and X. H. Chen. *New J. Phys.*, 11:045003, 2009.

[34] D. J. Singh. *Physica C: Superconductivity*, 469:418, 2009.

[35] I. I. Mazin, D. J. Singh, M. D. Johannes, and M. H. Du. *Phys. Rev. Lett.*, 101: 057003, 20087.

[36] K. Seo, B. A. Bernevig, and J. Hu. *Phys. Rev. Lett.*, 101:206404, 2008.

[37] K. Kuroki, S. Onari, R. Arita, H. Usui, Y. Tanaka, H. Kontani, and H. Aoki. *Phys. Rev. Lett.*, 101:087004, 2008.

[38] Y. Zhang, L. X. Yang, M. Xu, Z. R. Ye, F. Chen, C. He, H. C. Xu, J. Jiang, B. P. Xie, J. J. Ying, X. F. Wang, X. H. Chen, J. P. Hu, M. Matsunami, S. Kimura, and D. L. Feng. *Nat. Mater.*, 10:273, 2011.

[39] X.-P. Wang, T. Qian, P. Richard, P. Zhang, J. Dong, H.-D. Wang, C.-H. Dong, M.-H. Fang, and H. Ding. *Europhys. Lett.*, 93:57001, 2011.

[40] D. Mou, S. Liu, X. Jia, J. He, Y. Peng, L. Zhao, L. Yu, G. Liu, S. He, X. Dong, J. Zhang, H. Wang, C. Dong, M. Fang, X. Wang, Q. Peng, Z. Wang, S. Zhang, F. Yang, Z. Xu, C. Chen, and X. J. Zhou. *Phys. Rev. Lett.*, 106:107001, 2011.

[41] T. Qian, X.-P. Wang, W.-C. Jin, P. Zhang, P. Richard, G. Xu, X. Dai, Z. Fang, J.-G. Guo, X.-L. Chen, and H. Ding. *Phys. Rev. Lett.*, 106:187001, 2011.

[42] M. Xu, Q. Q. Ge, R. Peng, Z. R. Ye, J. Jiang, F. Chen, X. P. Shen, B. P. Xie, Y. Zhang, A. F. Wang, X. F. Wang, X. H. Chen, and D. L. Feng. *Phys. Rev. B*, 85:220504, 2012.

[43] V. Cvetkovic and Z. Tesanovic. *Europhys. Lett.*, 85:37002, 2009.

[44] K. Kuroki, S. Onari, R. Arita, H. Usui, Y. Tanaka, H. Kontani, and H. Aoki. *Phys. Rev. Lett.*, 101:087004, 2008.

[45] P. A. Lee and X.-G. Wen. *Phys. Rev. B*, 78:144517, 2008.

[46] M. Daghofer, A. Nicholson, A. Moreo, and E. Dagotto. *Phys. Rev. B*, 81: 014511, 2010.

[47] S. Raghu, X.-L. Qi, C.-X. Liu, D. J. Scalapino, and S.-C. Zhang. *Phys. Rev. B*, 77:220503, 2008.

[48] D. Zhang. *Phys. Rev. Lett.*, 103:186402, 2009.

[49] J. Hu and N. Hao. *Phys. Rev. X*, 2:021009, 2012.

[50] Y.-Y. Tai, J.-X. Zhu, M. J. Graf, and C. S. Ting. *Europhys. Lett.*, 103:67001, 2013.

[51] T. Shimojima, K. Ishizaka, Y. Ishida, N. Katayama, K. Ohgushi, T. Kiss, M. Okawa, T. Togashi, X.-Y. Wang, C.-T. Chen, S. Watanabe, R. Kadota, T. Oguchi, A. Chainani, and S. Shin. *Phys. Rev. Lett.*, 104:057002, 2010.

[52] C.-C. Lee, W.-G. Yin, and W. Ku. *Phys. Rev. Lett.*, 103:267001, 2009.

[53] D. Zhang. *Phys. Rev. Lett.*, 103:186402, 2009.

[54] T. Zhou, D. Zhang, and C. S. Ting. *Phys. Rev. B*, 81:052506, 2010.

[55] Y.-Y. Tai, J.-X. Zhu, M. J. Graf, and C. S. Ting. *EPL*, 103:67001, 2013.

[56] L. Pan, J. Li, Y.-Y. Tai, M. J. Graf, J.-X. Zhu, and C. S. Ting. *Phys. Rev. B*, 88:214510, 2013.

[57] H. Chen, Y.-Y. Tai, C. S. Ting, M. J. Graf, J. Dai, and J.-X. Zhu. *Phys. Rev. B*, 88:184509, 2013.

[58] P. G. de Gennes. *Superconductivity of Metals and Alloys*. W. A. Benjamin, New York, 1966.

[59] Jian-Xin Zhu, B. Friedman, and C. S. Ting. *Phys. Rev. B*, 59:3353, 1999.

[60] H.-Y. Chen. *The temperature and magnetic effect in d-wave superconductivity with the competing antiferromagnetism*. Ph.D. dissertation, University of Houston, 2005.

[61] H. Huang, D. Zhang, T. Zhou, and C. S. Ting. *Phys. Rev. B*, 83:134517, 2011.

[62] K. Seo, B. A. Bernevig, and J. Hu. *Phys. Rev. Lett.*, 101:206404, 2008.

[63] I. I. Mazin, D. J. Singh, M. D. Johannes, and M. H. Du. *Phys. Rev. Lett.*, 101: 057003, 2008.

[64] M. G. Kim, R. M. Fernandes, A. Kreyssig, J. W. Kim, A. Thaler, S. L. Budko, P. C. Canfield, R. J. McQueeney, J. Schmalian, and A. I. Goldman. *Phys. Rev. B*, 83:134522, 2011.

[65] Y. Laplace, J. Bobroff, F. Rullier-Albenque, D. Colson, and A. Forget. *Phys. Rev. B*, 80:140501, 2009.

[66] M.-H. Julien, H. Mayaffre, M. Horvati, C. Berthier, X. D. Zhang, W. Wu, G. F. Chen, N. L. Wang, and J. L. Luo. *EPL*, 87:37001, 2009.

[67] D. K. Pratt, W. Tian, A. Kreyssig, J. L. Zarestky, S. Nandi, N. Ni, S. L. Budko, P. C. Canfield, A. I. Goldman, and R. J. McQueeney. *Phys. Rev. Lett.*, 103: 087001, 2009.

[68] A. D. Christianson, M. D. Lumsden, S. E. Nagler, G. J. MacDougall, M. A. McGuire, A. S. Sefat, R. Jin, B. C. Sales, and D. Mandrus. *Phys. Rev. Lett.*, 103:087002, 2009.

[69] J. Hu and N. Hao. *Phys. Rev. X*, 2:021009, 2012.

[70] C.-L. Song, Y.-L. Wang, Y.-P. Jiang, L. Wang, K. He, X. Chen, J. E. Hoffman, X.-C. Ma, and Q.-K. Xue. *Phys. Rev. Lett.*, 109:137004, 2012.

[71] H. Xiao, T. Hu, A. P. Dioguardi, N. apRoberts-Warren, A. C. Shockley, J. Crocker, D. M. Nisson, Z. Viskadourakis, Xianyang Tee, I. Radulov, C. C. Almasan, N. J. Curro, and C. Panagopoulos. *Phys. Rev. B*, 85:024530, 2012.

[72] I. I. Mazin and M. D. Johannes. *Nat Phys*, 5:141, 2009.

[73] L. Zhang and D. J. Singh. *Phys. Rev. B*, 79:094528, 2009.

[74] X.-W. Yan, M. Gao, Z.-Y. Lu, and T. Xiang. *Phys. Rev. B*, 84:054502, 2011.

[75] C. Chao and D. Jian-Hui. *Chin. Phys. Lett.*, 28:057402, 2011.

[76] I. R. Shein and A. L. Ivanovskii. *Phys. Lett. A*, 375:1028, 2011.

[77] I. A. Nekrasov and M. V. Sadovskii. *JETP Lett.*, 93:166, 2011.

[78] Y.-Y. Tai, J.-X. Zhu, M. J. Graf, and C. S. Ting. *Europhys. Lett.*, 103:67001, 2013.

[79] H. Chen, Y.-Y. Tai, C. S. Ting, M. J. Graf, J. Dai, and J.-X. Zhu. *Phys. Rev. B*, 88:184509, 2013.

[80] T. Bohm, A. F. Kemper, B. Moritz, F. Kretzschmar, B. Muschler, H.-M. Eiter, R. Hackl, T. P. Devereaux, D. J. Scalapino, and H.-H. Wen. *arXiv*, 1409:6815, 2014.

[81] D. K. Pratt, W. Tian, A. Kreyssig, J. L. Zarestky, S. Nandi, N. Ni, S. L. Budko, P. C. Canfield, A. I. Goldman, and R. J. McQueeney. *Phys. Rev. Lett.*, 103: 087001, 2009.

[82] C. Lester, J.-H. Chu, J. G. Analytis, S. C. Capelli, A. S. Erickson, C. L. Condron, M. F. Toney, I. R. Fisher, and S. M. Hayden. *Phys. Rev. B*, 79: 144523, 2009.

[83] X. F. Wang, T. Wu, G. Wu, R. H. Liu, H. Chen, Y. L. Xie, and X. H. Chen. *New J. Phys.*, 11:045003, 2009.

[84] Y. Laplace, J. Bobroff, F. Rullier-Albenque, D. Colson, and A. Forget. *Phys. Rev. B*, 80:140501, 2009.

[85] L. Pan, J. Li, Y.-Y. Tai, M. J. Graf, J.-X. Zhu, and C. S. Ting. *Phys. Rev. B*, 88:214510, 2013.

[86] L. Pan, J. Li, Y.-Y. Tai, M. J. Graf, J.-X. Zhu, and C. S. Ting. *Phys. Rev. B*, 90:134501, 2014.

[87] T. Das and A. V. Balatsky. *Phys. Rev. B*, 84:014521, 2011.

[88] S. Ideta, T. Yoshida, I. Nishi, A. Fujimori, Y. Kotani, K. Ono, Y. Nakashima, S. Yamaichi, T. Sasagawa, M. Nakajima, K. Kihou, Y. Tomioka, C. H. Lee, A. Iyo, H. Eisaki, T. Ito, S. Uchida, and R. Arita. *Phys. Rev. Lett.*, 110:107007, 2013.

[89] Q.-E. Wang, Z.-J. Yao, and F.-C. Zhang. *Europhys. Lett.*, 101:57002, 2013.

[90] Y. Yin, M. Zech, T. L. Williams, X. F. Wang, G. Wu, X. H. Chen, and J. E. Hoffman. *Phys. Rev. Lett.*, 102:097002, 2009.

[91] T. Hanaguri, S. Niitaka, K. Kuroki, and H. Takagi. *Science*, 328:474, 2010.

[92] L. Shan, Y.-L. Wang, B. Shen, B. Zeng, Y. Huang, A. Li, D. Wang, H. Yang, C. Ren, Q.-H. Wang, S. H. Pan, and H.-H. Wen. *Nat. Phys.*, 7:325, 2011.

[93] D. Wang, J. Xu, Y.-Y. Xiang, and Q.-H. Wang. *Phys. Rev. B*, 82:184519, 2010.

[94] Y. Gao, H.-X. Huang, C. Chen, C. S. Ting, and W.-P. Su. *Phys. Rev. Lett.*, 106:027004, 2011.

[95] I. I. Mazin, D. J. Singh, M. D. Johannes, and M. H. Du. *Phys. Rev. Lett.*, 101: 057003, 2008.

[96] T. Zhou, H. Huang, Y. Gao, J.-X. Zhu, and C. S. Ting. *Phys. Rev. B*, 83: 214502, 2011.

[97] W. F. Tsai, Y. Y. Zhang, C. Fang, and J. P. Hu. *Phys. Rev. B*, 80:064513, 2009.

[98] E. Plamadeala, T. Pereg-Barnea, and G. Refael. *Phys. Rev. B*, 81:134513, 2010.

[99] T. Zhou, Z. D. Wang, Y. Gao, and C. S. Ting. *Phys. Rev. B*, 84:174524, 2011.

[100] L. Pan, J. Li, Y.-Y. Tai, M. J. Graf, J.-X. Zhu, and C. S. Ting. *Phys. Rev. B*, 90:134501, 2014.

[101] S. Onari and H. Kontani. *Phys. Rev. Lett.*, 103:177001, 2009.

[102] G. R. Boyd, P. J. Hirschfeld, and T. P. Devereaux. *Phys. Rev. B*, 82:134506, 2010.

[103] D. V. Efremov, M. M. Korshunov, O. V. Dolgov, A. A. Golubov, and P. J. Hirschfeld. *Phys. Rev. B*, 84:180512(R), 2011.

[104] Y. Wang, A. Kreisel, and P. J. Hirschfeld. *Phys. Rev. B*, 87:094504, 2013.

[105] R. M. Fernandes, M. G. Vavilov, and A. V. Chubukov. *Phys. Rev. B*, 85: 140512(R), 2012.

[106] T. Berlijn, C.-H. Lin, W. Garber, and W. Ku. *Phys. Rev. Lett.*, 108:207003, 2012.

[107] J. Li, Y. Guo, S. Zhang, S. Yu, Y. Tsujimoto, H. Kontani, K. Yamaura, and E. Takayama-Muromachi. *Phys. Rev. B*, 84:020513(R), 2011.

[108] J. Li, Y. Guo, S. Zhang, Y. Tsujimoto, X. Wang, C.I. Sathish, S. Yu, K. Yamaura, and E. Takayama-Muromachi. *Solid State Commun.*, 152:671, 2012.

[109] J. Li, Y. F. Guo, S. B. Zhang, J. Yuan, Y. Tsujimoto, X. Wang, C. I. Sathish, Y. Sun, S. Yu, W. Yi, K. Yamaura, E. Takayama-Muromachiu, Y. Shirako, M. Akaogi, and H. Kontani. *Phys. Rev. B*, 85:214509, 2012.

[110] Z.-J. Yao, W.-Q. Chen, Y. Li, G. Cao, H.-M. Jiang, Q.-E. Wang, Z. Xu, and F.-C. Zhang. *Phys. Rev. B*, 86:184515, 2012.

[111] H. Wadati, I. Elfimov, and G. A. Sawatzky. *Phys. Rev. Lett.*, 105:157004, 2010.

[112] K. Nakamura, R. Arita, and H. Ikeda. *Phys. Rev. B*, 83:144512, 2011.

[113] A. D. Christinason, E. A. Goremychkin, R. Osborn, S. Rosenkranz, M. D. Lumsden, C. D. Malliakas, I. S. Todorov, H. Claus, D. Y. Chung, M. G. Kanatzidis, R. I. Bewley, and T. Guidi. *Nature*, 456:930, 2008.

[114] C.-T. Chen, C. C. Tsuei, M. B. Ketchen, Z. A. Ren, and Z. X. Zhao. *Nature Phys.*, 6:260, 2010.

[115] P. Ghaemi, F. Wang, and A. Vishwanath. *Phys. Rev. Lett.*, 102:157002, 2009.